

Modeling the Effects of Hearing Loss on Neural
Responses in the Cochlear Nucleus

MODELING THE EFFECTS OF HEARING LOSS ON NEURAL
RESPONSES IN THE COCHLEAR NUCLEUS

BY
STEPHEN VETSI, B.Eng.Mgt.

A THESIS
SUBMITTED TO THE DEPARTMENT OF ELECTRICAL & COMPUTER ENGINEERING
AND THE SCHOOL OF GRADUATE STUDIES
OF MCMASTER UNIVERSITY
IN PARTIAL FULFILMENT OF THE REQUIREMENTS
FOR THE DEGREE OF
MASTER OF APPLIED SCIENCE

© Copyright by Stephen Vetsis, June 2009
All Rights Reserved

Master of Applied Science (2009)
(Electrical & Computer Engineering)

McMaster University
Hamilton, Ontario, Canada

TITLE: Modeling the Effects of Hearing Loss on Neural Responses in the Cochlear Nucleus

AUTHOR: Stephen Vetsis
B.Eng.Mgt., (Electrical Engineering and Management)
McMaster University, Hamilton, ON, Canada

SUPERVISOR: Dr. Ian C. Bruce

NUMBER OF PAGES: xi, 158

This thesis is dedicated Mr. Gary Gran.

Abstract

Physiological studies of neurons in the dorsal cochlear nucleus (DCN) and ventral cochlear nucleus (VCN) performed by Ma and Young (2006) and Cai *et al.* (2008), respectively, showed the changes in response properties that arise following acoustic trauma. A model of the auditory periphery by Zilany and Bruce (2007), capable of modeling the effects of acoustic trauma on auditory nerve (AN) fiber responses, was used to simulate inputs to computational models of DCN and VCN cells in order to determine if the changes shown by Cai *et al.* (2008) and Ma and Young (2006) could be fully explained by changes in the auditory periphery.

DCN cells simulated using the Zheng and Voigt (2006) DCN model receiving AN inputs from an impaired auditory periphery were able to reproduce many of the types of responses shown by Ma and Young (2006). Providing impaired AN inputs with compound action potential (CAP) threshold shifts beginning just above DCN cell best frequency (BF) were able to reproduce the tail responses reported by Ma and Young (2006). Type III DCN cells showed class A tail responses whereas, type IV and IV-T DCN cells showed class B tail responses as a result of impaired inputs from the auditory periphery. Type IV-T cells also showed class B-like tails in responses to CAP threshold shifts beginning well below BF. A similar study was performed with VCN cells modeled using the Rothman and Manis (2006c) model. Modeled VCN cells receiving impaired inputs from the auditory periphery did not show most of the behaviors reported by Cai *et al.* (2008) indicating that the changes in VCN cell responses following acoustic trauma are the result of either plastic changes in the brainstem or of features of normal VCN cell responses that are not currently captured by the model.

Acknowledgements

First and foremost, I would to thank my supervisor, Dr. Ian Bruce, for all of his help and guidance in completing this thesis. Over the course of my graduate studies he was nothing short of the perfect supervisor. It's quite possible that without his knowledge, patience and ability to talk me out of panicking, I may have gone insane a long time ago.

Many thanks to my collaborators, Dr. Herbert F. Voigt and Xiaohan Zheng, for their input and help. Extra thanks to Xiaohan for her tremendous help with all things relating to the DCN model code.

I would also like to give a special thanks to all of my good friends: Teddy , Sortwell, Tanya and Wayne Dainard ... I mean Meinen, Julie, Jurek, Charlie and Waleed. Without all of you I may have actually finished this thesis on time. I mean that in a good way. Special mention goes to Mr. Michael Quincy Dainard for always taking the late shift even if it meant getting the Jack, to Mr. George Gkoloumpovits for spending far too much time with me and to my adopted parents, Deb and Ricky D. If not for all your care packages #1 adopted Greek son may have starved before this thesis was complete.

Finally, I would like to thank my family for their love and support. When other people were telling me I was crazy for staying in school this long all of you pushed me to stick with it. Mom, Dad, it turns out you were right... again.

This research was funded by the Canadian Institute of Health Research (New Emerging Teams Grant 54023).

Abbreviations

Abbreviation	Term
AN	Auditory nerve
AP	Action potential
BF	Best frequency
BM	Basilar membrane
CAP	Compound action potential
CF	Characteristic frequency
CV	Coefficient of variation
DCN	Dorsal cochlear nucleus
ISI	Inter-spike interval
P-cell	DCN primary cell
PSTH	Post-stimulus time histogram
RM	Response map
SR	Spontaneous firing rate
VCN	Ventral cochlear nucleus

Contents

Abstract	iv
Acknowledgements	v
Abbreviations	vi
1 Introduction	1
1.1 Scope of Work	2
1.2 Contributions of this Work	2
1.3 Thesis Layout	3
1.4 Related Publications	3
2 Background & Theory	5
2.1 Neurons	5
2.1.1 Physiology	5
2.1.2 Models	11
2.1.2.1 The Leaky Integrate and Fire Model	11
2.1.2.2 Hodgkin-Huxley Model	13
2.2 The Auditory System	17
2.2.1 The Auditory Periphery	17
2.2.1.1 The Outer and Middle Ears	18
2.2.1.2 The Cochlea	21
2.2.2 Auditory Nerve Fibers	31
2.2.3 The Central Auditory System	41
2.2.4 The Cochlear Nucleus	44
2.2.4.1 The Ventral Cochlear Nucleus (VCN)	45
2.2.4.2 The Dorsal Cochlear Nucleus (DCN)	50
3 The Effects of Hearing Loss on Modeled Neurons in the DCN	56
3.1 Models of the Auditory Periphery	56
3.1.1 The Carney Model	57

3.1.2	The Zilany-Bruce Model	59
3.2	Zheng and Voigt DCN Model	61
3.2.1	Model Implementation	65
3.3	Healthy Modeled Neurons in the DCN	68
3.3.1	Comparison of the response maps of simulated DCN units using the two different AN fiber models	68
3.3.2	Comparison of the response properties of the AN fiber inputs produced by each AN model	68
3.3.3	Effects of DCN connection parameter changes on DCN cell re- sponse properties	71
3.3.4	Ideal DCN Connection Parameters	73
3.4	Impaired Modeled Neurons in the DCN	76
4	The Effects of Hearing Loss on Modeled Neurons in the VCN	90
4.1	Rothman and Manis Model	90
4.1.1	Model Implementation	94
4.1.2	Using Zilany-Bruce Model AN inputs	98
4.2	Healthy Modeled Neurons in the VCN	101
4.3	Impaired Modeled Neurons in the VCN	115
5	Conclusions & Future Works	135
5.1	Conclusions	135
5.2	Suggestions for Future Works	137
A	MATLAB code and ideal DCN model parametrs	138
A.1	VCN Model Code	138
A.1.1	VCN_v9.m	138
A.1.2	VCN_RK4solv_main_v2.m	143
A.1.3	VCN_RK4solv_v2.m	144
A.1.4	RK4_deriv_calc.m	144
A.1.5	VCN_RK4solv_main_v2.m	145
A.1.6	gateparts.m	145
A.1.7	gatetaus_v2.m	146
A.1.8	voltderiv_v2.m	146
A.1.9	gatederiv.m	147
A.2	CV Calculation Code	148
A.2.1	CVplot.m	148
A.3	Code for generating AN inputs to the Zheng and Voigt (2006) DCN model	149
A.3.1	fANimpairgenv2.m	149
A.4	DCN model ideal parameters	152

List of Figures

2.1	Anatomical features of a neuron	6
2.2	Illustration of voltage-gated ion channels	8
2.3	Sodium-Potassium pump.	8
2.4	Action potential phases	9
2.5	Signal transmission at a chemical synapse	11
2.6	Circuit diagram of the linear, passive leaky integrate and fire model. .	12
2.7	Spiking neuron simulated using the integrate and fire model in response to an injected current	14
2.8	Physiology of the auditory periphery	17
2.9	Average pressure gain as a function of frequency and direction	19
2.10	The middle ear	20
2.11	The transfer function of the middle ear in cats and humans	21
2.12	Physiology of the cochlea	22
2.13	Cross-section of the Cochlear Duct	23
2.14	Illustration of the organ of Corti	25
2.15	Cochlear hair cells	26
2.16	Cochlear hair cell physiology	27
2.17	Innervation of hair cells in the cochlea.	28
2.18	Basilar membrane traveling waves.	29
2.19	Basilar membrane response to various stimulus intensities.	30
2.20	Basilar membrane tuning curve	31
2.21	Inner Hair cell voltage responses	32
2.22	PSTH of an AN fiber	33
2.23	AN fiber tuning curves	35
2.24	AN fiber Q_{10} values	36
2.25	AN fiber rate-intensity relationship	37
2.26	AN fiber iso-intensity curves and frequency glide effects	38
2.27	Phase-locking of AN fibers	39
2.28	PSTH showing two-tone suppression in AN fibers	40
2.29	The ascending pathways of the brainstem	42
2.30	Regions of the Cochlear Nucleus and AN projections	46

2.31	Morphology of the endbulb of Held	47
2.32	Octopus cell morphology.	48
2.33	VCN cell response types.	49
2.34	DCN structure	50
2.35	Pyramidal cell response types	51
2.36	DCN internal circuit	53
2.37	DCN standard response maps	54
2.38	DCN principal cell model	55
3.1	Carney model schematic	58
3.2	Zilany-Bruce model schematic	59
3.3	DCN model schematic	62
3.4	DCN model connection parameters	63
3.5	DCN neuron circuit model	64
3.6	Simulated DCN cell responses to both Carney and Zilany & Bruce modeled AN fibers	69
3.7	AN fiber response maps	70
3.8	Simulated type-II responses using different AN model inputs	72
3.9	Simulated W-cell responses using different AN model inputs	72
3.10	Effects of DCN model parameters on simulated type-II cell responses	74
3.11	Simulated physiological DCN principal cell responses using Zilany & Bruce model AN inputs	77
3.12	Simulated type IV-T DCN principal cell iso-intensity curves	78
3.13	Impaired DCN cell “tail” distributions	79
3.14	Simulated type III cell receiving impaired AN inputs with a CAP threshold function rising edge at 10 kHz	80
3.15	Simulated type IV cell receiving impaired AN inputs with a CAP threshold function rising edge at 10 kHz	81
3.16	Simulated type IV-T cell receiving impaired AN inputs with a CAP threshold function rising edge at 10 kHz	82
3.17	Simulated type III cell receiving impaired AN inputs with a CAP threshold function rising edge at 6 kHz	83
3.18	Simulated type IV cell receiving impaired AN inputs with a CAP threshold function rising edge at 10 kHz	84
3.19	Simulated type IV-T cell receiving impaired AN inputs with a CAP threshold function rising edge at 6 kHz	85
3.20	Simulated type III cell receiving impaired AN inputs with a CAP threshold function rising edge at 1 kHz	86
3.21	Simulated type IV cell receiving impaired AN inputs with a CAP threshold function rising edge at 1 kHz	87

3.22	Simulated type IV-T cell receiving impaired AN inputs with a CAP threshold function rising edge at 1 kHz	88
4.1	Raster plots of AN data	97
4.2	AN fiber spontaneous rate histograms	99
4.3	Simulated spherical bushy cell PSTHs and regularity analysis	103
4.4	Simulated globular bushy cell PSTHs and regularity analysis	104
4.5	Effect of CF spread of AN inputs on simulated globular bushy cells	105
4.6	Simulated octopus cell PSTHs and regularity analysis	107
4.7	Simulated D-stellate cell PSTHs and regularity analysis	108
4.8	Effect of a spread of AN inputs with a spread of CFs on a simulated D-stellate cell	110
4.9	Effect of a different cell model on the sustained firing of a simulated D-stellate cell	111
4.10	Simulated T-stellate cell PSTHs and regularity analysis	112
4.11	Effect of AN inputs with a physiological spread of CFs on a simulated T-stellate cell	119
4.12	Effect of a different (type I-t) cell model on a simulated T-stellate cell	120
4.13	Primary-like neuron iso-intensity curves	121
4.14	Simulated D-stellate cell iso-intensity curves	122
4.15	Simulated octopus cell iso-intensity curves	123
4.16	Simulated T-stellate cell iso-intensity curves	124
4.17	Rate-level curves of recorded impaired and unimpaired primary-like VCN cells	125
4.18	Rate-level curves of recorded impaired and unimpaired chopper VCN cells	126
4.19	Spread of excitation in recorded VCN cells following hearing impairment	127
4.20	Rate-level curves of simulated impaired and unimpaired primary-like VCN neurons	128
4.21	Rate-level curves of simulated impaired and unimpaired onset chopper cells	129
4.22	Rate-level curves of simulated impaired and unimpaired sustained chopper cells	130
4.23	Rate-level responses of simulated octopus cells to both impaired and unimpaired AN inputs	131
4.24	Change in spread of excitation of an onset chopper cell following acoustic trauma	132
4.25	Change in spread of excitation of a simulated sustained chopper cell following acoustic trauma	133
4.26	Change in spread of excitation of a simulated onset cell following acoustic trauma	134

Chapter 1

Introduction

Physiological and modeling studies into the function of the mammalian auditory periphery have resulted in robust computational models capable of not only reproducing responses to a wide variety of stimuli but also of reproducing the effects of hearing loss on the responses of auditory nerve (AN) fibers. While knowledge of the effects of hearing loss on the function of the auditory periphery is fairly detailed, only recently have physiological studies of the effects of hearing loss on processing of auditory signals in the brainstem begun to emerge (Cai *et al.*, 2008; Ma and Young, 2006). Physiological studies into the anatomy and function of cells in the central auditory system have provided enough insight into the way sound is processed by the mammalian brain to yield computational models for the function of cells in the mammalian cochlear nucleus (CN). These models, however, have been developed with older, more simplistic models of the auditory periphery and the effects of hearing loss have not been seriously explored.

Anatomical studies of changes in the central auditory system following acoustic trauma have shown significant changes in structure and function following acoustic trauma typically demonstrated by a reorganization of the projection maps in the auditory cortex (Syka, 2002). While there is some general knowledge of physiological changes in the central auditory system following acoustic trauma, it is not currently known whether the responses of CN cells shown by Ma and Young (2006) and Cai *et al.* (2008) are the result of changes in the auditory periphery or due to synaptic reorganization that takes place in the auditory system following acoustic trauma. Computational models of AN fibers capable of reproducing the effects of hearing loss on the auditory periphery were used as inputs into current computational models of CN cells in an attempt to explore the effects of hearing loss on the function of modeled neurons in the CN.

1.1 Scope of Work

These works were undertaken to perform a preliminary modeling study of the effects of hearing loss on the response properties of neurons in the CN. Existing models of neurons in the ventral cochlear nucleus (VCN) by Rothman and Manis (2006c) and dorsal cochlear nucleus (DCN) by Zheng and Voigt (2006) were used in conjunction with the Zilany and Bruce (2007) model of the auditory periphery. The Zilany and Bruce (2007) model was chosen as it is one of the only current models of the auditory periphery capable of reproducing the effects of hearing loss. It has also been verified for an extensive set of acoustic stimuli.

The goal of these works was to combine the DCN and VCN computational models with the Zilany and Bruce (2007) model. Once the various models were integrated, impaired AN inputs were used to examine their effects on simulated CN cells. Attempts were made to match AN inputs to reported physiological configurations, where physiological information was available. Modeled impaired neurons were simulated with AN inputs matching the threshold shifts reported in hearing impairment studies by Cai *et al.* (2008) and Ma and Young (2006).

Due to significant differences between the AN models originally used as inputs for the development of the DCN and VCN models, it was expected that some complications would arise. The DCN and VCN model response properties using Zilany and Bruce (2007) AN inputs were analyzed with healthy AN inputs. Published modeled and physiological results were compared to simulated results using the new inputs and an attempt was made to explain the changes from both a modeling and physiological perspective. These comparisons were made to help guide future works to provide more robust and physiologically sound models of CN neurons. Attempts were made to find a parameter set for the DCN model to behave as similarly as possible to recorded DCN cells. In the case of modeled VCN cells, no attempt at studying the effects of parameter changes was made due to time constraints.

1.2 Contributions of this Work

Recent physiological studies by Ma and Young (2006) and Cai *et al.* (2008) showed the changes in response properties of neurons in the DCN and VCN, respectively, as a result of peripheral hearing loss. The source of the changes in response properties, in each case, was unknown. We performed computational studies of the responses of DCN and VCN cells receiving inputs simulating hearing loss in the auditory periphery to determine if the changes observed by Ma and Young (2006) and Cai *et al.* (2008) were the result of changes in the auditory periphery or plastic changes in the brainstem. DCN cells simulated with hearing loss in the auditory periphery were able to reproduce many of the responses shown by Ma and Young (2006). Modeled VCN

neuron responses to hearing loss in the auditory periphery did not show the changes in responses reported by Cai *et al.* (2008) indicating that plastic changes in the VCN are the source of the changes in VCN cell responses following acoustic trauma.

While the Rothman and Manis (2006c) model was shown to reproduce the responses of most VCN cell types to a wide variety of stimuli when provided with unimpaired AN inputs, as modeled by Zilany and Bruce (2007), it proved unable to accurately model the responses of T-stellate cells. Computer simulations were able to show that currently unmodeled inhibitory synaptic inputs from D-stellate cells, shown in physiological studies by Ferragamo *et al.* (1998), are required in order to properly model the physiological responses of T-stellate cells.

1.3 Thesis Layout

Following this introduction, Chapter 2 provides an overview of the physiology of neurons, the function of the auditory system, and descriptions of the leaky-integrate-and-fire and Hodgkin and Huxley models of the neuron. Knowledge of these topics is necessary for understanding of the works that follow. Chapter 3 contains descriptions of the Carney (1993) and Zilany and Bruce (2007) models of the auditory periphery, as well as the Zheng and Voigt (2006) model of the DCN. Details are provided about the implementation of each of these computational models. Simulated DCN cells using both models of the unimpaired the auditory periphery are compared and discrepancies discussed. A description of a qualitative framework of determining ideal DCN model parameters using Zilany and Bruce (2007) AN inputs is given. Modeled DCN cells receiving both impaired and unimpaired inputs from the auditory periphery are then shown. Simulated impaired DCN cell responses are compared to physiological studies and discussed. Chapter 4 contains descriptions of the Rothman and Manis (2006c) model of VCN cells as well as details of the computational implementation of the model. Modeled VCN cells receiving both impaired and unimpaired inputs from the auditory periphery are then shown and results compared to both modeling and physiological studies. Chapter 5 contains a discussion of the limitations of each of the current models of the CN as well as discussion of the main findings of these works. That discussion is then followed by descriptions of possible future works to be undertaken using these findings.

1.4 Related Publications

Parts of this thesis have appeared in the following publications:

Vetsis, S., Zheng, X., Voigt, H. F., and Bruce, I. C. (2008). Effects of an improved auditory-periphery model on the response properties of modeled neurons in the dorsal cochlear nucleus. In *Proceedings of 30th Annual International Conference of the IEEE Engineering in Medicine and Biology Society (EMBC2008)*, pages 2477–2480. IEEE, Piscataway, NJ.

Zheng, X., Giang, A., Vetsis, S., Bruce, I. C., and Voigt, H. F. (2008). A computational modeling study of the effects of acoustic trauma on the dorsal cochlear nucleus. In *Proceedings of 4th European Conference of the International Federation for Medical and Biological Engineering (ECIFMBE 2008)*, volume 22, pages 2695–2698. Antwerp, Belgium.

Chapter 2

Background & Theory

2.1 Neurons

Neurons are the fundamental building blocks of the nervous system. They are able to produce rapidly changing electrochemical impulses, called action potentials, that can be transmitted throughout the body to control a variety of bodily functions, such as causing muscles to contract. Networks of interconnected neurons in the brain are able to perform a variety of complex processing functions, such as speech processing and recognition. The following section provides a brief overview of the physiological mechanisms governing the function of neurons.

2.1.1 Physiology

The anatomical features of a typical neuron can be seen in Figure 2.1. There are four main parts to each neuron: (i) the cell body or soma, (ii) the axon, (iii) the dendrites and (iv) synapses. The soma can be described as the information processing part of a neuron. It takes inputs from the dendrites. These inputs then trigger an electrochemical response in the soma which is then transmitted as a propagating electrochemical impulse from the soma along the axon to another cell (neuron, muscle tissue, etc.). Synapses are the connection mechanism between dendrite and axon terminals and the neurons they connect to. To fully understand this process, we must first understand the underlying physiological processes that allow neurons to produce these electrochemical responses.

The soma is bounded by a semi-permeable barrier known as the cell membrane. The cell membrane separates the contents of a cell from the extracellular space. It consists mainly of a lipid bilayer made of phospholipids with hydrophilic heads and hydrophobic tails. These phospholipids orient themselves with the polar hydrophilic heads facing outwards into extra-cellular space and the soma cytoplasm and with

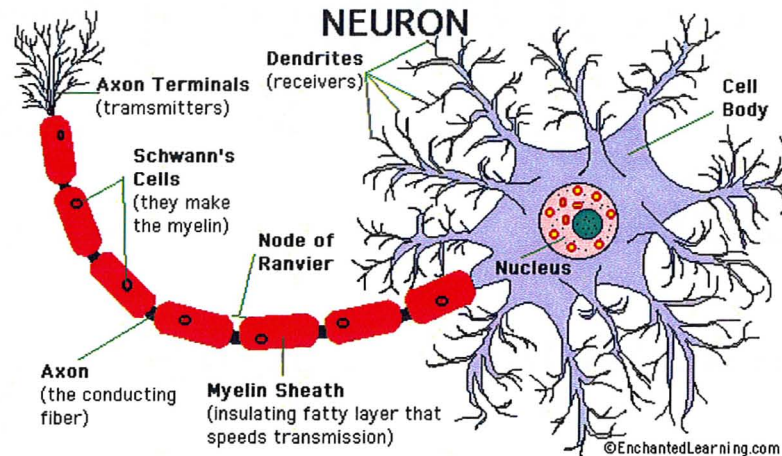


Figure 2.1: Illustration of the anatomical features of a neuron. (Reprinted from EnchantedLearning.com (2009))

the non polar hydrophilic tails in between. The tight packing of phospholipids in the bilayer limits the flow of various ions across the cell membrane. The difference in concentrations of ions on either side of the cell membrane produces an electrochemical gradient (Tortora and Grabowski, 2003).

In order for changes to occur in the transmembrane potential, there must be some way for ions to cross the cell membrane and cause changes in ion concentrations. This is accomplished in three ways: (i) facilitated diffusion, (ii) voltage-gated ion transport and (ii) active transport. All methods use ion channels or pumps in the membrane that provide pathways for ions to cross the membrane.

In the case of facilitated diffusion a type of ion channel called a leakage channel is used. Leakage channels are passive openings that fluctuate randomly between open and closed positions and allow potassium and sodium ions to cross the membrane in the direction determined by the electrochemical gradient. Ions will travel from a region of high concentration to a region of low concentration as well as in the direction determined by the transmembrane potential (Tortora and Grabowski, 2003). The movement of these ions is described by the Nernst equilibrium potential (Plonsey and Barr, 2000). The Nernst equilibrium potential:

$$V_m^{eq} = -\frac{RT}{Z_p F} \ln \frac{[C_p]_i}{[C_p]_e} \quad (2.1)$$

defines that potential across the membrane that exactly opposes the net diffusion of an ion across the membrane. R represents the gas constant, T represents the absolute temperature, F is Faraday's constant, Z_p is the valence of the ion p and $[C_p]_i$ and $[C_p]_e$ represent the intracellular and extracellular concentrations of ion p , respectively.

Voltage-gated ion channels are primarily responsible for the ability of neurons to generate action potentials. These ion channels open in response to changes in the transmembrane potential. The two ions that are mainly responsible for the generation of action potentials are sodium and potassium. Each has their own voltage-gated ion channels. Diagrams of both types of voltage-gated channels can be seen in Figure 2.2. The voltage-gated sodium channel has two types of gating particles, activation particles and inactivation particles. At resting potential the activation gating particles are mostly closed and the inactivation gating particles are mostly open. As the transmembrane potential is increased towards a certain value (typically between, -70 and -50mV) a conformational change occurs in the activation gating particles causing them to open. The voltage-gated channel at this stage is considered to be in an “activated” state and allows Na^+ ions to pass into the membrane. The permeability of the membrane to sodium in the activated state is increased as much as 500 to 1000 fold (Guyton and Hall, 2000). The voltage change that caused the opening of the activation gating particles also initiates the closing of the inactivation particles. However, the inactivation particles close more slowly than the activation particles open. Once the inactivation particle closes a voltage-gated sodium channel is said to be in an “inactivated” state. Na^+ ions can no longer freely cross the membrane and the channel is closed. The inactivation particles will also not reopen until the cell has returned to near its resting potential. Once at the resting potential, the voltage-gated channels return back to their resting state.

The main type of voltage-gated potassium channel differs from its sodium counterpart in that it has only one type of gating particle and two states. At its resting state the gating particles are mostly closed, preventing the flow of K^+ ions out of cell. As the transmembrane potential is increased, a conformational change in the voltage-gated potassium channel occurs, similar to the voltage-gated sodium channel. The main difference is that the voltage-gated potassium channel opens very slowly. By the time the voltage-gated potassium channel opens, the voltage-gated sodium channels are beginning to close due to inactivation. The decreased entry of Na^+ ions into the cell combined with the increased permeability of the membrane to K^+ ions causes the cell to return to its resting potential.

Active transport is performed by pumps such as the sodium-potassium pump. The sodium-potassium pump maintains the steep Na^+ and K^+ concentration gradients across the cell membrane. It moves ions against the concentration gradient and, as such, requires energy in the form of ATP for its function. A graphical representation of this process can be seen in Figure 2.3 below. The sodium-potassium pump moves three Na^+ ions outside the cell for every two K^+ ions it allows into the cell. It allows for the cell membrane to recover back to its resting level of ion concentrations across the membrane after the generation of action potentials.

Action potentials are spike-like electrical potentials that are produced by excitable

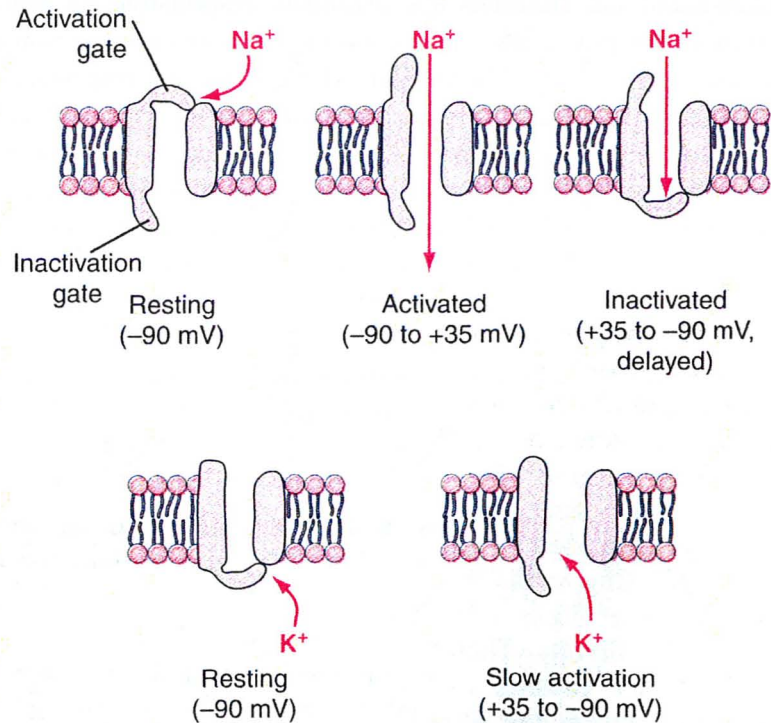


Figure 2.2: Illustration of voltage-gated ion channels. The voltage-gated sodium channel is shown on top. The orientation of the gating particles in the resting, activated and inactivated state are shown. The voltage-gated potassium is shown below as well as its two states; resting and slow activation. In both illustrations intracellular space is located on the downwards side of the membrane shown. (Figure 5-7 reprinted from Guyton and Hall (2000))

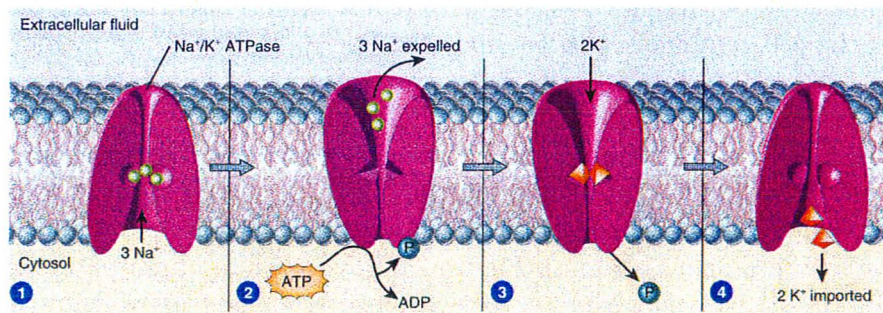


Figure 2.3: Illustration of Sodium-Potassium pump process. Figure 3.11 reprinted from Tortora and Grabowski (2003).

cells. They are “all-or-none” events that occur when a membrane is depolarized beyond a certain point called the threshold potential. Each action potential generated by an excitable cell is practically identical in shape and temporal characteristics. Due to the “all-or-none” nature of these events, the information they contain is typically not in the shape of the action potential itself but rather in the time at which it occurs and the rate of spiking. Action potential waveforms are divided into four different phases: (i) resting/stimulus phase, (ii) depolarizing phase, (iii) re-polarizing phase and (iv) hyperpolarizing phase. These four stages can be seen in the diagram of an action potential shown in Figure 2.4 below.

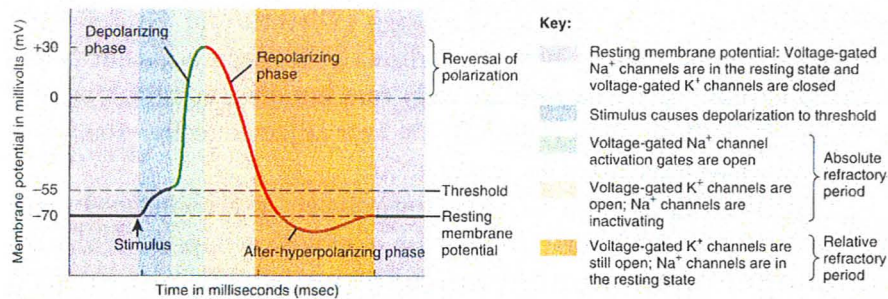


Figure 2.4: Illustration of the various phases of action potential generation. Key physiological events responsible for each stage are listed to the right of the illustration. Figure 12.11 reprinted from Tortora and Grabowski (2003).

During the resting/stimulus phase the membrane is initially in its resting state. A stimulus is applied to depolarize the membrane. If the stimulus is not strong enough, the membrane will not reach the action potential threshold and will eventually return to its resting potential once the stimulus is removed. Facilitated diffusion and active transport dominate the membrane response at this stage. If the applied stimulus drives the membrane beyond the action potential threshold the voltage-gated sodium channels activate and the membrane then enters the depolarizing phase. The newly opened voltage-gated sodium-channels allow a large influx of Na^+ ions into the cell and cause a sharp and quick depolarization of the cell membrane. As this sharp depolarization begins to subside the membrane enters the re-polarizing phase. At this point the voltage-gated sodium channels have begun entering their inactivated state and the voltage-gated potassium channels have opened. This virtually ends the influx of Na^+ ions and we begin to see an efflux of K^+ ions causing re-polarization of the cell membrane. As the membrane potential approaches the resting potential the membrane may enter a hyperpolarizing phase. At this stage the voltage-gated potassium channels are slowly beginning to close however they are still allowing some K^+ ions to leave the cell which causes the membrane to hyperpolarize beyond the

resting potential until the channels fully close. Once fully closed, active transport and facilitated diffusion of Na^+ and K^+ ions occurs until the membrane reaches its resting state again.

From the previous discussion on the generation of action potentials, it is clear that some form of stimulus is normally required at the soma to cause the neuron to fire an action potential. In the body, these stimuli are transferred to the soma by synapses. Synaptic inputs arrive at both the dendrites and the soma causing post-synaptic potentials which can generate action potentials. There are two types of synapses: (i) chemical synapses and (ii) electrical synapses. Electrical synapses are typically present in axonal connections to visceral smooth muscles and cardiac muscles among other cells in the body (Tortora and Grabowski, 2003). Electrical synapses conduct action potentials directly between adjacent cells via gap junctions. Gap junctions contain approximately one hundred tubular connexons which act like tunnels connecting the cytosol of the two adjacent cells. Ions flow directly through the connexons from one cell to the next.

The works in this thesis focus entirely on interconnected neurons. Neurons are typically connected to one another by chemical synapses. Unlike electrical synapses, the intracellular spaces of the presynaptic neuron (the one sending the signal) and the postsynaptic neuron (the one receiving the signal) are not connected. Instead there is a space between the two neurons, called the synaptic cleft. When an action potential from the presynaptic neuron reaches the chemical synapse, it triggers the release of neurotransmitters that diffuse across the synaptic cleft. The neurotransmitters bind to neurotransmitter receptors in the postsynaptic neuron's cell membrane. This event triggers the opening of a type of ion channel called a ligand-gated ion channel. The newly opened ligand-gated ion channel in turn allows ions to enter the postsynaptic neuron and trigger a change in the postsynaptic neuron's transmembrane potential called a postsynaptic potential. Ligand-gated ion channels are similar to voltage-gated ion channels. The difference is that they open in response to the presence of neurotransmitters in the neurotransmitter receptors as opposed to changes in the transmembrane potential. This process is illustrated in Figure 2.5.

There are two main types of postsynaptic potentials: (i) excitatory postsynaptic potentials (EPSPs) and (ii) inhibitory postsynaptic potentials (IPSPs). The type of postsynaptic potential is determined, primarily, by the Nernst equilibrium potential of ion that travels through the ligand-gated ion channel. When a neurotransmitter is received by a ligand-gated ion channel, the ion channel opens and allows ions to flow as forced by the electrochemical gradient. If the electrochemical gradient forces a net influx of positive ions and increases the neuron's transmembrane potential, an EPSP is generated. EPSPs make the cell more excitable since the transmembrane potential is now closer to the action potential threshold and will be able to fire an action potential in response to a smaller stimulus. Conversely, an IPSP is generated when

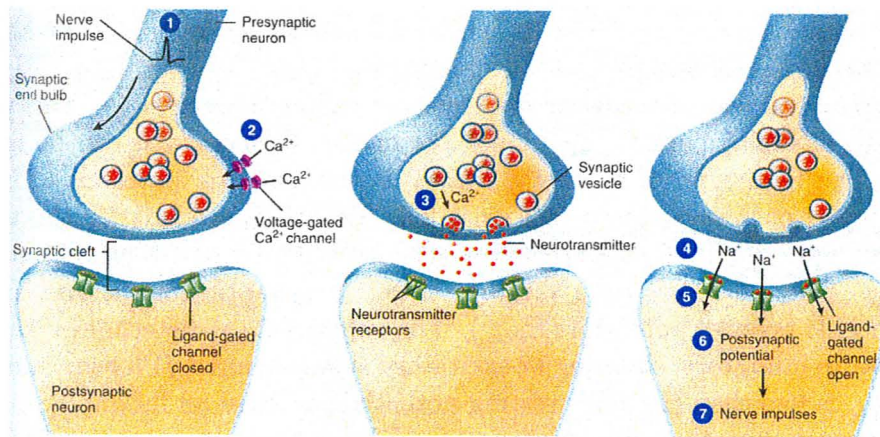


Figure 2.5: Illustration of signal transmission at a chemical synapse. Figure 12.14 reprinted from Tortora and Grabowski (2003).

the net ionic movement across the membrane as a result of the opening of ligand-gated ion channels causes a hyperpolarization of the postsynaptic neuron. The net result of the influx of ions results in a decrease in the postsynaptic neuron's transmembrane potential and a decrease in overall excitability.

2.1.2 Models

There are several computational models able to describe the behavior of the neural transmembrane potential using simple circuit elements. These models are all comprised of capacitors, voltage sources and variable resistors. The two main models used in these works are: (i) the leaky integrate and fire model and (ii) the Hodgkin-Huxley model.

2.1.2.1 The Leaky Integrate and Fire Model

The leaky integrate and fire model is a very simple model of a neuron. The simplicity of the leaky integrate and fire model lies in the fact that it does not attempt to explicitly reproduce the specific shape of the action potential waveform. Instead, the model is divided into two parts: (i) a linear/passive circuit model and (ii) an *ad hoc* non-linear model for representing action potential generation. The passive linear circuit model can be seen in Figure 2.6. There are four main current pathways to the passive cell model (Koch, 1999). The first is the membrane capacitance (C_m) which allows for the gradual changes in the transmembrane potential in response to sustained stimuli as well as the gradual re-polarization of the membrane to rest. The second is the leakage pathway consisting of the membrane resistance (R_m) and the

membrane resting potential (V_{rest}). In the absence of other stimuli, this pathway will drive the model back to the cell's resting potential. The third pathway is the injected current pathway, denoted by the transient current source (I_{inj}). This pathway is used when modeling current injection experiments. Otherwise, it can be ignored.

The final type of current pathway is the synaptic pathway. There are several synaptic pathways shown in Figure 2.6. This is to account for the variable number of synaptic inputs for different neurons. All synaptic pathways are modeled the same way. They all consist of a variable, transient synaptic conductance ($G_{syn_n}(t)$) and a synaptic reversal potential (E_{syn_n}). The value of E_{syn_n} determines whether or not we have an inhibitory, shunting or excitatory synaptic input (Plonsey and Barr, 2000). If E_{syn_n} is less than the cell's resting potential, we have an inhibitory synapse. If E_{syn_n} is greater than the cell's resting potential, we have an excitatory synapse. If E_{syn_n} lies around the resting potential, shunting inhibition occurs.

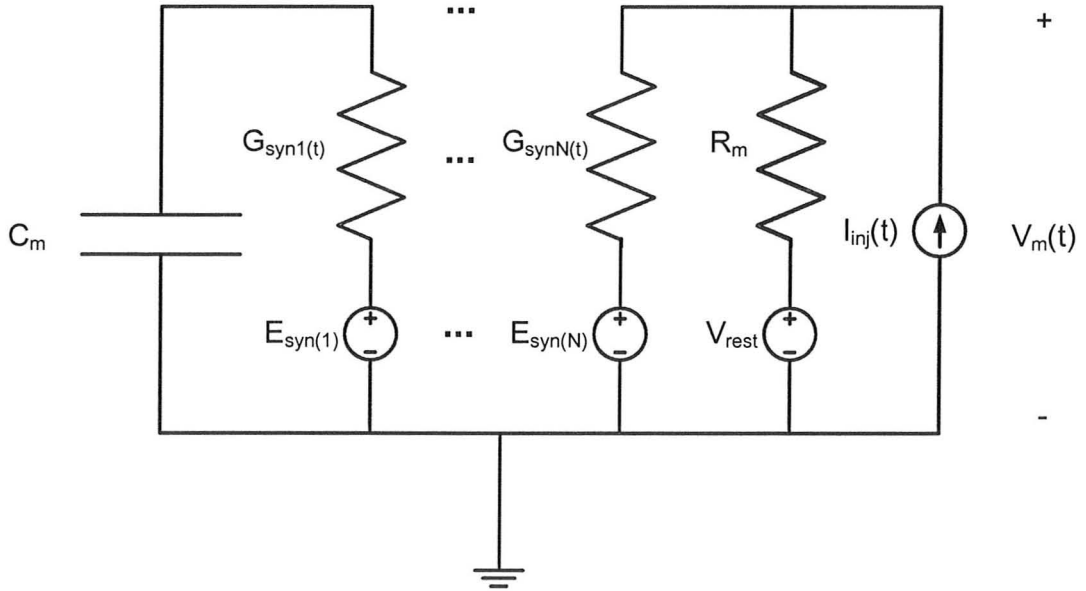


Figure 2.6: Circuit diagram of the linear, passive leaky integrate and fire model.

The transmembrane potential is computed using

$$C \frac{dV_m(t)}{dt} = I_{inj}(t) - \frac{V_m(t) - V_{rest}}{R_m} - G_{syn_1}(t)(V_m(t) - E_{syn_1}) - \dots - G_{syn_N}(t)(V_m(t) - E_{syn_N}) \quad (2.2)$$

This differential equation is obtained by performing a summation of all the currents in the passive model.

When the transmembrane potential crosses the threshold potential, an action potential is said to be generated and we switch to our non-linear model. The *ad hoc* non-linear model represents action potentials as delta functions. The transmembrane potential is set to a large value at the instant the action potential occurs and set to the resting potential for the duration of the absolute refractory period to model refractory effects (Koch, 1999). For an illustration of this process see Figure 2.7 below.

The leaky integrate and fire model is useful tool for neural modeling in situations where we are concerned with the timing of action potential activity for lengthy stimuli. In these cases the specific shape of the action potential waveform is not of paramount importance. As such, the leaky integrate and fire model can be used as a reasonable approximation of neural activity while limiting the computational load required in simulations.

2.1.2.2 Hodgkin-Huxley Model

In the late 1940s Hodgkin and Huxley performed a series of voltage and space clamp experiments on squid axons in an attempt to create a model for representing the kinetics behind membrane currents. The experiments were performed under several assumptions (Koch, 1999). Firstly, it was assumed that action potentials typically involve only two types of currents; ionic currents and capacitive currents. Second, that the ionic currents in open ion channels are linearly related to transmembrane potential via Ohm's law. Finally, that each ionic current could be represented as a maximum conductance multiplied by numerical coefficients representative of the fraction of open channels. Those constants are functions of gating particles which have one of two states; open or closed. This results in expressions of ionic currents:

$$I_K(t) = g_K(t, v_m)(V_m - E_K) \quad (2.3)$$

$$I_{Na}(t) = g_{Na}(t, v_m)(V_m - E_{Na}) \quad (2.4)$$

A "voltage clamp" condition is obtained via an experimental setup that forces the membrane potential to a certain desired voltage. By fixing the transmembrane potential, Hodgkin and Huxley were able to separate the capacitive currents from the ionic currents. Space clamping was used to eliminate axial spatial dependence. It has the effect of keeping the potential along the entire axon uniform so that the resulting currents are radial. Space clamping is achieved by inserting a highly conductive axial conductor along the axon.

These experiments resulted in a set of differential equations for the sodium and potassium ion current dynamics. Of the two, the potassium model is simplest. The

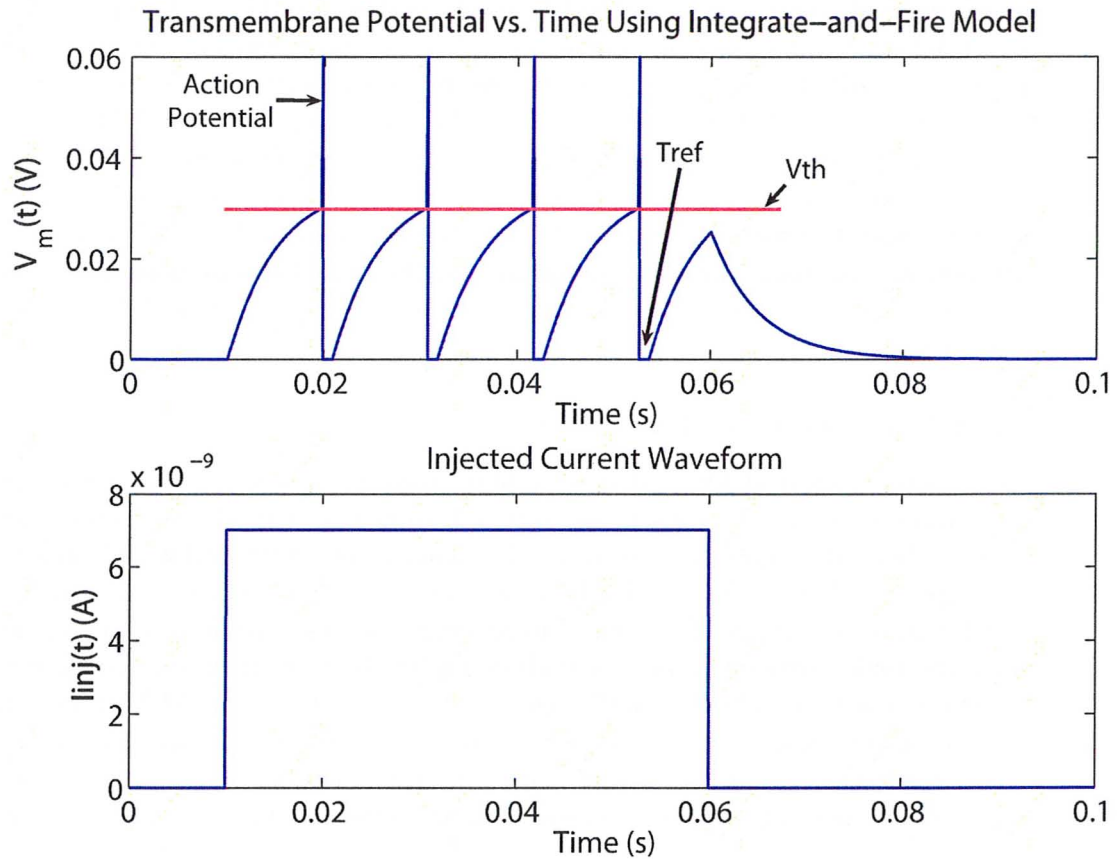


Figure 2.7: This plot shows a spiking neuron simulated using the integrate and fire model in response to an injected current. No synaptic inputs were simulated in this cell. The top plot shows the relative transmembrane potential ($v_m = V_m - V_{rest}$). T_{ref} represents the absolute refractory period. Notice that the transmembrane potential is set to the resting potential after each generated action potential. Also, notice that the transmembrane potential is set to an arbitrarily high number when the threshold potential (V_{th}) is crossed, indicating the generation of an action potential. The lower plot shows the injected current waveform.

potassium ionic current's dynamics are described by four identical gating particles (n -particles). The gating particle n is called the potassium activation particle. It is called an activation particle because it causes an increase in conductance with increasing depolarization. g_K represents the potassium ionic current conductance, n the potassium activation particle coefficient and τ_n the gating particle time constant, \bar{g}_K the maximum potassium conductance, and n_∞ is the steady state n value at the current transmembrane potential. In the model, the n variable can be described as the fraction of gating particles open and allowing ionic current flow. α_n and β_n are the rate constants and are dependant only on the relative transmembrane potential, v_m ($= V_m - V_{rest}$).

$$g_K(t, v_m) = \bar{g}_K n^4(t, v_m) \quad (2.5)$$

$$\frac{dn}{dt} = \frac{n_\infty - n}{\tau_n} \quad (2.6)$$

$$n_\infty = \frac{\alpha_n}{\alpha_n + \beta_n} \quad (2.7)$$

$$\tau_n = (\alpha_n + \beta_n)^{-1} \quad (2.8)$$

$$\alpha_n = \frac{0.01(10 - v_m)}{\exp \frac{10 - v_m}{10} - 1} \quad (2.9)$$

$$\beta_n = 0.125 \exp \frac{-v_m}{80} \quad (2.10)$$

The model for sodium ion current dynamics is similar to the potassium model, but it depends on two different types of gating particles. The m particle models the sodium activation particle. The h particle models the sodium inactivation particle because it causes a decrease in the conductance in response to a depolarization. The mathematical expressions for the m and h gating particles are similar to that of the n potassium activation particle. The full set of differential equations that describes their behavior are:

$$g_{Na}(t, v_m) = \bar{g}_{Na} m^3(t, v_m) h(t, v_m) \quad (2.11)$$

$$\frac{dm}{dt} = \alpha_m(1 - m) - \beta_m m \quad (2.12)$$

$$\frac{dh}{dt} = \alpha_h(1 - h) - \beta_h h \quad (2.13)$$

$$m_\infty = \frac{\alpha_m}{\alpha_m + \beta_m} \quad (2.14)$$

$$\tau_m = (\alpha_m + \beta_m)^{-1} \quad (2.15)$$

$$h_\infty = \frac{\alpha_h}{\alpha_h + \beta_h} \quad (2.16)$$

$$\tau_h = (\alpha_h + \beta_h)^{-1} \quad (2.17)$$

$$\alpha_m = \frac{0.1(25 - v_m)}{\exp \frac{25 - v_m}{10}} - 1 \quad (2.18)$$

$$\beta_m = 4 \exp \frac{-v_m}{18} \quad (2.19)$$

$$\alpha_h = 0.07 \exp \frac{-v_m}{20} \quad (2.20)$$

$$\beta_h = (\exp \frac{30 - v_m}{10} + 1)^{-1} \quad (2.21)$$

The complete Hodgkin-Huxley current model for a neuron is:

$$C_m \frac{dV_m}{dt} = \bar{g}_{Na} m^3 h (E_{Na} - V_m) + \bar{g}_K n^4 (E_K - V_m) + g_m (V_{rest} - V_m) + I_{inj}(t) \quad (2.22)$$

C_m represents the membrane capacitance, g_m the membrane leakage conductance, V_{rest} the membrane resting potential and I_{inj} the injected current.

Using the set of differential equations described above, we can compute the resulting membrane currents necessary to determine the transmembrane potential. This model, though more computationally intensive, is able to reproduce most of the physiological characteristics of neural transmembrane potential behavior (accurate action potential waveform shape, refractory period, hyperpolarization, etc.) to various external stimuli (injected currents, synaptic inputs, etc.).

2.2 The Auditory System

2.2.1 The Auditory Periphery

The auditory periphery is the first stage of the auditory system. It is divided into three sections: (i) the outer ear, (ii) the middle ear and (iii) the cochlea. The auditory periphery's main function is to convert the information of incoming sounds (intensity, frequency and direction) into electrical signals that are transmitted by neurons throughout the brain. An illustration of the anatomy of the auditory periphery in human beings can be seen in Figure 2.8.

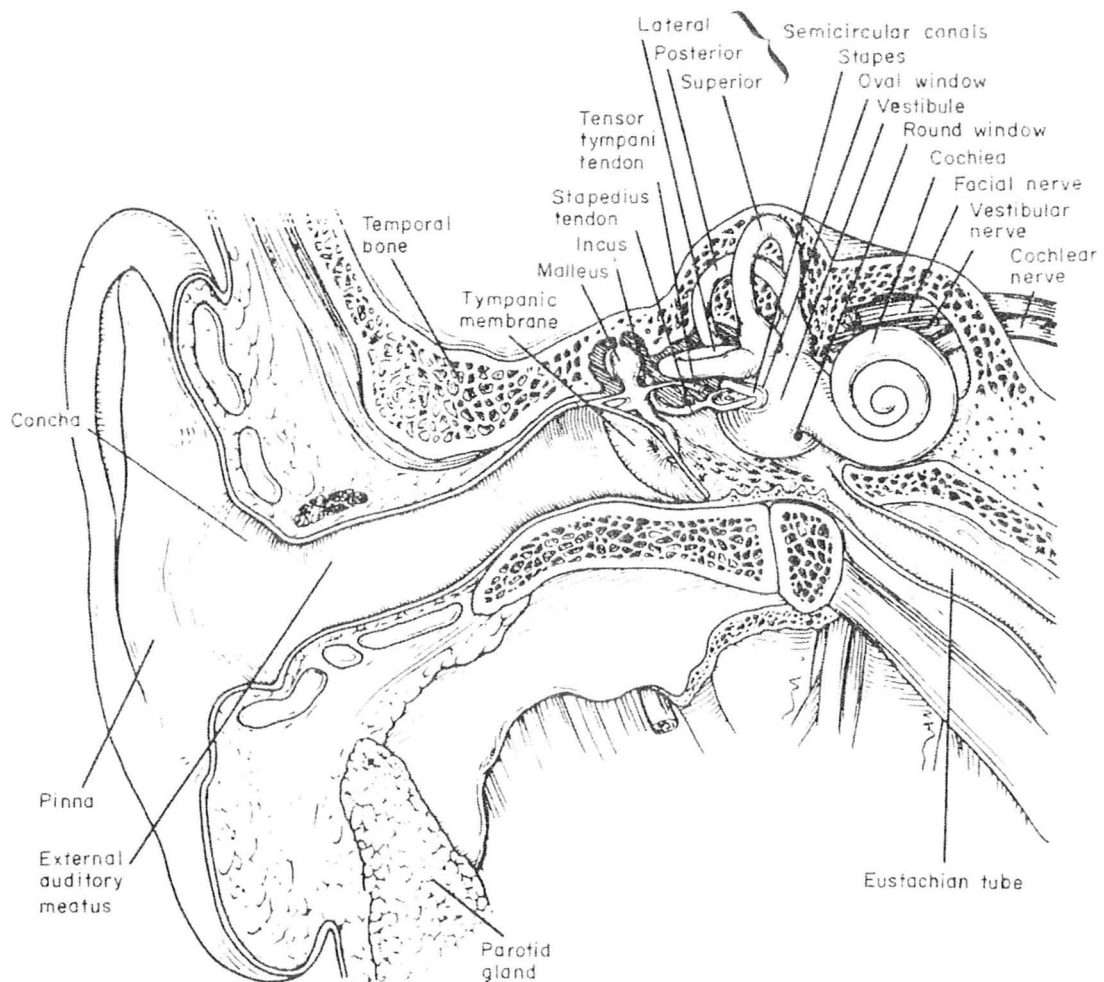


Figure 2.8: The human auditory periphery. (Reprinted from Pickles (2008))

2.2.1.1 The Outer and Middle Ears

The outer ear consists of the pinna, the concha and the external auditory meatus. The outer ear provides the auditory system with two main functions: (i) providing pressure gain to the tympanic membrane and (ii) providing directionality cues to aid in the process of sound localization.

The pinna is a cartilaginous flange. It collects incoming sound waves over a larger area and funnels them through the resonant cavity, called the concha, and then into the canal (external auditory meatus). The process of collecting all of these incoming sound waves and funneling them into the much smaller meatus canal results in an increase in pressure at the tympanic membrane. The complex shape of the external ear creates a frequency dependant sound pressure gain at the tympanic membrane. The maximum gain in humans is typically 15-20 dB, with a broad peak centered around 2.5 kHz. In that frequency region, the length of the concha and meatus canal is approximately one quarter wavelength long which results in a dominant resonance.

The complex shapes of the pinna and concha are also of tremendous importance in providing directionality cues for sound localization. A sound will have a larger intensity in the ear closest to its source. However, the intensity of the sound itself is not enough information to determine whether or not the source of the sound is above, below, behind or in front of the subject. The raised ridges of the pinna and concha cause unique reflections of sound waves into the external auditory meatus in a way that depends on the direction of the incident waves. Reflected waves will arrive in the meatus after direct waves and will result in interference (destructive or constructive depending on the direction). Figure 2.9 shows examples of the effect the direction of an incident sound has on average pressure gain in the human external ear (A) and cat external ear (B).

Once the outer ear has performed its pressure gain function, the sound waves enter the middle ear. The middle ear acts like a transformer to match the impedance of the external auditory meatus to the higher impedance of the cochlear fluids that follow. This prevents the reflection of incident sound from the cochlea. This process is performed, mainly, by the tympanic membrane and three small bones known as ossicles. These bones are called the malleus, the incus and the stapes. An illustration of their shape and orientation can be seen in Figure 2.10.

Sound waves from the meatus strike the tympanic membrane and cause it to vibrate. This, in turn, causes the malleus and incus to rotate together and transfer the force from the tympanic membrane. The malleus and incus are connected rigidly so that the bones rotate together acting as levers. The force is then transferred to the stapes. The stapes is attached to a flexible window in the wall of the cochlea, known as the oval window.

The anatomy of the middle ear achieves impedance matching by two principles. The first is that the area of tympanic membrane is much larger than that of the stapes

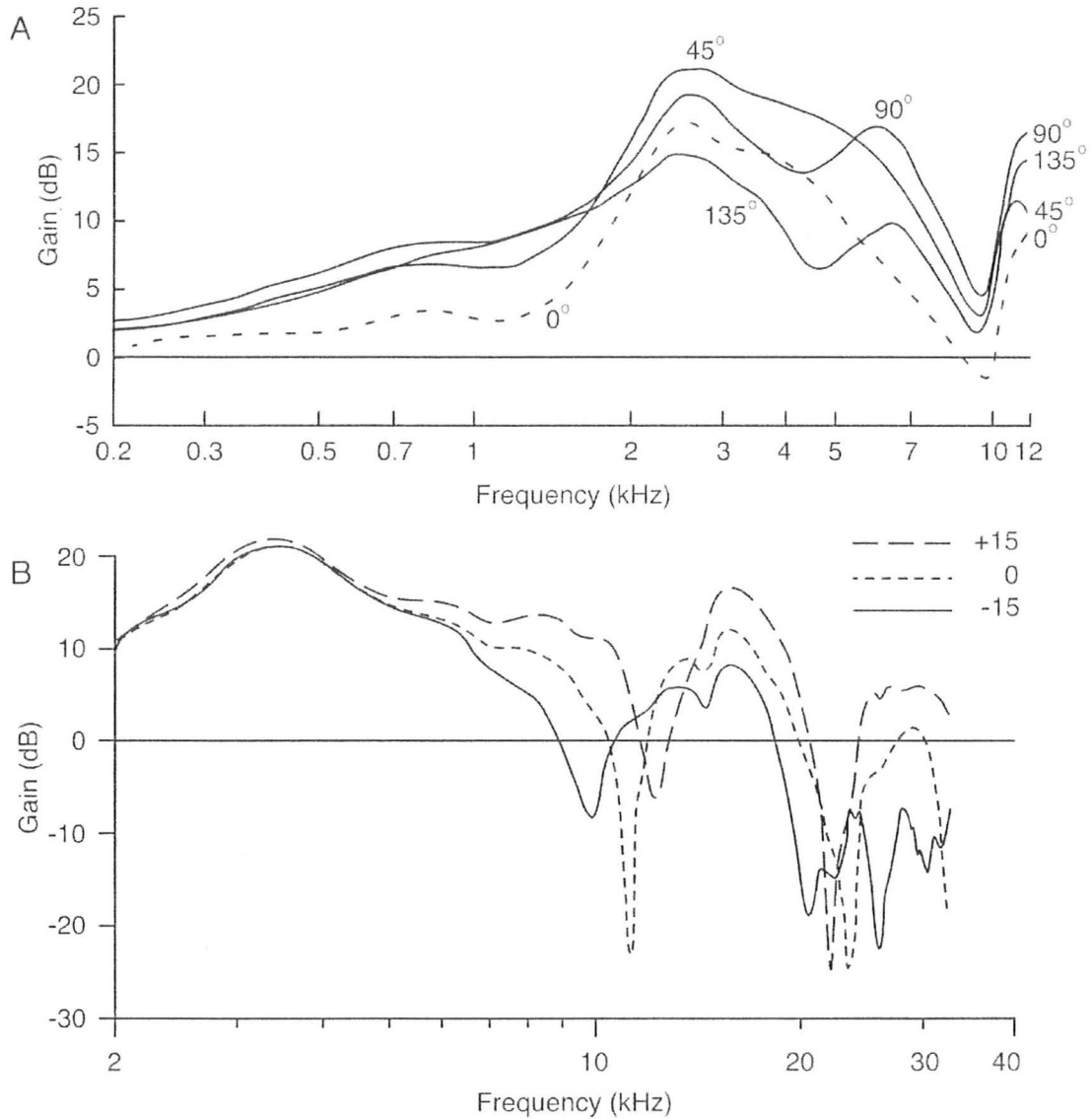


Figure 2.9: Figures show the effect the direction of a sound source has on pressure gain in humans (A) and cats (B). (A) A sound is presented to the human ear at different orientations in the vertical plane. Zero degrees indicates straight in front of the head. (B) The change in gain in the cat external resulting from changes in elevation of a sound source in the vertical plane. In both figures, zero degrees indicates a position straight in front of the head. Average sound pressure gain of the human and cat external ear is plotted against the frequency spectrum of a sound. (Figure 2.2 reprinted from Pickles (2008))

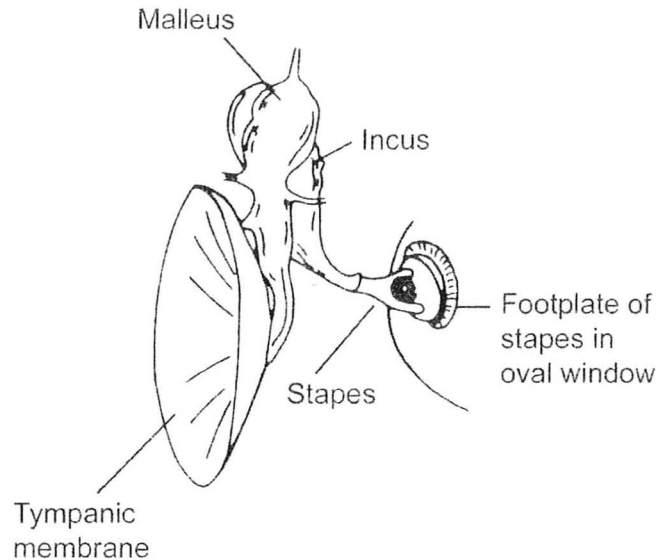


Figure 2.10: Physiology of middle ear. Connection of tympanic membrane and ossicles (malleus, incus and stapes) to oval window shown. (Reprinted from Pickles (2008))

footplate. The force collected over the tympanic membrane is therefore applied to a much smaller area, resulting in an overall pressure increase at the oval window. This is said to be the primary method by which impedance matching is achieved in the middle ear (Pickles, 2008). The second principle is of the lever action of the ossicles. The arm of the incus is much shorter than the arm of the malleus. This produces a lever action that increases the force and decreases the velocity at the stapes.

By these simple principles, we would expect a constant pressure gain to be produced by the middle ear. In actual fact, this is not the case. The transfer function of the middle ear in both humans and cats can be seen in Figure 2.11 below. At lower frequencies there is a lesser pressure gain in the middle ear. This can be attributed to the elastic stiffness of the tympanic membrane and the ligaments of the middle ear bones. For a constant sound pressure level, the displacement of air is inversely proportional to the frequency of the sound. Lower frequencies will attempt to induce more motion in the tympanic membrane and ossicles which is partially counteracted by the elastic stiffness of that region. The effectiveness of the pressure gain at high frequencies is also slightly decreased. This is due to several factors. At high frequencies, it has been shown that the vibration pattern on the tympanic membrane breaks up into separate zones, reducing the effectiveness of transmission. The ossicular chain also begins to flex at high frequencies, further reducing its effectiveness. The maximum of the middle ear transfer function occurs around 1 kHz. In this frequency

region, the aforementioned phenomena have the minimum effect on the impedance matching function of the middle ear.

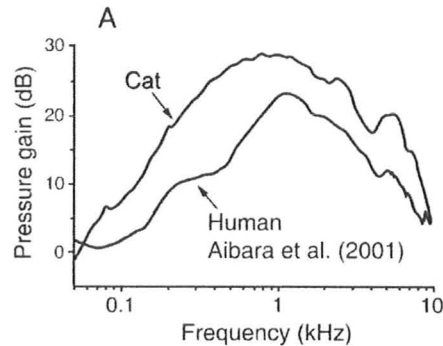


Figure 2.11: Shows the transfer functions of the middle ear in cats and humans. The figure shows pressure gain (dB) plotted as a function of frequency (kHz). Note that the cat middle ear is able to provide greater gain than the human middle ear at virtually all frequencies. The transfer function of the cat also has a slight dip in gain that occurs at the 4 kHz range of the frequency spectrum. (Figure 2.6 A reprinted from Pickles (2008))

Transmission through the middle ear can also be controlled by the middle ear muscles. The middle ear muscles are two striated muscles attached to the ossicles. The tensor tympani muscle attaches to the malleus near the tympanic membrane and the stapedius muscle attaches to the stapes from the wall of the middle ear. These muscles contract to increase the stiffness in the ossicular chain. By increasing the stiffness of the ossicular chain, we can reduce the transmission of low-frequency sounds. Several functions have been suggested for these muscles (Pickles, 2008): (i) contraction to loud sounds to prevent ear damage, (ii) attenuation of persistent, high-intensity, low-frequency stimuli and (iii) attenuating low frequencies to prevent the masking of high-frequency stimuli at high sound intensities.

2.2.1.2 The Cochlea

The cochlea is a seashell-shaped structure connected to the ossicles by the stapes footplate (Figure 2.8). It is divided into three main regions, called *scala*. The three *scala* are the *scala vestibuli*, the *scala tympani* and the *scala media*. These regions spiral throughout the cochlea maintaining their spatial orientations throughout the cochlea (Figure 2.12). The *scala tympani* and *scala vestibuli* are joined at the apex of the cochlea by an opening called the *helicotrema*. The *scala media* is separated from the *scala vestibuli* by *Reissner's membrane* and from the *scala tympani* by the *basilar membrane*. A cross-section of the spiraling cochlear duct can be seen in Figure 2.13.

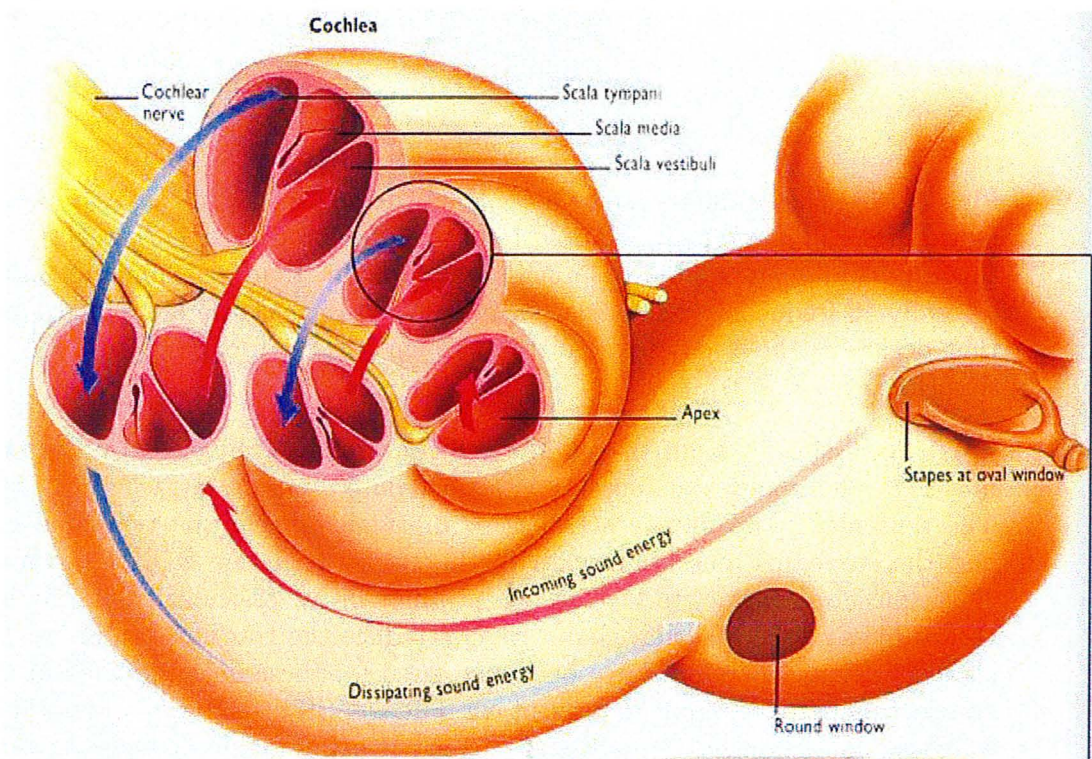


Figure 2.12: Illustration of the physiology of the cochlea. Note the spiraling cochlear duct. (Reprinted from universe-review.ca (2009))

Each scala is filled with a form of fluid. The scala vestibuli and scala tympani are filled with a fluid called perilymph. Perilymph has an ionic concentration similar to extracellular fluid (high Na^+ and low K^+ concentration). The scala media is filled with endolymph. Endolymph is similar to intracellular fluid in ionic concentrations (low Na^+ and high K^+ concentration) and is also at a high positive potential (+80mV) (Pickles, 2008). This high potential is actively maintained by the stria vascularis.

At the end of the scala vestibuli and scala tympani are two openings called the oval window and round window, respectively. The vibrations of the middle ear are transferred to the oval window by the stapes. This causes a displacement of fluid in the cochlea from the scala vestibuli, through the helicotrema and into the scala tympani. This fluid flow causes a wavelike displacement of the basilar membrane.

Attached to the basilar membrane is the organ of Corti (Figure 2.14). The organ of Corti acts like an audio transducer, detecting the displacement of the basilar membrane and converting it to electrical signals for transmission to the connected auditory nerves. The organ of Corti's shape is maintained by the rigid pillar cells that run along its length. The pillar cells end in the reticular lamina, the upper surface of the organ of Corti at the tectorial membrane. The arch of the organ of Corti is supported by phalangeal cells. The inner phalangeal cells completely surround and support the inner hair cells (IHC). The outer phalangeal cells, or Deiter's cells, hold the basal ends of the outer hair cells (OHC). These outer phalangeal cells also extend up to the reticular lamina providing separation between outer hair cells. On the basal side of the outer hair cells are a group of supporting cells called Hensen's cells. Similarly, on the modiolar side of the organ of Corti is another group of supporting cells.

Resting on the organ of Corti is the tectorial membrane. The tectorial membrane is a gelatinous and fibrous flap composed of collagens and tectorins (molecules unique to the inner ear). The tectorial membrane is only fixed on one end and is attached to the limbus. There are small processes, called trabeculae or marginal pillars that extend from the tectorial membrane to the reticular lamina. The IHCs and OHCs are organized in rows running from the base of the basilar membrane to the apex. There are three to five rows of OHCs in humans. Protruding out of each hair cell are stereocilia. The longer stereocilia of the OHCs are embedded into the bottom of the tectorial membrane. The stereocilia of the IHC fit into a raised groove in the tectorial membrane called Hensen's stripe. When the basilar membrane is deflected up and down, the organ of Corti is pushed up into the tectorial membrane and causes a deflection of the stereocilia extending from the hair cells to the tectorial membrane. The deflection of these stereocilia causes the opening of ion channels in the stereocilia themselves (van Netten *et al.*, 2008).

In IHCs the stereocilia are organized into a relatively straight pattern of three adjacent rows. The stereocilia of the OHCs are organized into three to five, closely

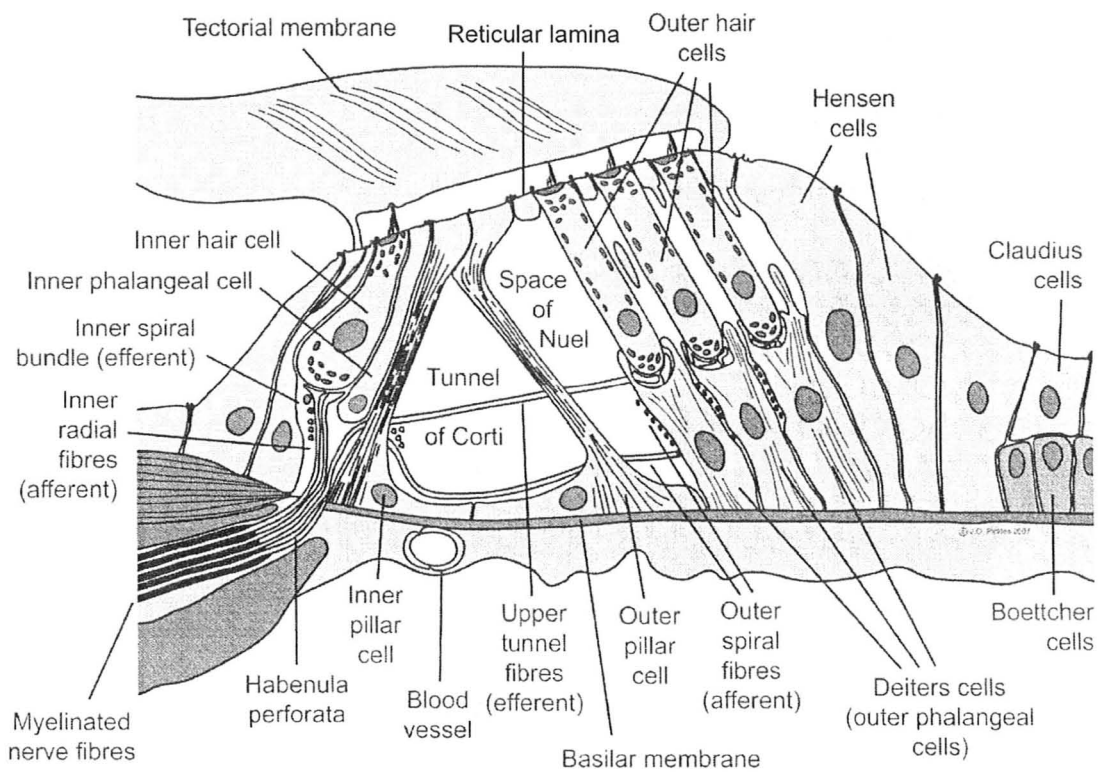


Figure 2.14: Illustration of the organ of Corti. (Figure 3.1D, reprinted from Pickles (2008))

packed V-shaped rows. Electron micrographs of the organ of Corti, with the tectorial membrane removed, can be seen in Figure 2.15 for a further illustration of the arrangement of hair cells and their stereocilia.

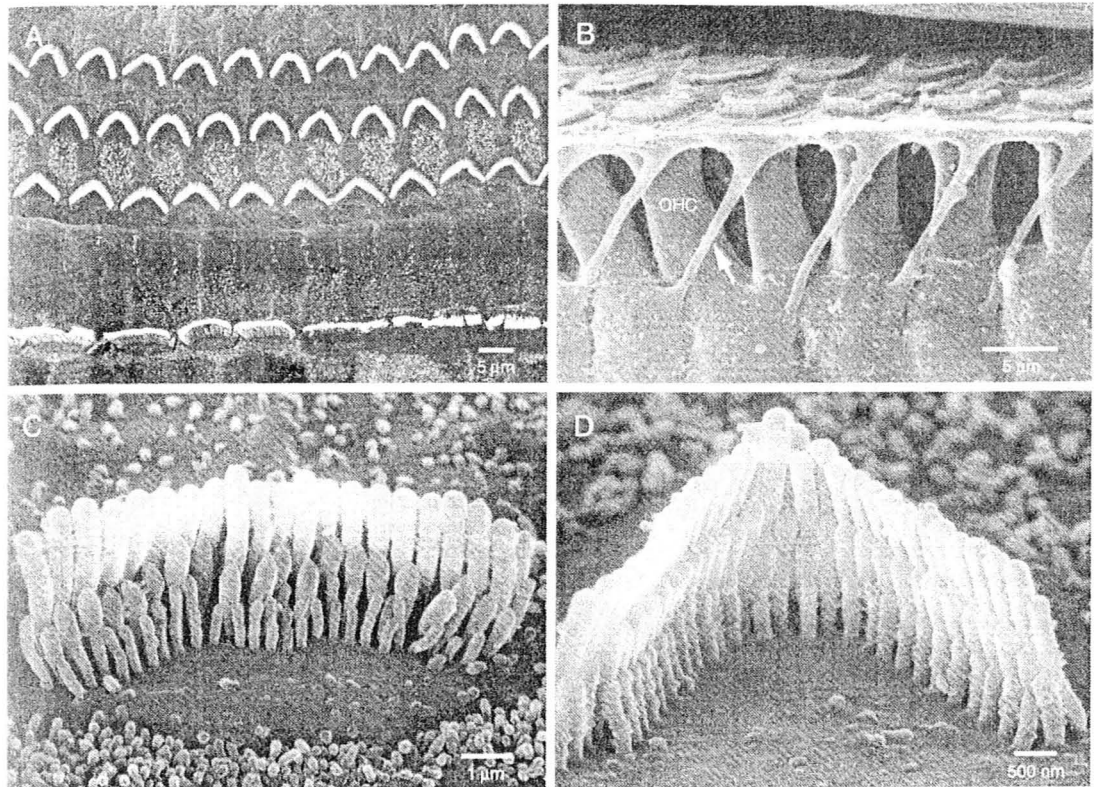


Figure 2.15: Electron micrographs of hair cells in the organ of Corti. (A) Shows the upper surface of the organ of Corti after the tectorial membrane has been removed. Clearly shown are the three rows of OHCs (top) as well as the V-shaped pattern of their stereocilia. The row of IHCs as well as the straight orientation of their stereocilia is also shown (bottom). (B) The phlanges of Deiter's cells (e.g. arrow) are shown. In this micrograph, the supporting cells on the outer edge of the organ of Corti were removed. The micrograph shows a view looking inwards towards the modiolus. (C) A closer view of the straight rows of stereocilia in IHCs. (D) A closer view of the V-shaped rows of stereocilia in OHCs. (Figure 3.4, reprinted from Pickles (2008))

Illustrations of the cross-section of inner and outer hair cells can be seen in Figure 2.16. Each type of hair cell is surrounded by a supporting structure of cells, as described earlier. Protruding from the top of each hair cell are the stereocilia. In both IHCs and OHCs, the tallest stereocilia are located furthest away from the modiolus.

The stereocilia are composed of packed actin filaments giving them a rigid structure so that they behave as levers as a result of mechanical deflection. The rows of stereocilia are connected by links at their tips and on their sides. This causes the rows of stereocilia to move together as a bundle when deflected, opening the mechanotransducer channels. Some of the actin filaments protrude further into the cell forming structures called rootlets. These rootlets connect to another actin filament structure called the cuticular plate. This serves to form a rigid structure to attach the stereocilia to the hair cell body. At the basal end of each hair cell body are afferent and efferent nerve endings. The hair cell membrane near the nerve endings contains synaptic ribbons surrounded by synaptic vesicles. The synaptic ribbon controls the release of neurotransmitters by the synaptic vesicles to ensure a coordinated release for reliable synaptic activation of afferent auditory nerve fibers. The afferent nerve fibers project from the cochlea to the brain stem.

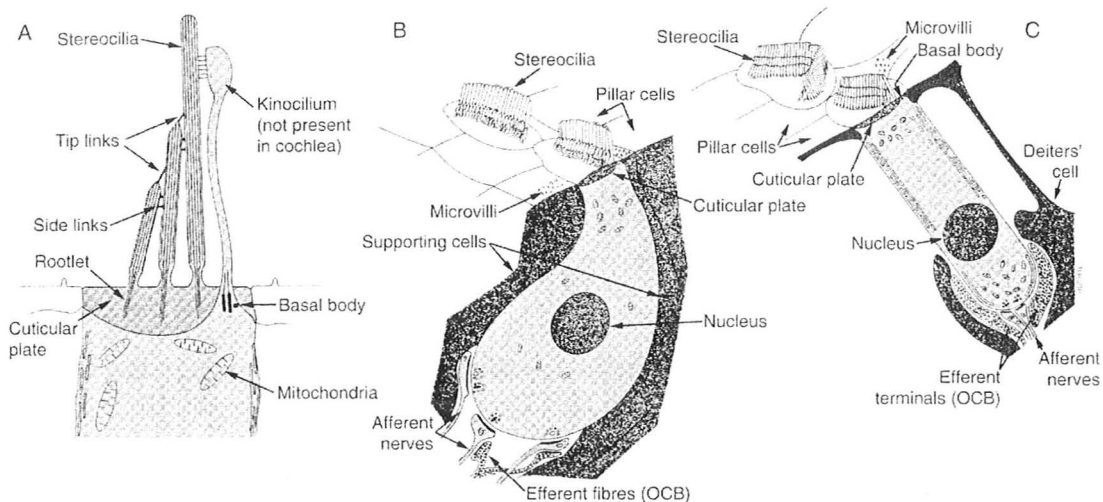


Figure 2.16: (A) An illustration of the organization of the physiology of the stereocilia protruding from hair cells. (B) A cross sectional illustration of inner hair cell physiology. (C) A cross sectional illustration of outer hair cell physiology. (Figure 3.5, reprinted from Pickles (2008))

Auditory nerve fibers enter the organ of Corti through the central cavity of the cochlea, the modiolus and then through the spiral structure of the cochlea. Afferent fibers have their cell bodies in the spiral ganglion on the inner wall of the spiral lamina (see Figure 2.13). There are two types of afferent auditory nerve fibers in the cochlea: (i) type I fibres and (ii) type II fibres. Type I fibres are myelinated and typically connect directly to the IHCs nearest to their point of entry from the spiral ganglion. Type II fibres innervate OHCs. Their axons take a less direct path. They enter from

the spiral ganglion, turn basally for approximately 5 hair cells through the tunnel of Corti on the basilar membrane. They then spiral outwards among the rows of OHCs and connect to approximately 50 different hair cells, generally all in the same row. This can be seen in Figure 2.17. Efferent nerve fibers innervating the OHCs tend to arise from the medial surface of the superior olivary complex. Those innervating the IHCs arise from the lateral region of the superior olivary complex. The connections of the efferent fibres on each type of hair cell are illustrated in 2.16. Note that efferent fibres in IHCs do not connect directly to the cell body, but rather connect to the dendrites of the afferent fibres.

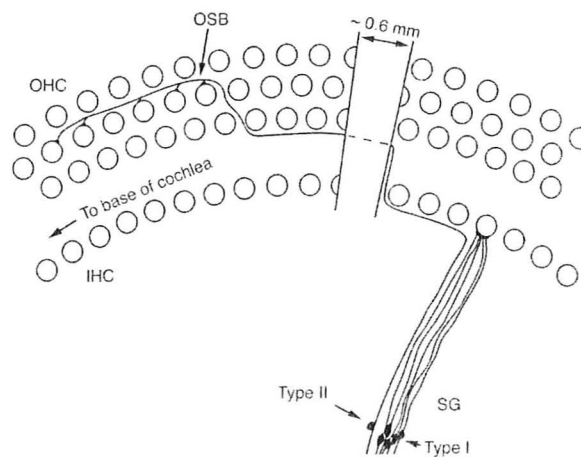


Figure 2.17: Illustration of the innervation pattern of hair cells in the cochlea by AN fibers. The great majority of fibers (Type I fibers) innervate the IHCs directly. Type II fibers are shown running basally for 0.6 mm after which they branch towards the OHCs, continue to run basally and connect to several OHCs in the same row. (Figure 3.6, reprinted from Pickles (2008))

The basilar membrane (BM) plays an extremely important part in the processing of sounds. When the oval window is displaced by the stapes, the cochlear fluids are moved which causes a traveling wave along the basilar membrane. The traveling wave moves apically along the BM. The pattern and position of this traveling wave is dependant on the frequency of the stimulus. In response to a pure tone (sinusoidal) signal, the vibrations in the BM show a sharp peak confined to a narrow region. The location of that peak changes as the frequency of the signal changes. High frequency signals cause peaks closer to the base of the BM (near the stapes) and low frequency signals cause peak vibrations at the apex of the BM (near the round window). The shape of the traveling wave and the effect that frequency can have on position along the BM are illustrated in Figure 2.18.

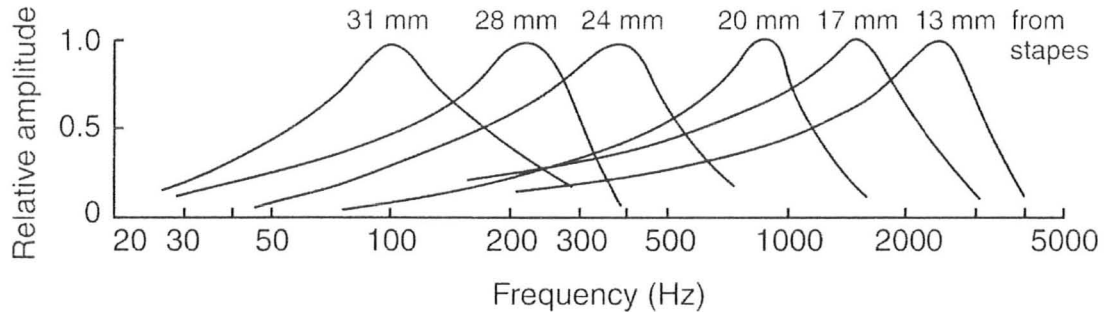


Figure 2.18: This figure shows several traveling waves along the basilar membrane. The relative amplitude of basilar membrane (BM) vibrations at a particular point along the BM are plotted over a range of frequencies. Above each wave is the distance of the recorded point measured from the stapes. We see that each point is most responsive at a particular frequency called the characteristic frequency (CF). The figure also shows that the membrane is more responsive to low frequency signals away from the stapes and to high frequency signals near the stapes. We also see that a point on the membrane does not vibrate significantly to tones not near its CF. (Figure 3.9, reprinted from Pickles (2008))

The response of the BM is also dependant on the intensity of the stimulus. Larger stimulus intensities tend to cause larger vibrations in the BM over a much larger area. This effect, however, is nonlinear. Figure 2.19 shows these behaviors. The plots show measurements of the vibrations of the basilar membrane at one point on the membrane. The figure on the left shows that, for low intensity signals, we see that the BM vibrates only in response to a stimulus at a particular frequency. As the intensity is increased, the size of the BM vibrations increases. We also see that the BM will vibrate in response to broader range of frequencies as well (Ruggero *et al.*, 1997). The figure on the right shows that this effect is non-linear. Eventually, increases in the intensity of the stimulus do not result in proportional increases in the vibration of the BM.

The properties of basilar membrane just discussed are illustrated further in Figure 2.20, in a plot called a tuning curve. It shows the various combinations of stimulus frequency and stimulus intensity that result in identical displacements of the BM at a particular point. The shape of this curve is extremely important in that hair cells and the auditory nerve (AN) fibers that innervate them have identical response properties. This implies that the properties of the BM are primarily responsible for the responses of AN fibers.

The hair cells provide the link between the mechanical response of BM and the electrophysiological response of the AN fibers. As discussed earlier, the movement

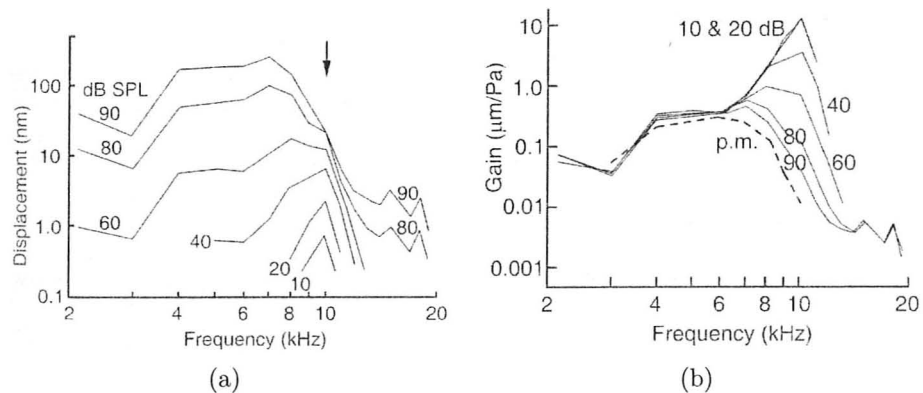


Figure 2.19: These figures show the effect stimulus intensities have on the vibrations of the BM. (a) shows the amplitude of vibrations at a single point in response to several tones of different intensities. This particular point has a CF of approximately 10kHz and is indicated by the arrow. As stimulus intensity increases, the overall vibrations at the point is increased and the point becomes more responsive to a wider range of frequencies. (b) shows the BM gain plotted over frequency at a point. The fact that the curves do not overlap shows that the gain provided by the BM for increased stimulus intensity is not linear. At high intensities the BM actually attenuates the signal slightly whereas there is a significant gain at the CF with low intensity signals. ((a) Figure 3.11 A and (b) figure 3.13 B reprinted from Pickles (2008))

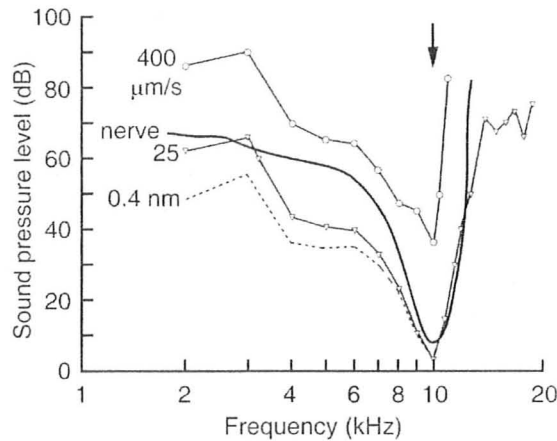


Figure 2.20: Shows the basilar membrane tuning curve for several different BM displacements. We see that larger displacements require larger overall stimulus intensities. The thick line indicates the tuning curve of AN fibers with similar CFs. We see that the shape of AN fiber tuning curves is identical to that of the BM tuning curve. The BF at this particular point along the BM is indicated by the arrow. (Figure 3.11 B reprinted from Pickles (2008))

of the BM causes the organ of Corti to move up against the tectorial membrane causing the deflection of the stereocilia protruding from the hair cells. The mechanical deflection of these stereocilia opens ion channels in the stereocilia (van Netten *et al.*, 2008). The scala media is filled with endolymph, a high K^+ concentration fluid that has an electrochemical potential of approximately $+80\text{mV}$. The intracellular potential of the hair cells ranges from -45 to -70mV . The electrochemical gradient will thus force K^+ ions from the endolymph into the hair cell body. The resulting intracellular depolarization triggers the release of the neurotransmitters that activate the efferent AN fibers. Intracellular recordings of IHC potentials have shown the types of responses shown in Figure 2.21. Hair cell potentials are made of two elements, a DC component and an AC component. As stimulus frequency is raised, the AC component of the response decreases in amplitude relative to the DC component. This is due to the fact that the capacitance of the hair cell membrane produces low-pass filtering of the response with a cutoff of approximately 1 kHz.

2.2.2 Auditory Nerve Fibers

AN fibers provide the means of communicating the information in auditory signals to the central auditory system for processing. Their response properties are determined, primarily, by the BM, IHC and OHC response properties. AN responses to pure tone

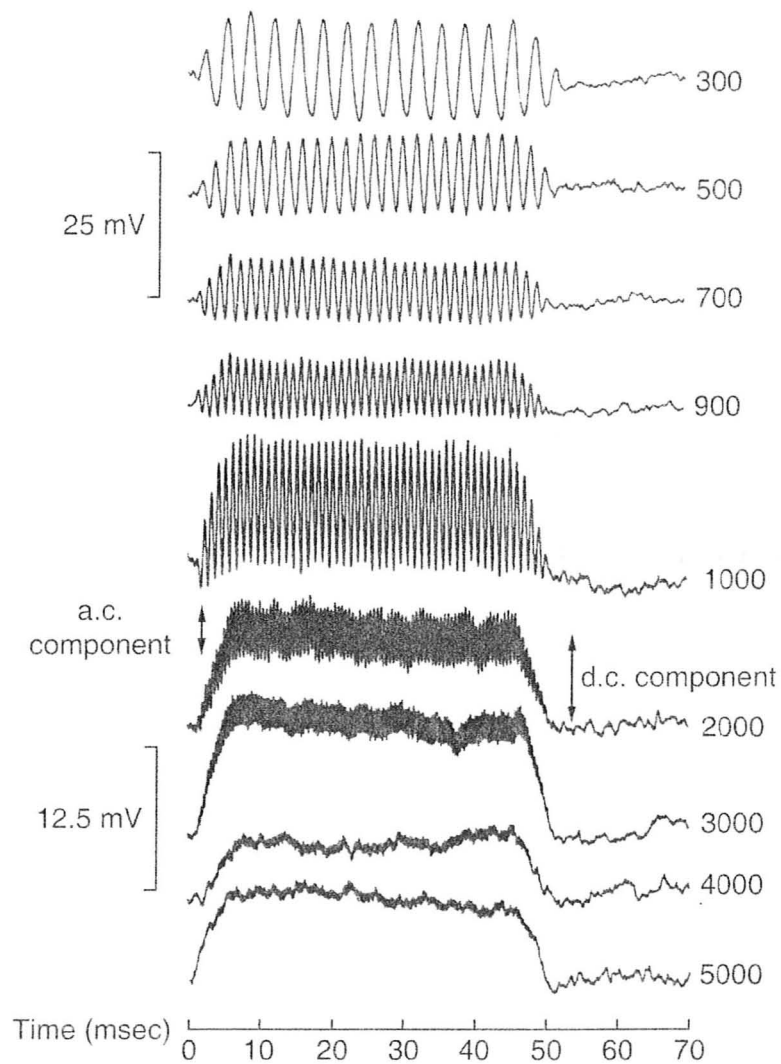


Figure 2.21: Figures of inner hair cell voltage changes in response to various frequencies. As frequency (numbers on the far right of each curve) is increased, the size of the a.c. component relative to the d.c. component decreases. (Figure 3.21 reprinted from Pickles (2008))

stimuli are typically shown in the form of a post-stimulus-time-histogram (PSTH). A PSTH shows the number of spikes that occur in a particular time period of several repetitions of an applied auditory stimulus. A typical PSTH of an AN fiber responding to a pure-tone stimulus can be seen in Figure 2.22. We can see that AN fibers produce a very sharp onset response when the tone is first presented. The response then drops sharply during the first 10-20 ms after the stimulus is applied. The drop in activity then decreases extremely slowly for the remainder of the stimulus (Pickles, 2008).

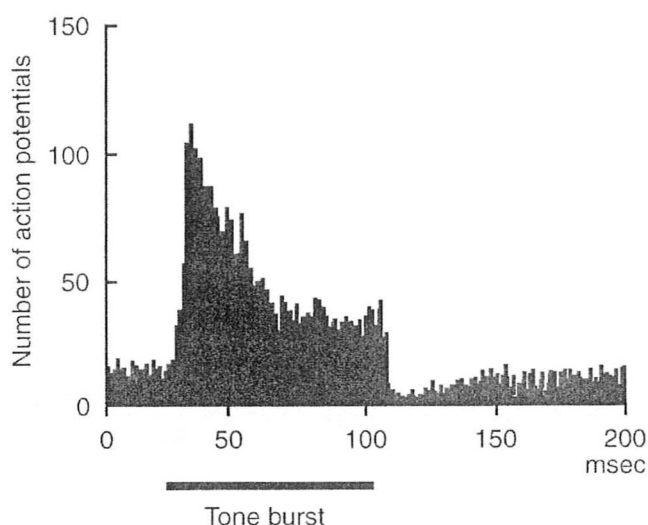


Figure 2.22: Post-stimulus time histogram of an AN fiber in response to a tone burst. Number of action potentials in each time bin are plotted against elapsed time. The duration of the tone burst is shown by the black bar below the elapsed time axis. AN fiber PSTHs in response to a tone stimulus are characterised by a sharp onset peak followed by a steep decline in firing rate leading to an eventual sustained firing period for the remaining duration of the stimulus. The action potentials in bins where a tone is not being presented represent the spontaneous firing behavior of the AN fiber. (Figure 4.3 reprinted from Pickles (2008))

We can see from the PSTH that AN fibers still fire action potentials well after the stimulus tone has ceased being applied. This tendency of AN fibers to fire action potentials even when there is no applied stimulus is called the spontaneous behavior of an AN fibre. AN fibers tend to fire spontaneously at a rate called the spontaneous rate (SR). The SR and characteristic frequency (CF) are the two variables that are used to characterize individual AN fibers.

Recorded AN fibers have shown a broad range of SRs which have been used to separate them into three different groups: (i) high SR fibers ($SR > 20$ spikes/s),

(ii) medium SR fibers ($0.5 < \text{SR} < 20$ spikes/s) and (iii) low SR fibers ($\text{SR} < 0.5$ spikes/s). Approximately, 25% of AN fibers are low and medium SR fibers, with most of that group being low SR fibers. The rest of the population of AN fibers are high spont fibers whose mean SR is located at around 60-80 spikes/s. The maximum recorded SR for an AN fiber, to date, is 120 spikes/s (Evans, 1972). Physiological studies have shown that differences in the spontaneous behavior of AN fibers are due to specialization of the synapse between each fiber and the IHC. In addition, high SR fibers tend to be much thicker than other types of AN fibers and they tend to innervate IHCs on their pillar (OHC) side. Low and medium SR fibers are thinner and tend to innervate IHCs on the opposite side (Pickles, 2008).

Figure 2.23 below shows the tuning curves of AN fibers with several different CFs. AN fiber tuning curves plot the firing thresholds (in dB SPL) of a particular AN fiber over a broad range of stimulus frequencies. The threshold is defined as the lowest intensity at which a detectable increase in firing rate, over the AN SR, is observed. While there are slight variations between the tuning curves of different AN fibers, there are several common characteristics. The first is that each AN fiber tuning curve shows an absolute minimum threshold at CF. It is derived from the CF of the BM where the IHC innervating a particular AN fiber is located. The second feature common to all tuning curves is that they show an asymmetrical band-pass filter shape. Each tuning curve shows a bandpass region centered around a CF with a “tail” region in frequencies below CF.

The tuning curves shown in Figure 2.23 show a variation in shape depending on the CF of the AN fiber. Some fibers have thinner bandpass regions than others implying some are more frequency selective than others. In order to quantify this frequency resolution, a Q or “quality” factor is used. The Q_{10} factor is defined as

$$Q_{10} = \frac{\text{CF}}{\text{BW}_{10\text{dB}}} \quad (2.23)$$

where $\text{BW}_{10\text{dB}}$ is the bandwidth of the AN fiber tuning curve at 10 dB SPL above the CF threshold. A large Q_{10} factor indicates a relatively narrow tuning curve bandwidth and thus a large level of frequency selectivity. Figure 2.24 shows the Q_{10} factors of several AN fibers plotted against their CFs. We can see that higher CF fibers are more frequency selective than low frequency AN fibers.

Figure 2.25 shows rate-intensity curves of AN fibers with several different CFs and several different spontaneous rates. Rate-intensity curves show the firing rate of an AN fiber plotted against the stimulus intensity for a tone stimulus. We see that the rate-intensity relationship of AN fiber responses has a non-linear, sigmoidal shape. At low stimulus intensities (around or below threshold) the rate-intensity relationship is constant near the SR of the fiber because the applied stimulus is not yet strong enough to significantly excite the AN fiber. As the threshold is crossed,

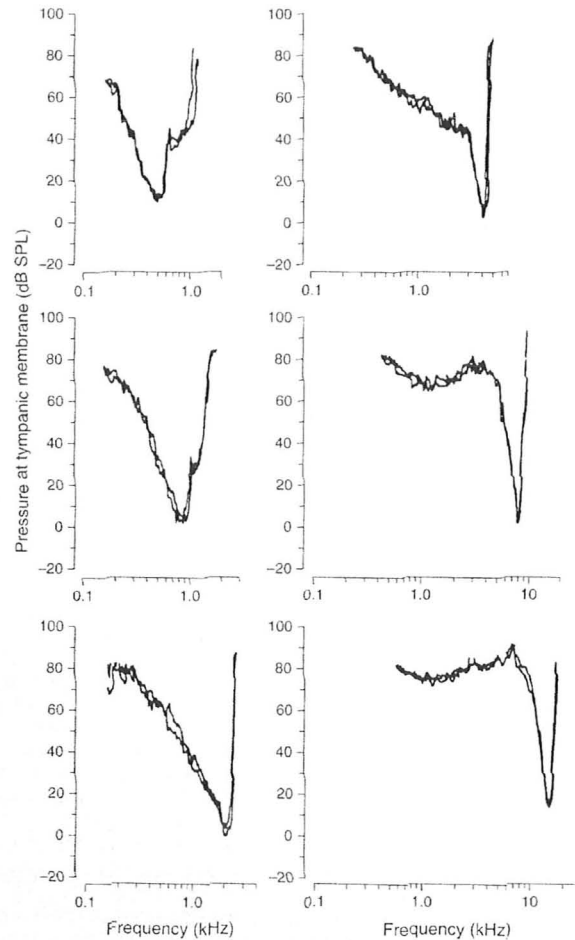


Figure 2.23: Threshold tuning curves of different AN fibers with varying CFs. Tuning curves for two fibers with similar CFs are shown in each plot. A threshold tuning curve shows the minimum threshold (in dB SPL) of excitation of the particular AN fiber for tone stimuli of varying frequencies. Common across all fibers is an overall minimum threshold at CF. Fibers with higher CF (such as that in the bottom right) have much thinner regions of excitation around CF and prominent tails at frequencies below CF. The tuning curves shows that AN fibers are not responsive to tone stimuli with frequencies significantly greater than CF. (Figure 4.4 reprinted from Pickles (2008))

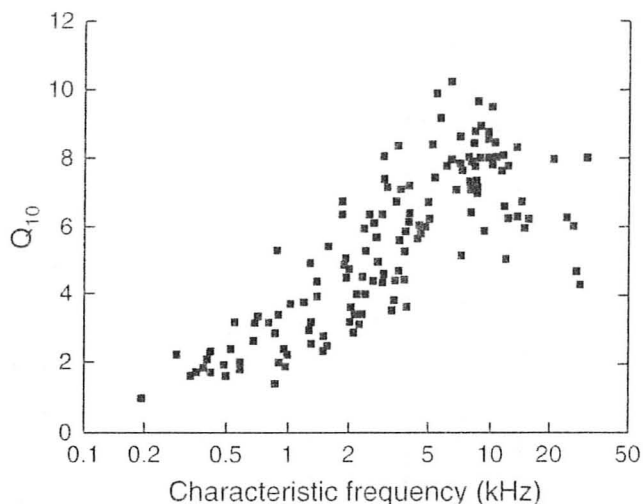


Figure 2.24: AN fiber Q_{10} values are plotted against CF for a large population of fibers. Q_{10} values can be seen to rise with rising CF indicating that fibers with higher CFs have a greater degree of frequency selectivity than those with low CFs. (Figure 4.6 B reprinted from Pickles (2008))

we see sharp increases in the AN fiber firing rate in response to increased stimulus intensity. Eventually, the rate-intensity curve begins to flatten out and saturates as stimulus intensity is increased because the AN fiber can no longer be driven any harder. The slope of the increasing region of the rate-intensity function is dependant on the frequency of the stimulus (as seen in Figure 2.25). At frequencies slightly above and below the CF of the fiber, the slope is fairly close to the one shown at CF however, the rate-intensity has a higher threshold. This is similar to the relationship shown by the tuning curves in Figure 2.23. At frequencies far below CF (e.g. in the “tail” region), the slope is extremely low and it takes a very loud stimulus to drive AN fiber above threshold. The slope of the rate-intensity curve is also dependant on the SR of the fiber. Figure 2.25 shows that the slope of the rate-intensity curve decreases with SR. High SR fibers have a much lower dynamic range than low spont fibers. We can also see from this figure that high SR fibers have significantly lower thresholds of excitation than medium and low SR fibers (Pickles, 2008).

While AN fibers are most easily excited by tonal stimuli at their CFs, it is not always a CF tone that causes an AN fiber to fire at its strongest possible rate. Figure 2.26 shows iso-intensity curves for an AN fiber with a CF of approximately 2 kHz. Iso-intensity curves show the firing rate plotted against stimulus frequency for tones presented at an identical stimulus intensity. We see that at lower stimulus intensities the maximum firing rate achieved by the applied stimuli occurs at CF, as expected.

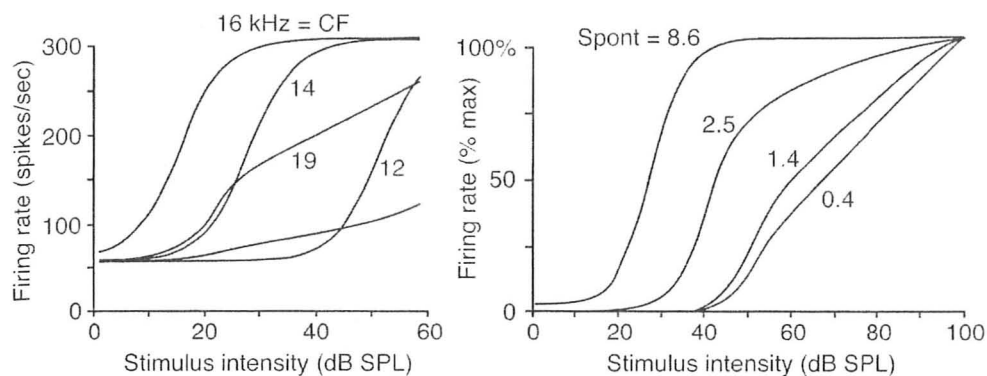


Figure 2.25: (Left) Rate-intensity curves of an AN fiber with a CF of 16 kHz receiving tonal stimuli with a variety of frequencies. At the CF the AN fiber has its minimum threshold of excitation and saturates to its maximum firing rate most quickly. The rate-intensity curve is as steep for frequencies below CF. Above CF, the rate-intensity curves are much less steep. The behaviors are similar to the basilar membrane. (Right) Rate-intensity functions of several AN fibers with different spontaneous firing rates, simulated at CF. Firing rate is plotted as a percentage of the maximum firing rate of each fiber. We see that fibers with high spontaneous rates have significantly lower thresholds and saturate much more quickly than fibers with low spontaneous rates. (Figure 4.7 reprinted from Pickles (2008))

However, at high stimulus intensities we see that the maximum firing rate occurs with a stimulus frequency around 1 kHz. This shift in the “best frequency” (BF) effect is reversed for AN fibers with a CF below 1 kHz (Pickles, 2008).

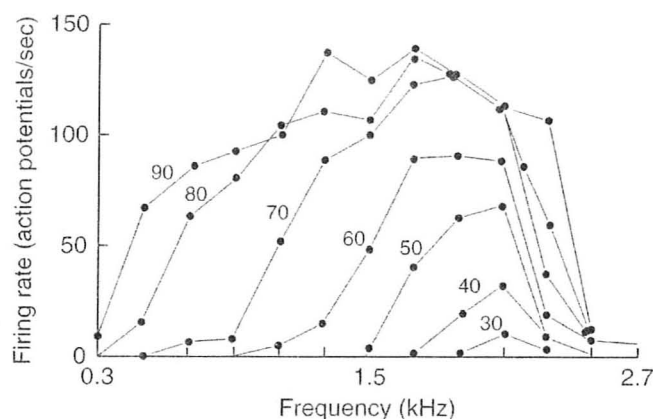


Figure 2.26: Iso-intensity curves of an AN fiber with a CF of approximately 2 kHz. Each curve on the figure represents the firing rate of the AN fiber in response to a variety of pure tone stimuli all presented at the same intensity. Intensities of each curve are noted next to each line. (Figure 4.8 B reprinted from Pickles (2008))

Studies of AN responses have shown an ability of fibers to phase-lock to low-frequency stimuli (Johnson, 1980). This is illustrated in the period histograms shown in Figure 2.27. Period histograms are similar to PSTHs except that instead of plotting the occurrence of spikes over the entire length of the presented stimulus, the occurrence of spikes is plotted over the length of one period of the presented tonal waveform. The resulting period histogram resembles a half-wave rectified form of the applied stimulus. This is due to the nature of IHC responses to tone waveforms. They are most excitatory on the upwards push of the BM towards the scala vestibuli and hyperpolarize when the BM is deflected in the opposite direction. A study by Palmer and Russell (1986) showed that phase-locking declines with a decrease in the a.c./d.c. ratio in the responses of IHCs. It appears that the average firing rate of an AN fiber is determined by the d.c. response of its IHC and its ability to synchronize to a tone is determined by how pronounced the a.c. response is from the d.c. response. The low-pass filtering of signals by the IHC membrane is the reason why AN fibers are only able to phase lock to low-frequencies.

AN fibers do not have any inhibitory behaviors in their responses to tonal stimuli. However, an interesting phenomenon known as two-tone suppression occurs which can cause a decrease in the excitability of an AN fiber. Two-tone suppression occurs when a suppressive tone is “turned on” during the presentation of an excitatory tone. This

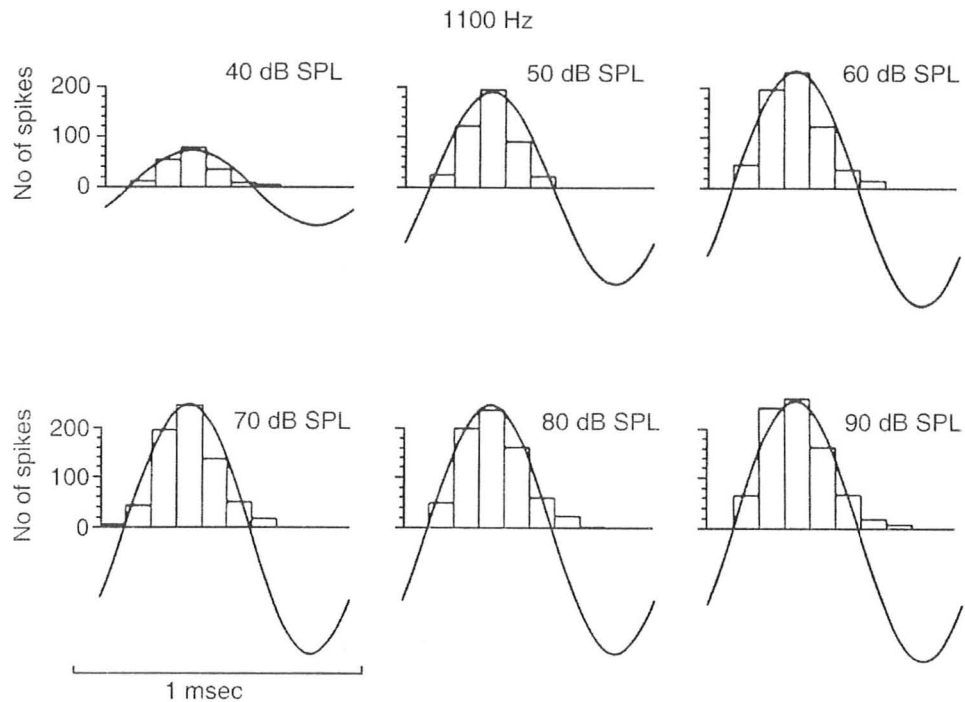


Figure 2.27: PSTHs of a fiber activated by a low frequency tone (1100 Hz) at various stimulus intensities. Note the tendency of the of the AN fiber to fire only during one half of the tone cycle and to fire more strongly as stimulus intensity is increased. Sinusoids of best fit are shown on each PSTH. Note that the overall firing rate does not increase after 70 dB as the AN fiber has reached its saturated firing rate. The saturation of the firing rate does not affect the ability of the fiber to phase lock to the tone stimulus. (Figure 4.9 reprinted from Pickles (2008))

causes inhibition in the response of an AN fiber as the result of a stimulus that, on its own, would not cause any inhibition (Pickles, 2008). Figure 2.28 shows a PSTH of an AN fiber that is undergoing two-tone suppression. We see that the response during the presentation of the suppressive tone is the opposite of that shown in Figure 2.22. At the onset of the suppressive tone there is significant suppression of the AN fiber. Gradually, the firing rate of the AN fiber increases as the suppressive tone continues, contrary to the gradual decrease in sustained firing seen for a single tone. Once the suppressive tone is removed, the typical onset and sustained behavior shown in Figure 2.22 repeats itself as the inhibitory second tone is removed and the initial excitatory tone takes over the response. This behavior arises from overlapping traveling waves on the BM. If the two tones are close enough in frequency such that their traveling waves overlap, then what results is a net attenuated traveling wave and the perceived suppressed behavior. Two-tone suppression is a mechanism by which AN fibers can provide contrast to a signal buried in noise.

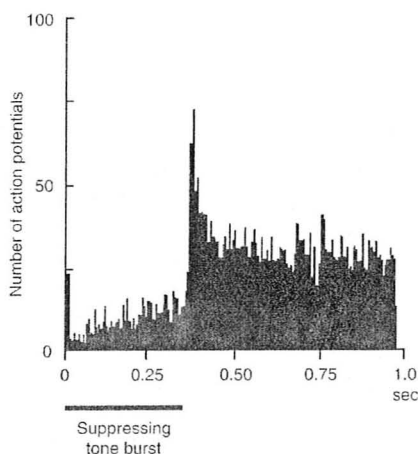


Figure 2.28: PSTH of an AN fiber undergoing two-tone suppression. AN fiber is receiving a continuous excitatory tone over the entire stimulus period. The time-course of the suppressive tone is shown by the black bar at the bottom of the Figure. Notice almost immediate drop in AN firing rate at the onset and the gradual increase in firing rate over the course of the suppressive stimulus. After the suppressive tone is removed, the AN fiber shows its typical onset behavior to the continuous excitatory tone. (Figure 4.13 reprinted from Pickles (2008))

2.2.3 The Central Auditory System

The auditory system is a symmetrical network of interconnected neurons in the brain that process auditory signals. There is an identical network of cells on each side of the brain that begins from the cochlea at each ear and ends at the auditory cortex. The two networks are also interconnected to allow for sound localization. The auditory system is divided into five main parts: (i) the cochlear nuclei, (ii) the superior olivary complex (SOC), (iii) the nuclei of the lateral lemniscus (NLL), (iv) the inferior colliculus (IC) and (v) the medial geniculate body (MGB) after which the network terminates at the auditory cortex. An illustration of the ascending pathways of the auditory system can be seen in Figure 2.29.

The system begins with AN fibers exiting the cochlea and projecting out to the cochlear nuclei. The works of this thesis focus on the responses of cells in the cochlear nuclei. A detailed description of the physiology and function of the cochlear nucleus can be found in section 2.2.4. After the cochlear nuclei, the auditory system is divided into two separate branches: (i) the binaural sound localization stream and (ii) the dorsal stream.

The binaural sound localization stream projects ventrally in the ventral acoustic stria to the superior olivary complex on both sides of the brain where information about the timing, intensity and vertical direction of sounds arriving at each ear are compared to localize the source of an auditory stimulus. The binaural sound localization stream has two divisions. The first division projects to the lateral superior olive (LSO) where the intensities of the stimuli at each ear are compared. Fibers that project to the contralateral LSO are received directly from the cochlear nuclei or indirectly via synaptic inputs from the medial nucleus of the trapezoid body (MNTB). The second division of the binaural sound localization stream projects to the medial superior olive (MSO) where interaural time differences are compared. The dorsal stream projects to the inferior colliculus (IC) on the other side of the auditory system and makes some terminals in the nuclei of the lateral lemniscus (NLL) on the way. Many of the projecting cells in the dorsal stream arise from octopus cells that terminate at the ventral nucleus of the lateral lemniscus (VNLL).

The superior olivary complex is composed of several subnuclei. The main components of the superior olivary complex are the LSO, the MSO and the MNTB. The LSO receives two major inputs: (i) direct, excitatory inputs from the AVCN (primarily spherical bushy cells) and (ii) inhibitory inputs provided by synaptic connections from cells in the MNTB which arise from globular bushy cells from the AVCN on the opposite side of the brain. Cells in the LSO fire in response to the difference in intensity of the sounds in each ear. An LSO cell fires at its maximum when an auditory stimulus is not present or extremely quiet at the opposing ear. As the intensity of the sound is increased in the opposite ear, the LSO cells firing rate decreases. When the sounds have equal intensity, the firing rate of an LSO cell approaches near zero levels

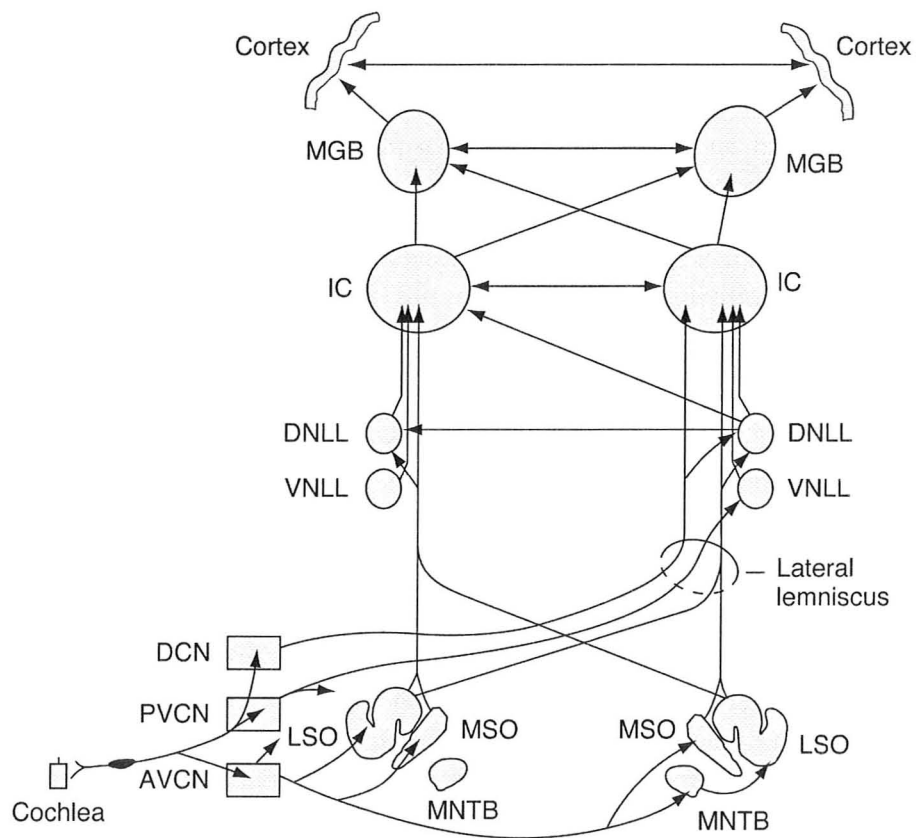


Figure 2.29: An illustration of the main ascending pathways of the brainstem are shown. AVCN, anteroventral cochlear nucleus; DCN, dorsal cochlear nucleus; DNLL, dorsal nucleus of the lateral lemniscus; IC, inferior colliculus; LSO, lateral superior olive; MGB, medial geniculate body; MNTB, medial nucleus of the trapezoid body; MSO, medial superior olive; PVCN, posteroventral cochlear nucleus; VNLL, ventral nucleus of the lateral lemniscus. (Figure 6.12 reprinted from Pickles (2008))

(Pickles, 2008). The MNTB, effectively, acts as a relay between spherical bushy cells in the AVCN on the opposite side of the brain and the LSO. The MSO receives direct innervation from spherical bushy cells of the AVCN on both sides of the brain. MSO cells act as coincidence detectors by comparing the interaural time difference between auditory signals in each ear. MSO cells are primarily low-frequency cells that use differences in the phase between incident signals at each ear to calculate the interaural time difference. As the delay is increased between signals at each ear, so does the firing rate of the MSO cell. A signal arriving at each ear at exactly the same time and in phase will cause the cell to fire at a level near zero. As the difference in phase is increased, so does the firing rate of the MSO neuron (Pickles, 2008). Spherical bushy cells are ideal inputs to the MSO because they are able to phase-lock to low-frequency signals with greater efficacy than individual AN fibers. MSO cells provide synaptic input to the dorsal nucleus of the lateral lemniscus (DNLL) as well as the IC.

Fibers extending from the SOC to the IC run through a tract known as the lateral lemniscus which is subdivided into two nuclei: (i) the ventral nucleus of the lateral lemniscus (VNLL) and (ii) the dorsal nucleus of the lateral lemniscus. Some fibers run directly through the lateral lemniscus to the IC and others enter after a synaptic terminal in either the VNLL or the DNLL. The VNLL receives inputs from contralateral (opposing) AVCN neurons as ipsilateral (same side) MNTB neurons. The VNLL is not involved in binaural sound localization and instead seems to be primarily involved in temporal responses and extracting harmonic relations between stimuli. Many VNLL have responses similar to AVCN octopus cells which have sharp onset behaviors. The DNLL, on the other hand, is involved in binaural sound localization and receives inputs from the ipsilateral MSO, the LSOs of both sides and the contralateral cochlear nucleus (Pickles, 2008). DNLL neurons are typically excited by contralateral stimuli and inhibited by ipsilateral stimuli. The DNLL serves to enhance the contrast between the responses to sound sources localized in the vertical plane (Pickles, 2008). Both the DNLL and VNLL provide significant inhibitory input to the IC.

The IC is the main hub for the auditory pathways from lower stages of the brain stem. The IC is the first stage in the auditory system where both the sound localization and sound identification streams of the auditory pathway converge. Here information from both streams is combined to form responses that are significantly more complex than those of previous stages of the auditory system. The IC is tonotopically organized and receives cells from several stages of the auditory system with identical frequencies in the same region. The variety of response types of IC cells is vast. Not only can cells be characterized by their responses to a wide variety of frequencies, but IC cells in the same tonotopic region have shown significant variation in responses indicating that there is further cell specialization orthogonal to the

frequency region (Pickles, 2008). IC cells have shown responses with multiple excitatory and inhibitory regions. IC cells have also shown that the sizes and locations of each region can be changed temporally due to inhibitory and excitatory interactions of surrounding neurons and input neurons. IC neurons project to the MGB. Some neurons project through the IC to the MGB without terminating in between.

The MGB is the final stage of the auditory system before the auditory cortex (AC). It both sends and receives significant inputs to the AC which indicates that they can be grouped together as a functional unit (Pickles, 2008). MGB cells have shown a large variety of responses, such as onset, offset, on-off or sustained excitation and inhibition. Many MGB neurons have extremely narrow tuning curves, even at high stimulus intensities. The tuning curves of MGB neurons have shown to be significantly narrower than those of AN fibers. This indicates that the MGB plays a role in maintaining frequency contrast regardless of stimulus intensity. Part of this sharp contrast is due to inhibitory inputs between adjacent MGB neurons.

The AC is the final and most complex part of the auditory system. Here all aspects of sound are processed, including localization. The responsiveness of the AC at any point in time is hypothesized to reflect the current behavioral state of the animal with the neuronal responses being modified so that a larger portion of the cortex is devoted to stimuli of particular significance (Pickles, 2008).

The various stages of the auditory system also project to non-auditory sections of the brain to induce responses such as the tightening of the middle ear muscle to protect against loud stimuli, the fast contraction of both facial and body muscles in response to a sudden acoustic stimulus and changes in orientation towards the source of an acoustic stimulus.

2.2.4 The Cochlear Nucleus

The cochlear nucleus (CN) of the brain is heavily involved in the process of sound localization in both the horizontal and vertical planes. Sounds are localized in the horizontal plane by comparing the difference in arrival time and sound pressure level at each ear. In the vertical plane, sounds are localized by detecting spectral notches in the signal that arise from the directionally dependant deflection of sound waves in the pinna. The neural circuitry in the CN is able to detect these features for sound localization. In addition to aiding in the sound localization process, CN cells also have certain properties which are involved in enhancing incoming auditory stimuli. Several of the cell types in the CN have inhibitory sidebands. These inhibitory sidebands can play an important role in enhancing spectral contrast in signals buried in noise by accentuating predominant frequencies in a signal and attenuating surrounding noisy regions. Fluctuations in amplitude modulated signals can also be emphasized by cells in the CN. Many cells in the VCN can phase-lock to tone stimulus with greater

precision than an individual AN fiber (Johnson, 1980). Changes in amplitude are then reflected in the overall firing rate of the cell. Other cells that receive a large number of AN inputs can reflect changes in the overall envelope of a signal by changes in their firing rates (Pickles, 2008).

The CN is divided into three sections: (i) the anteroventral cochlear nucleus (AVCN), (ii) the posteroventral cochlear nucleus (PVCN) and (iii) the dorsal cochlear nucleus. The orientation of these sections can be seen in Figure 2.30. AN fibers, of both types, enter the cochlear nucleus from the cochlea and branch to each of the three sections. The fibers are “tonotopically” arranged based on the CFs of the incident fibers (illustrated in Figure 2.30). Each region contains different cell types which perform different functions.

2.2.4.1 The Ventral Cochlear Nucleus (VCN)

The AVCN is composed of bushy cells. Bushy cells are divided into two cell types: (i) spherical and (ii) globular. Spherical bushy cells receive an average of three AN nerve fibers per cell and have synaptic terminals called end bulbs of Held (Ryuogo and Parks, 2003). Endbulbs of Held surround bushy cells and have many synaptic contacts (Figure 2.31). These synaptic contacts provide extremely reliable transmission of synaptic inputs with minimal synaptic delay. This is essential for the detection of precise timing information required in binaural sound localization (Pickles, 2008). The nature of these synaptic connections gives response properties similar to those of primary AN fibers. As such, spherical globular cells are said to have primary-like responses. The spherical globular cells project to the medial superior olivari (MSO) nuclei on both sides of the brain for coincidence detection of sounds. Globular bushy cells receive a larger number of auditory nerve inputs (between 4 to 40). They have smaller, modified end bulbs of Held as synaptic terminals. The larger number of AN inputs gives globular cells a higher probability of firing with the onset of a stimulus which gives what is known as a primary-like with notch response (Pickles, 2008). Globular bushy cells project along the pathway to the contralateral lateral superior olive (LSO), where the sound intensities of stimuli are compared.

The PVCN has four major types of cell: (i) globular bushy cells (as described above), (ii) octopus cells, (iii) T-stellate cells and (iv) D-stellate cells. Octopus cells are large cells with a complex structure (seen in Figure 2.32). They fire strongly at the onset of a stimulus, producing what is called an onset response. Octopus cells have an extremely low input resistance and short time constants which cause synaptic potentials to decay quickly. They receive a range of AN fiber inputs and only fire in response to several coincident AN fibers (Oertel *et al.*, 2000). They tend to respond best to broadband stimuli, such as clicks and are extremely useful in the process of coincidence detection. Octopus cells project to the contralateral ventral nucleus

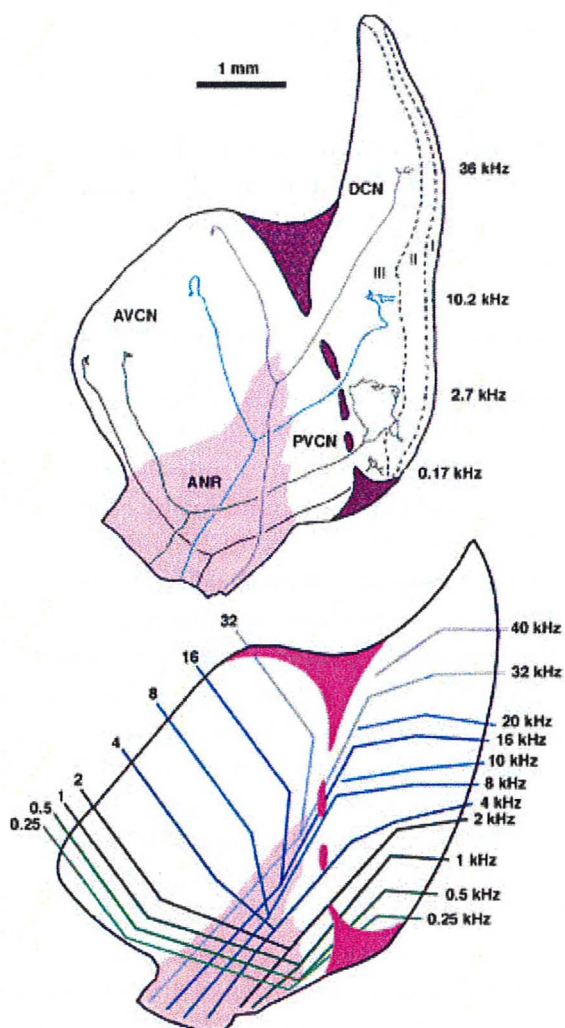


Figure 2.30: This figure shows the three regions of the cochlear nucleus (CN). Projection of incident auditory nerve fibers throughout the CN are shown. The tonotopic organization of the projecting fibers is also illustrated. (Fig. 9, reprinted from Ryuogo and Parks (2003))



Figure 2.31: Morphology of the endbulb of Held in mammals. Endbulbs of Held surround bushy cells and provide many parallel synaptic terminals for an incident AN fiber. (Fig. 3, reprinted from Ryuogo and Parks (2003))

of the lateral lemniscus (VNLL) and the superior paraolivary nucleus (SPN), which provide significant inhibition to the inferior colliculus (IC) (Cant and Benson, 2003). Of the two types of stellate cells, T-stellate cells account for the majority ($\sim 95\%$) of the population (Pickles, 2008). Stellate cells are given their name due to the shape of projection of their dendrites around the cell. T-stellate cells fire repetitively in response to a sustained stimulus at a rate unrelated to the frequency of the stimulus. This is called a sustained chopped response and is typified by a sharp initial peak followed by a series of declining peaks that eventually flatten out in height (Pickles, 2008). These cells have narrow excitatory bandwidths surrounded by wider inhibitory bands and can encode a narrow stimulus in a noisy background. T-stellate cells are also called T-multipolar or Type I multipolar cells and project to the DCN as well as the IC, the SPN and the dorsomedial periolivary nucleus (DMPO) (Cant and Benson, 2003). D-stellate cells produce an onset chopper response. This is similar to a sustained chopper response only it lacks the sustained firing over the length of the stimulus. This is due to a delayed inhibition of the cell from other neurons (Pickles, 2008). D-stellate cells receive AN inputs over a broad range of frequencies and are only responsive to broadband signals. They project to the DCN where they provide wideband inhibition. D-stellate cells provide direct inhibition to T-stellate cells to form the inhibitory sidebands that characterize their responses (Ferragamo *et al.*, 1998). D-stellate cells are also called Type II multipolar cells.

Neural response properties are often shown in the form of a post-stimulus time histogram (PSTH) which indicates the number of action potentials fired within a certain period of time in response to several repetitions of a stimulus. The PSTHs of the VCN cells described above are shown in Figure 2.33 to provide a visual representation of the response properties discussed.

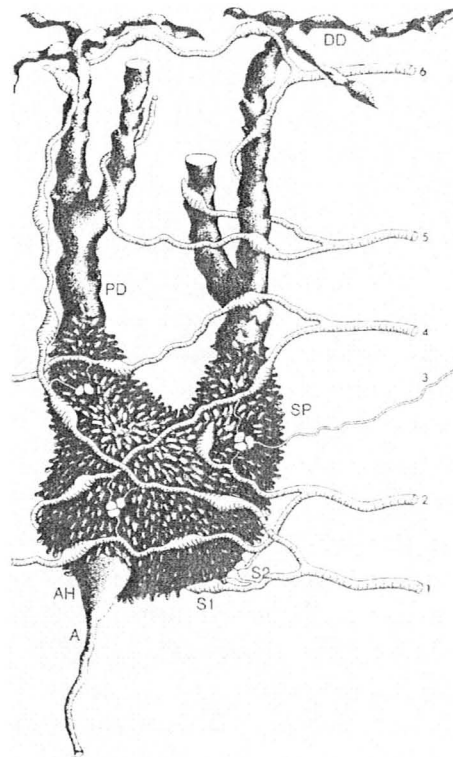


Figure 2.32: This figure shows the morphology of an octopus cell. (Figure 6.5, reprinted from Pickles (2008))

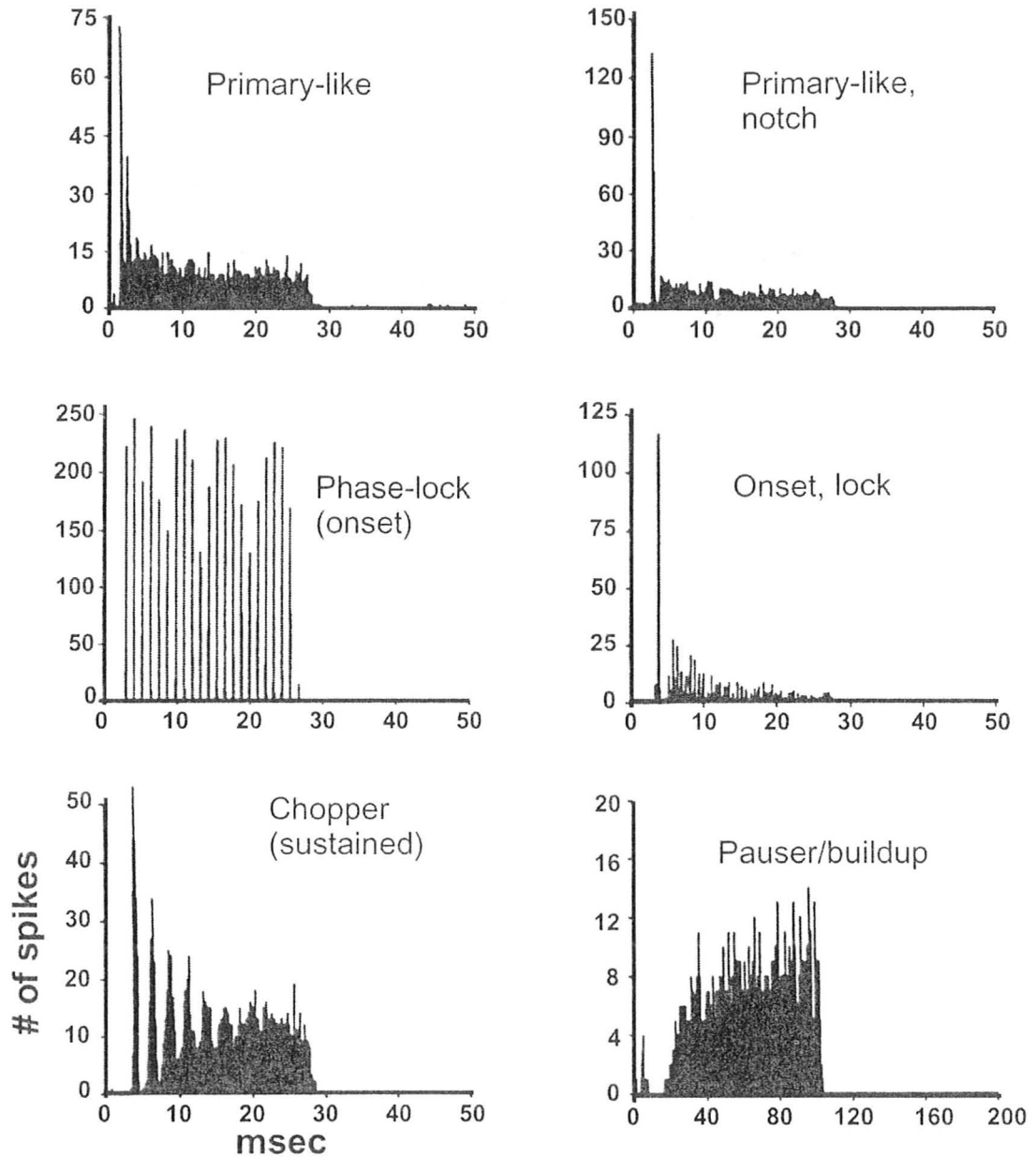


Figure 2.33: This figure shows the post-stimulus time histograms (PSTH) of the various responses found in the VCN. (Figure 3.1, reprinted from Oertel *et al.* (2002))

The ability of bushy cells to achieve a greater degree of synchrony with a low-frequency stimulus than AN fibers makes them ideal for coincidence detection of signals. The low membrane resistance and short time constants of bushy cells allows them to detect the time difference in two ears as small as $10\mu\text{s}$ (Pickles, 2008).

2.2.4.2 The Dorsal Cochlear Nucleus (DCN)

The DCN is made up of layers of cells characterized by the types of cells they contain. The DCN is divided into three regions arranged from outermost to innermost: (I) the superficial or molecular layer, (II) the pyramidal cell layer and (III) the deep layer (Young and Oertel, 2004). Each layer is tonotopically organized in parallel to its preceding layer. Figure 2.34 shows the different regions of the DCN, their relative position in the CN and the tonotopic organization.

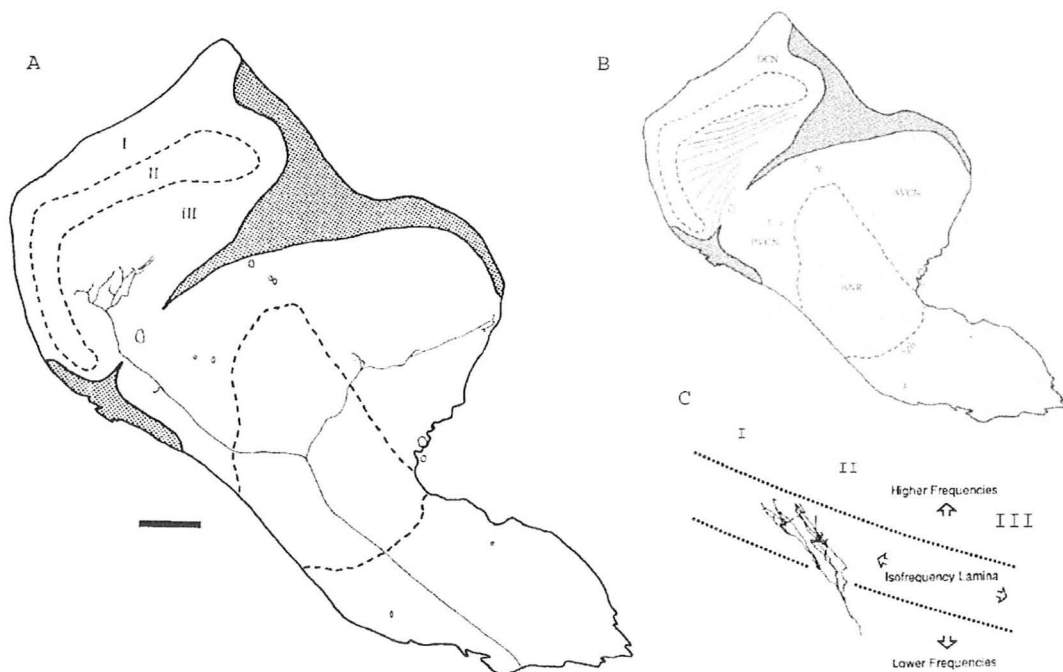


Figure 2.34: (A) shows the locations of the various regions of the DCN. (B) shows the location of all of the regions of the cochlear nucleus. (C) is an illustration of the tonotopic organization of the regions of the DCN. ((A) Figure 1, (B) figure 2 and (C) figure 3C reprinted from Ryugo and May (1993))

The superficial layer is comprised of granule cell axons and some of populations of small neurons. Granule cell axons are afferents to the DCN that provide inputs

orthogonally to AN fibers. The pyramidal cell layer is comprised primarily of pyramidal cells and cartwheel and granule cells. The deep layer contains the AN fibers, the other afferent to the DCN, as well as giant cells and vertical cells (Young and Oertel, 2004). Pyramidal cells and giant cells are the two forms of principal cells in the DCN. They are called principal cells because they integrate inputs from both types of afferents and are the primary output from the DCN.

Pyramidal (or fusiform) cells have dendrites extending to both the molecular and deep layers of the DCN. They form a band along the pyramidal cell region of the DCN receiving inputs from both AN fibers and the afferents in the molecular layer. They produce pauser and buildup responses to stimuli. Pauser responses have an onset spike, followed by a pause. Buildup responses show a slow buildup in spike activity in a response to a stimulus. The PSTHs of both of these responses can be seen in Figure 2.35. Fusiform cells project directly to the IC where they provide sound localization information (Cant and Benson, 2003).

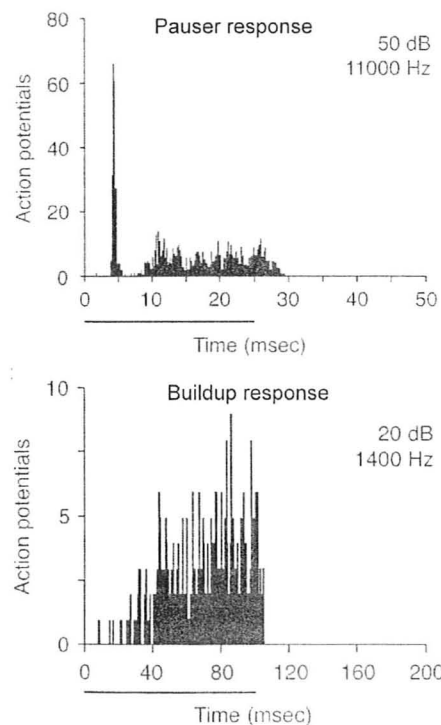


Figure 2.35: This figure shows the post-stimulus time histograms of the pauser and buildup responses seen in pyramidal cell in the DCN. (Figure 6.7 reprinted from Pickles (2008))

Cartwheel cells are inhibitory interneurons that receive inputs from granule cells.

Their dendrites project to the molecular layer of the DCN and they contact pyramidal, giant and other cartwheel cells. Intracellular recordings have shown some cartwheel cells respond strongly to sounds and others respond weakly. Animals with a lack of cartwheel cells have not shown a change in DCN cell responses and it is hypothesized that they provide nonauditory information to the DCN (Young and Oertel, 2004). Giant cells are large, multipolar cells located in the deep layer. Their dendrites are large and sparse and cross isofrequency slices. Giant cell axons project to pyramidal cells in the molecular layer as well as to the IC. Vertical cells are inhibitory interneurons in the deep layer. Their dendrites extend to the pyramidal cell layer and some project back to stellate cells in the VCN tonotopically to VCN cells with similar BFs. Vertical cells that project back to the VCN are called tuberculoventral cells. Granule cells receive major inputs from the parallel fibers and provide excitatory output to the DCN in the molecular layer. They provide excitation across isofrequency slices in the molecular layer.

The complex internal circuitry of the DCN is summarized in Figure 2.36. Here we can see the various layers of the DCN and the interconnections between all of the main DCN cell types. The types of interconnections are also noted with (+) indicating an excitatory connection and (-) and inhibitory connection. D-stellate cells from the PVCN have also been seen to project to the DCN to provide inhibitory input (Cant and Benson, 2003; Doucet and Ryugo, 1997). Experimental results have shown that these complex interactions can be used to control pyramidal cell plasticity (Oertel and Young, 2004).

DCN cell responses are typically described by what are called response maps (RM). RMs are intensity versus level matrices that indicate if a neuron is in an excitatory or inhibitory state. An excitatory state implies that the neuron is firing action potentials at a significantly higher rate than its average spontaneous rate in response to a stimulus. An inhibitory state is the exact opposite. DCN neurons, generally have a best frequency (BF) which is the frequency in which they are most easily excited. The main response types of cells found in the DCN can be seen in Figure 2.37. While the specific shapes of each response can vary from neuron to neuron, the inhibitory and excitatory regions that characterize each response are generally present.

The type IV response is typical of most DCN principal cells in cats. Type II responses are most commonly recorded from vertical cells in the DCN. Type III responses have been recorded from principal cells in the DCN. They differ from type II responses in that they have some spontaneous activity and respond equally well to both broadband noise as they do to pure tones (Oertel *et al.*, 2002). The main causes for the nonlinear responses of principal DCN cells can be explained, chiefly, by two inhibitory interactions: (i) narrowband inhibition provided by the vertical cells and (ii) wideband inhibition provided by the D-stellate cells in the VCN. Cross

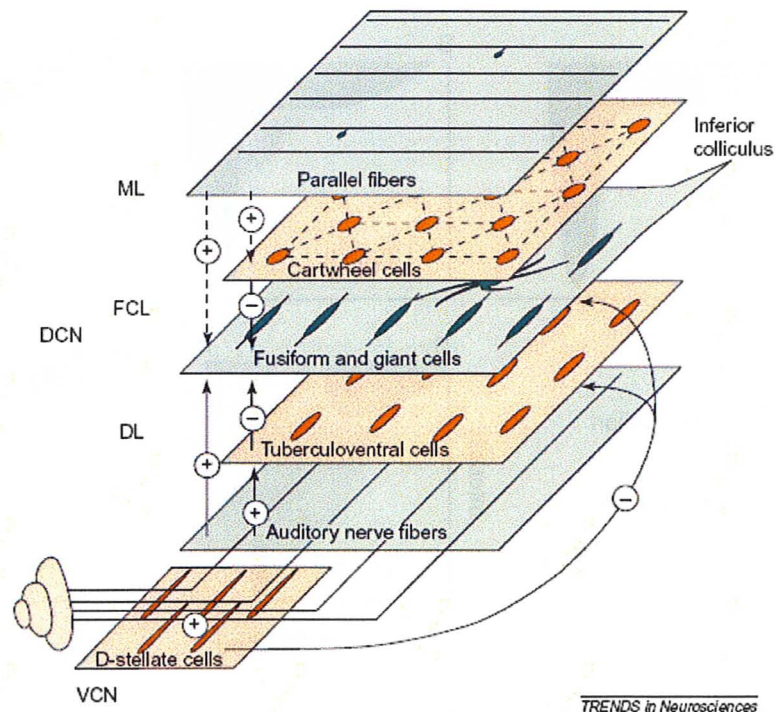


Figure 2.36: This figure shows the interconnections of all of the cell types in the DCN neural circuit. (+) indicates an excitatory connection and (-) indicates an inhibitory connection. ML is the molecular layer, FCL is pyramidal cell layer, DL is the deep layer, DCN is the dorsal cochlear nucleus and VCN is the ventral cochlear nucleus. (Figure 3 reprinted from Oertel and Young (2004))

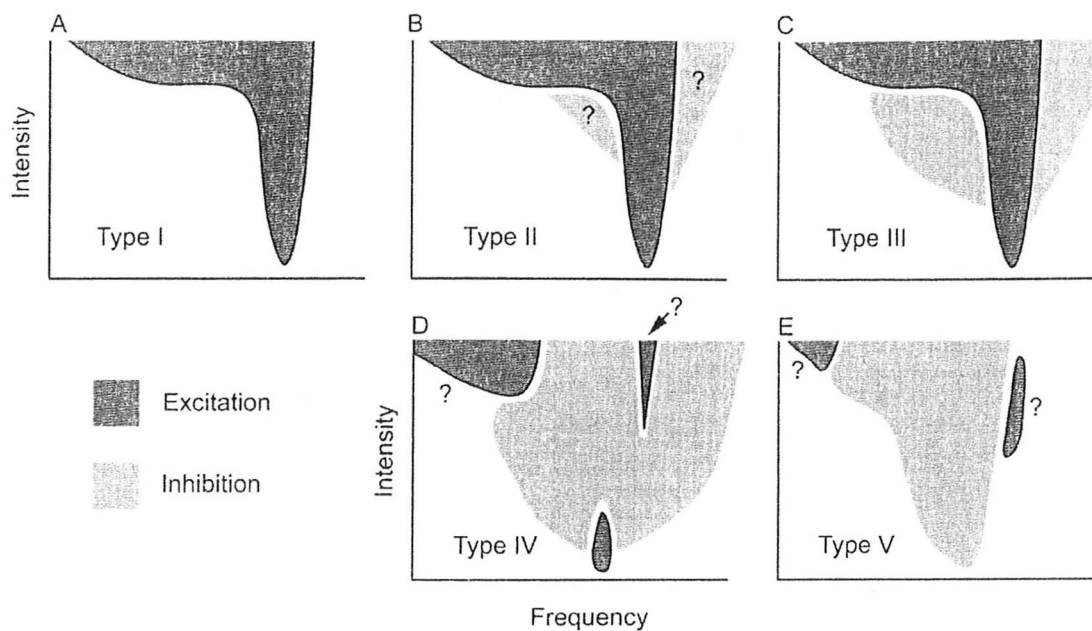


Figure 2.37: These figures shows the common response maps of each type of DCN cell response. Figures A-E are organized in increasing order of inhibition. Purely excitatory responses are typically found in the AVCN. Cells with greater amounts of inhibition (D-E) are predominantly found in the DCN. A question mark deliniates a feature that is not necessarily present in all cells of that type. (Figure 6.9 reprinted from Pickles (2008))

correlation experiments have shown a decrease in probability of discharge in type IV neurons following a discharge in a type II neurons with similar BF indicating direct inhibition (Oertel *et al.*, 2002). The onset chopper responses of D-stellate cells have the exact characteristics to cause the sideband inhibition in type II cells as well as the inhibitory response to notch noise exhibited by type IV neurons. The interactions of the various cells are summarized in the DCN circuit in Figure 2.38 and form the basis of the computational models of the DCN that will be used in this study. The GABAergic neuron, cartwheel neuron and granule cell inputs shown account for the additional internal circuitry discussed earlier.

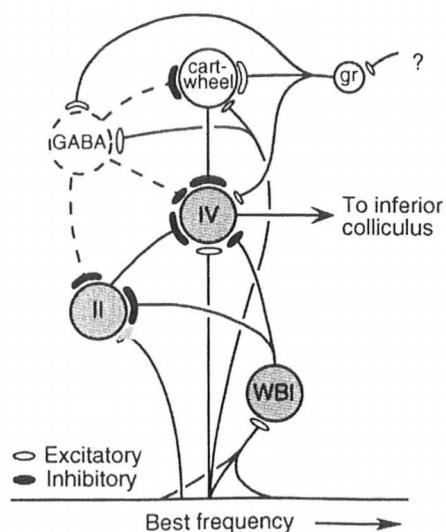


Figure 2.38: This figure shows a schematic for a DCN principal cell. All excitatory and inhibitory connections are shown as per the legend. IV, is a type-IV DCN cell; II, is a type II cell; WBI, represents wideband inhibition; GABA, represents a GABAergic neuron; gr, is a granule cell. (Figure 5.11 reprinted from Oertel *et al.* (2002))

Our earlier discussion of the outer and middle ear revealed that the pinna introduces spectral notches in an incident signal dependant on the location of the source in the vertical plane. Behavioral studies with cats have confirmed the location of the first spectral notch in a broadband signal arriving at the eardrum as being a key feature used by cats to localize sounds in the vertical plane (Oertel *et al.*, 2002). Recent studies have shown that type IV units in the DCN are highly responsive to the rising edges of spectral notches in a signal, confirming the involvement of the DCN as a key part of sound localization in the vertical plane (Reiss and Young, 2005).

Chapter 3

The Effects of Hearing Loss on Modeled Neurons in the DCN

This chapter outlines the computational studies undertaken to explore the effects of hearing loss in the auditory periphery on modeled DCN neurons. Results are compared to a physiological study performed by Ma and Young (2006) in order to determine if changes in DCN cell reponse properties arise from changes in the auditory periphery or plastic changes in the brainstem. The chapter begins with descriptions of the Carney (1993) and Zilany and Bruce (2007) models of the auditory periphery followed by a description of the Zheng and Voigt (2006) model of primary neurons in the DCN. A description of the implementation of the Zheng and Voigt (2006) model used in these works as well as a discussion of some of the difficulties faced follows. DCN neurons modeled using both the Carney (1993) and Zilany and Bruce (2007) models as input are compared and the sources of discrepancies found. A set of Zheng and Voigt (2006) model parameters capable of producing physiological responses using Zilany and Bruce (2007) model AN inputs is presented. Hearing impairment in the auditory periphery is then modeled using the Zilany and Bruce (2007) model and the effect on simulated DCN cells is shown and compared to physiological results.

3.1 Models of the Auditory Periphery

Two separate models of the auditory periphery were used in the following works: the Carney model and the Zilany and Bruce model. The differences between the two will be discussed below.

3.1.1 The Carney Model

The Carney (1993) model of the auditory periphery was developed in an attempt to model the temporal and average-rate characteristics of AN fiber responses, as well as the change on those characteristics as a function of stimulus intensity. The model attempts to model the following main components of the auditory periphery: (i) the mechanical tuning of the basilar membrane, (ii) inner hair cell (IHC) transduction and (iii) the IHC-AN synapse (adaptation, stochastic spike generation and refractoriness).

Figure 3.1 shows a schematic of the Carney model (Carney, 1993). The first stage of the model is time-varying narrowband filter that is designed to reproduce the effects of the mechanical tuning of the basilar membrane. The filter implementation is that of a gammatone filter with a variable bandwidth. An example of a gammatone filter impulse response in both the time and frequency domain can be found in Zhang *et al.* (2001). The bandwidth is varied by means of a feedback loop to the filter. The first stage of the feedback loop is an asymmetrical compressive non-linearity. This non-linearity is designed to have no effect at low SPL levels, have an increasing effect from about 30 to 90 dB SPL and then saturate for high signal intensities similar to the effects of broadened tuning in AN fiber tuning curves. Following the asymmetrical compressive non-linearity is a low pass filter to introduce a delay to the effects of the compressive non-linearity. The feedback signal is then scaled and biased from volts to seconds and then used as a control signal for the gammatone filter to control its bandwidth. The next stage of the model is a traveling wave delay to model the measured latencies of AN fibers.

The IHC is the next stage of the Carney (1993) model and is modeled as a saturating non-linearity followed by two low pass filters. The non-linearity is a characteristic of the input/output relationships of measured IHCs. The low pass filters are there to model the electrical filtering of the IHC membrane. Following this stage, we reach the IHC-AN synapse portion of the model. The signal from the previous stage of the model is used to drive a time-varying Poisson process spike generator. The spike generator has a feedback loop that is used to model effects of refractoriness. Refractoriness was modeled as an absolute refractory period of 0.75ms follow by a gradual decay of the discharge-history effect which lasts for about 40-50ms.

The Carney (1993) model is able to reproduce the temporal and average-rate characteristics of AN fibers in cats with low frequency CFs in response to tonal and more complex auditory stimuli. For higher frequencies, however, the model loses its ability to accurately model AN fiber responses to acoustic stimuli. The model is also unable to model some of the non-linearities present in the responses of low-SR AN fibers. As well, the Carney model does not model frequency glides, two tone suppression, peak splitting and lacks the ability to model the effects of hair cell loss on the responses of AN fibers.

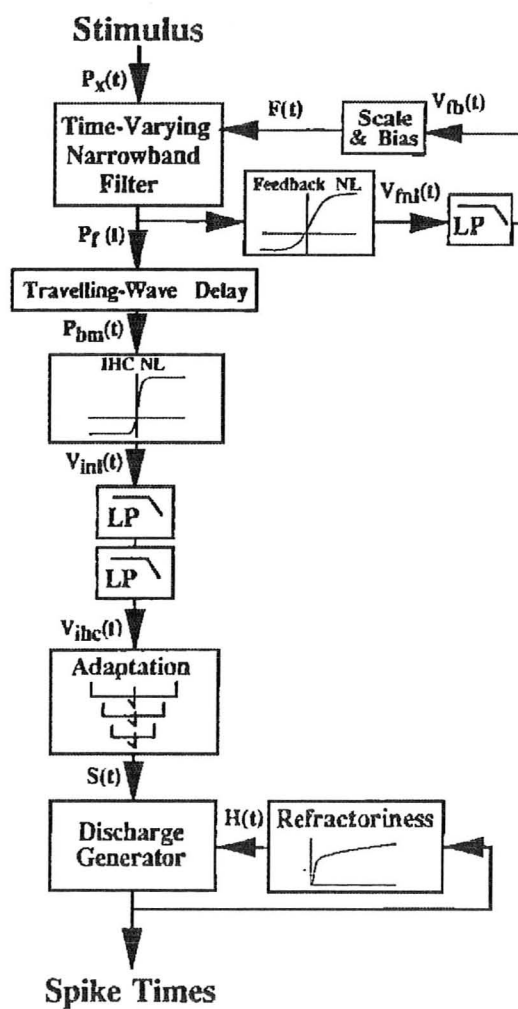


Figure 3.1: This figure shows a schematic for the Carney (1993) model of the auditory periphery. See text for details of elements of model. NL, is a non-linearity; LP, is a low-pass filter. (Figure 1 reprinted from Carney (1993))

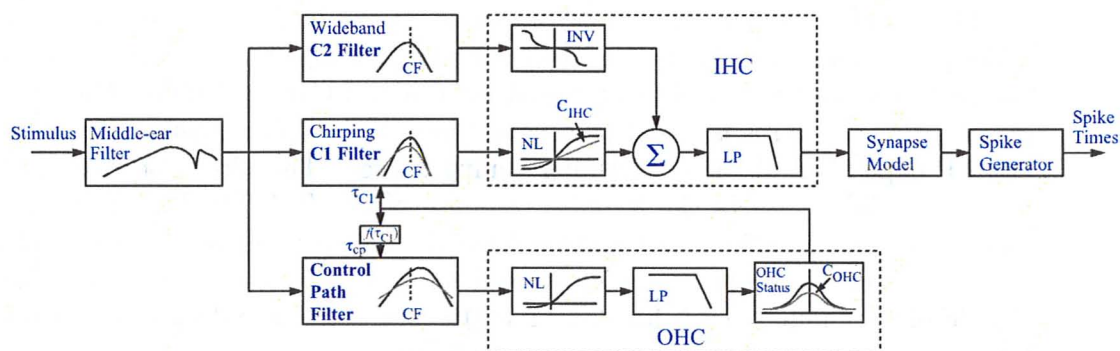


Figure 3.2: This figure shows a schematic of the Zilany and Bruce (2006) model of the auditory periphery. See text for details of elements of model. NL, is a non-linearity; LP, is a low-pass filter; CF, characteristic frequency; INV, inverting non-linearity. (Figure 1 reprinted from Zilany and Bruce (2006))

3.1.2 The Zilany-Bruce Model

The Zilany and Bruce (2006, 2007) model of the auditory periphery in cats is a robust computational model capable of modeling a broader range of physiological phenomena of AN fiber responses than the Carney (1993) model. This model is also able to recreate the effects of hearing impairment. A full schematic of the various stages of the model can be seen in Figure 3.2.

The first stage of the Zilany and Bruce (2007) model is a middle ear (ME) filter. This filter is a simplified version of the ME model proposed by Bruce *et al.* (2003) and is implemented as a second order system of three cascading digital filters. This filter reproduces the transfer function of the middle ear in cats, including the dip in pressure gain at 4 kHz arising from acoustic resonances in the bulla.

The model then separates into three parallel pathways: (i) the control path filter pathway, (ii) the C1 filter pathway and (iii) the C2 filter pathway. The control path filter pathway models the active processes in the cochlea and is divided into several stages. The first is a time-varying gammatone filter that allows for the reproduction of two-tone suppression effects. The filter has a higher center frequency and wider bandwidth than the C1 filter. The filter's center frequency corresponds to a shift of 1.2mm basal to the fiber CF along the BM. The control path filter then feeds into an OHC Boltzman non-linearity followed by an OHC low-pass filter with a cut-off frequency of 600 Hz. The output of the low-pass filter is passed to a nonlinear function that converts the output to time-varying coefficients in the C1 filter and control path filters. The net result of this pathway is to control the function of the C1 filter so that it behaves linearly at low and high stimulus intensities, while producing the

compressive and suppressive cochlear nonlinearities at moderate intensities.

The C1 filter models the tuning properties of the BM. It consists of two second-order poles and a first-order pole, their complex conjugates and a fifth-order zero on the real axis similar to a filter proposed by Tan and Carney (2003). The placement of the poles and zeros is based on several physiological phenomena. The first being the CF dependant shape of AN fiber tuning curves. The filter also reproduces the frequency glides seen in the impulse response of the BM. Finally, the compressive and suppressive nonlinearity resulting from the active processes in the cochlea. To reproduce these phenomena, the poles and zeros of the C1 filter are placed based on the CF of the simulated AN fiber and its Q10 values. Poles and zeros are then shifted based on the inputs provided by the control path.

The C2 filter is parallel to the C1 filter and is important in modeling responses at high intensities both for normal hearing and hearing impairment. The C2 filter is modeled as the broadest possible C1 filter (i.e. as the shape of C1 filter when the OHCs are completely impaired). The shape of the filter is based on physiological studies. The C2 filter's function is independent of OHC function and its shape is invariant over time.

The function of the IHC is modeled using the sum of the C1 and C2 filter pathways. The outputs of both the C1 and C2 filters are passed through separate transduction functions. The C1 transduction function is the same as that of Bruce *et al.* (2003) and is modeled as a logarithmic compressive function. The C2 transduction function's shape is designed to follow Kiang's two-factor cancellation hypothesis (Kiang, 1990). It is symmetrical and inverted with respect to the C1 transduction function. The slope of growth of the C2 transduction function is also double that of the C1 transduction function. The outputs of each transduction function are summed and then passed through a low-pass filter to give the IHC potential. The low-pass filter is a seventh-order filter with a cutoff frequency of 3800 Hz to match the decrease in pure-tone synchrony of fibers as their CFs increase.

After the IHC low-pass filter, the resulting signal is sent to the IHC-AN synapse model. The model is based on the work of Zhang *et al.* (2001) and models the spontaneous rate, adaptation properties and rate-level behavior of the simulated AN spike trains. Spike discharge times are produced by a renewal process driven by the synapse model that incorporates refractory effects. The implementation is similar to that of Zhang *et al.* (2001) and Bruce *et al.* (2003).

The effects of hearing impairment are modeled using the C_{IHC} and C_{OHC} scaling factors. These scaling factors take on values from 0 to 1 where 0 implies complete impairment and 1 represents healthy function. C_{OHC} is introduced in the control path output. As C_{OHC} is decreased, the C1 filter's bandwidth is increased (broadened tuning) and gain is decreased (elevated threshold) to recreate the effects of OHC impairment on AN fiber responses. When substantial IHC impairment occurs, the

responses of IHCs tend to be dominated by the C2 filter properties. To model these effects, the C_{IHC} scaling factor is introduced to attenuate the C1 filter signal as impairment is increased.

3.2 Zheng and Voigt DCN Model

The DCN model used in these works was developed by Zheng and Voigt (2006). The model consists of a network of five different cell types. A schematic for the model is shown in Figure 3.3. The five cell types are pyramidal cells (P-cells), type II cells (I2-cells), wideband inhibitor cells (W-cells), auditory nerve fiber inputs (AN-fibers) and non-specific afferents. The non-specific afferents in this model represent the inputs provided to DCN pyramidal cells by GABAergic neurons, cartwheel cells and granule cells (as discussed in 2.2.4.2). This network model is based on the anatomical model shown in Figure 2.38. The model is organized into 800 iso-frequency slices spaced 0.005 octaves apart with each cell in the same slice having an identical BF.

The Zheng and Voigt (2006) model is able to produce the various forms of pyramidal cell responses with simple changes to the connection parameters in the cell network. The connection parameters are: (i) number of inputs, (ii) connection strength and (iii) bandwidth of input cell BFs. The connection scheme of the DCN neural network is shown in Figure 3.4. Cell B is the cell being modeled and cell A is the input cell. Each connection between B and A is determined by the total number of A cells inputting to B ($N_{A \rightarrow B}$), the bandwidth of slices of A that provide input to B ($BW_{A \rightarrow B}$) and the offset of that input bandwidth ($C_{A \rightarrow B}$). For example, say we are modeling an I2-cell with a BF of 5kHz and we set $BW_{A \rightarrow B} = 2$ oct, $N_{A \rightarrow B} = 20$ and $C_{A \rightarrow B} = 1$ oct as the connection parameters for our AN inputs. That means that our I2 cell will have 20 AN inputs with CFs spread over a bandwidth of 2 octaves, centered around 10kHz (i.e., 20 AN inputs with CFs between 5kHz and 20kHz). Incident action potentials to cell B are modeled as step increases in variable conductance of $\sigma_{A \rightarrow B}$ followed by an exponential decay with time constant $\tau_{A \rightarrow B}$.

The neuron circuit model used of modeled DCN cells is based on the MacGregor (1987) neuromine. This model consists of a membrane capacitance, leakage conductance, a potassium channel branch and branches for each excitatory/inhibitory connection. The circuit model can be seen in Figure 3.5.

The following set of equations describe the MacGregor (1987) neuromine:

$$\tau_m \frac{dV_m}{dt} = -V_m - g_K(V_m - E_K) - g_{\text{ex}}(V_m - E_{\text{ex}}) - g_{\text{in}}(V_m - E_{\text{in}}) \quad (3.1)$$

$$\tau_K \frac{dg_K}{dt} = -g_K + b_K S \quad (3.2)$$

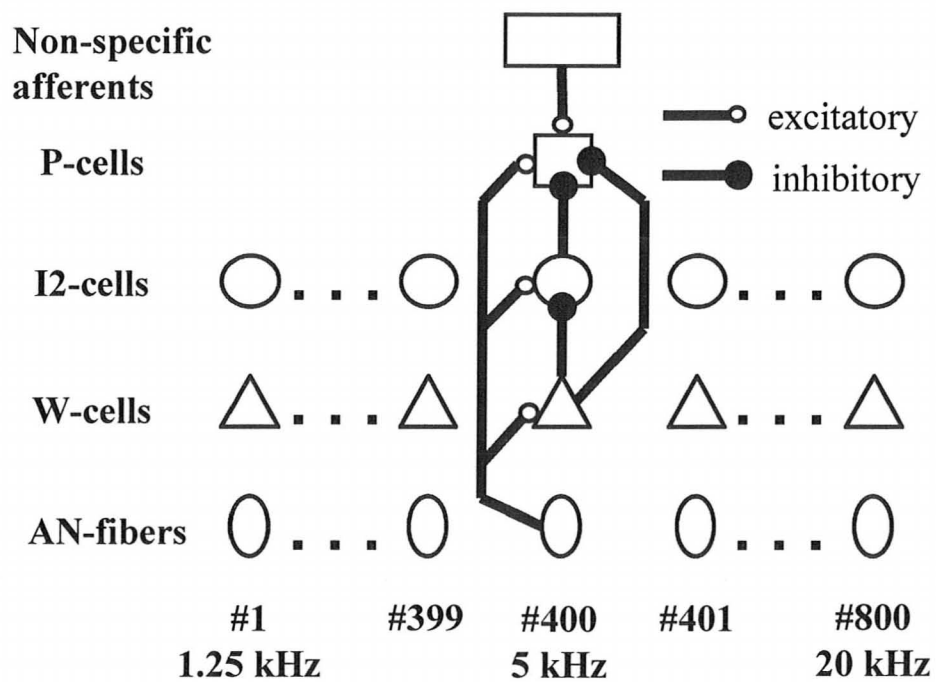


Figure 3.3: This figure shows a schematic for a patch of the Zheng and Voigt (2006) DCN principal cell model. All excitatory and inhibitory connections in a single frequency slice are shown. P-cells represent DCN pyramidal cells; I2-cells represent type II units; W-cells are wideband inhibitors; AN-fibers are the auditory nerve inputs. (Figure 1.a reprinted from Zheng and Voigt (2006))

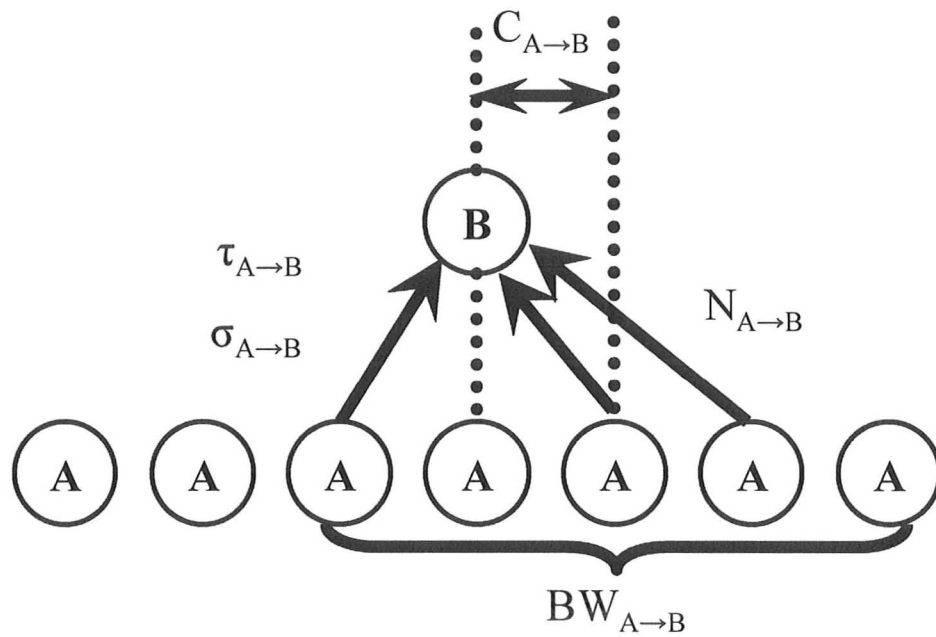


Figure 3.4: This figure shows the connection scheme between cell types in the Zheng and Voigt (2006) DCN model. Cell B represents the cell being modeled and cell A represents the input cell. The connections parameters are all shown. $\sigma_{A \rightarrow B}$ and $\tau_{A \rightarrow B}$ are the step conductance increase and decay time constant in response to spike inputs from input cells A. $BW_{A \rightarrow B}$ is the bandwidth of input A cells that input into cell B. $C_{A \rightarrow B}$ is the offset of the input BW from the B cell BF. $N_{A \rightarrow B}$ represents the number of A cells that connect to cell B. (Figure 1.b reprinted from Zheng and Voigt (2006))

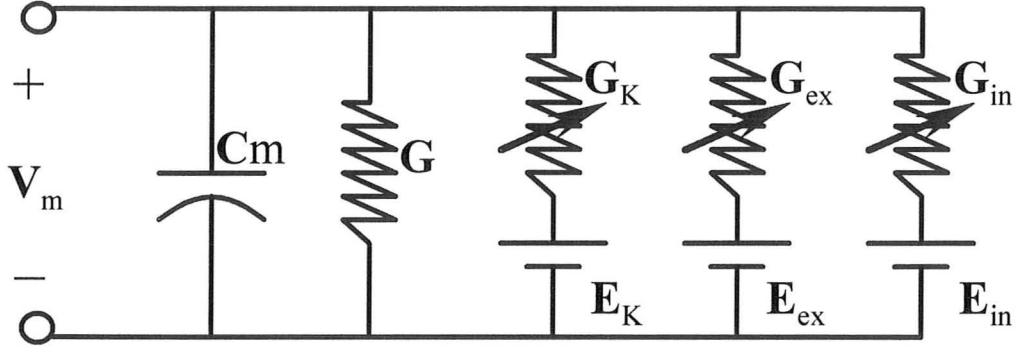


Figure 3.5: This figure shows the circuit model used to model individual neurons in the Zheng and Voigt (2006) model. V_m is the transmembrane potential, C_m is the membrane capacitance and G the membrane leakage conductance. E_K is the potassium channel reversal potential and G_K the potassium channel variable conductance. E_{ex} is the reversal potential and G_{ex} the variable conductance for an excitatory synaptic input. E_{in} is the reversal potential and G_{in} the variable conductance for an inhibitory synaptic input. (Figure 1.c reprinted from Zheng and Voigt (2006))

Table 3.1: DCN model intrinsic parameters

Population	τ_m (ms)	θ (mV)	b_K	τ_K (ms)	E_K (mV)	E_{ex} (mV)	E_{in} (mV)
W-cells	5.0	4.0	2.00	1.0	-10	+70	-10
I2-cells	6.0	14.5	1.75	1.0	-10	+70	-10
P-cells	10.0	7.5	2.00	1.0	-10	+70	-10

where $g_K = G_K/G$, $g_{ex} = G_{ex}/G$ and $g_{in} = G_{in}/G$. When V_m crosses the action potential threshold, the time of the action potential is noted and S is set to one to trigger the step increase in the K^+ channel conductance. S is zero otherwise.

Synaptic inputs to target cell B from source cells A are modeled using the following expression

$$\tau_{A \rightarrow B} \frac{dg_{A \rightarrow B}}{dt} = -g_{A \rightarrow B} + \sigma_{A \rightarrow B} \sum_{i=1}^{N_{A \rightarrow B}} S_{A_i} \quad (3.3)$$

where S_A are the input spikes at time t .

Table 3.1 shows the individual cell parameters for all of the different modeled cells in the Zheng and Voigt (2006) model. The rest of the model parameters were changed depending on the type of pyramidal cell response we were trying to simulate.

Non-specific afferents were modeled as a Poisson process with a firing rate set to 120 spikes/s.

3.2.1 Model Implementation

An initial attempt at coding the Zheng and Voigt (2006) model in MATLAB using an integrate-and-fire type implementation and Euler's method of numerical integration proved unsuccessful. The presence of step increases and decreases in the membrane conductance resulted in oscillatory behavior as a result of sharp changes in dV/dt that would drive the membrane potential to infinity. The size of the step increases proposed by Zheng and Voigt (2006) combined with the relatively long simulation time step of 0.1 ms were the root cause of the instabilities. While smaller simulation steps could counteract these behaviors, the resulting drastic increase in computational time for simulating a network of this complexity proved prohibitive.

The implementation of the Zheng and Voigt (2006) model used in these works used a significantly different method to model the DCN neural network. Direct numerical integration was not used for calculating the transmembrane potential or any variable conductances. Instead each variable parameter was treated as a constantly exponentially decaying function. At each simulation time step the change in variable conductance was calculated using the following expression

$$g_x(t) = g_x(t-1) \exp\left(\frac{-\Delta t}{\tau_x}\right) + \sigma_{A \rightarrow B} N_x(t) (1 - \exp\left(\frac{-\Delta t}{\tau_x}\right)) \quad (3.4)$$

where Δt is the simulation step size, $g_x(t)$ the variable conductance as simulation time t , $\sigma_{A \rightarrow B}$ the synaptic connection strength (as described above) and N_x the total number of synaptic inputs at time t . The transmembrane potential was calculated using the following expressions:

$$V_m(t) = V_m(t-1) \exp\left(-\frac{g_{\text{tot}}(t)\Delta t}{\tau_m}\right) + E_\infty (1 - \exp\left(-\frac{g_{\text{tot}}(t)\Delta t}{\tau_m}\right)) \quad (3.5)$$

$$E_\infty = \frac{-E_K g_K(t) + E_{ex} g_{ex}(t) + E_{in} g_{in}(t)}{g_{\text{tot}}} \quad (3.6)$$

$$g_{\text{tot}} = 1 + g_K(t) + g_{ex}(t) + g_{in}(t) \quad (3.7)$$

Effectively, each variable continues to decay over the length of the simulation until a synaptic input introduces a step increase, after which, the parameter continues to decay. This implementation has several advantages: (i) minimal computational resources are required and (ii) instability issues are prevented by avoiding direct

numerical integration.

The Zheng and Voigt (2006) DCN model implementation used in these works was coded in a combination of FORTRAN and C by members of Herbert F. Voigt's research group at Boston University. All computations and modeling were performed in FORTRAN and C was used for its I/O functionalities (loading and storing data). These programming languages were used due to the advantages they provide to computational time. All DCN simulations were carried out on an IBM pSeries 655, 48-processor system with 6 nodes located at Boston University. Each node consists of eight Power4 processors running at 1.1 GHz and sharing 16 GB of memory.

AN fiber spike train inputs to the DCN model were simulated and stored once using both the Carney and Zilany and Bruce models of the auditory periphery. All subsequent DCN simulations would load and use these previously generated spike trains. Spike trains were simulated for a set of 800 AN fibers with CFs spaced 0.005 octaves apart and centered around the DCN model center frequency of 5 kHz. Spontaneous rates were assigned to the AN fibers randomly using a physiological statistical distribution (Davis and Voigt, 1996). The distribution, seen in Equation 3.8, uses a uniformly generated random variable (*prob*) as input to a piece-wise function that assigns an SR (R_{SP}). Each fiber was presented with a single repetition of a 1-second stimulus consisting of an onset delay of 10 ms, followed by a 200 ms tone and then silence for the remainder of the one second period. The tone was given a 5-ms sinusoidal ramp at both the onset and at the end of the waveform. AN fibers spike trains were generated for tone stimuli with intensities ranging from 0 to 90 dB SPL (in 2 dB SPL steps) and stimulus frequencies within 1.5 octaves above and below the 5 kHz (in 0.1 octave steps) to generate DCN cell response maps. AN spike trains were simulated with a sampling frequency of 100 kHz.

$$R_{SP}(\text{prob}) = \begin{cases} 3.66 \cdot \text{prob}, & \text{prob} < 0.14, \\ 0.12 \cdot 10^{(5.06 \cdot \text{prob})}, & 0.14 \leq \text{prob} \leq 0.38, \\ -222.0 + 611.0 \cdot \text{prob}, & 0.38 < \text{prob} < 0.4, \\ 0.0066 \cdot \sinh 29.8 \cdot (\text{prob} - 0.697) \\ + 63.1 \cdot \text{prob} + 20.35 & \text{prob} \geq 0.4. \end{cases}, \quad (3.8)$$

Spike train inputs as well as DCN model outputs were stored to data files using the *stdio.h* functionality of C. As such, rigorous formatting of generated AN input data was required. A separate data file was created for each stimulus configuration that contained the spike trains for all 800 AN fibers simulated using that stimulus. Each individual spike train was converted into a vector of inter-spike intervals (ISIs) in order to minimize storage space. Firstly, the total number of spikes arriving from the AN input is streamed to a binary data file using 4 unsigned bytes of numerical precision. Following that the ISI for each successive spike is streamed to the data

file using 2 unsigned bytes of numerical precision. In rare cases where the ISI is too long to be stored using 2 unsigned bytes of data, a hexadecimal value of 0xFFFF is streamed to the data file followed by the ISI stored using 4 unsigned bytes. Once the entire ISI vector has been streamed to the data file using the C *write()* or the MATLAB *fwrite()* command, the procedure is repeated again for the next AN fiber. Spike trains are stored in the data files in order of increasing CFs. The same process was used to process the input data for use in the DCN model. DCN model data was stored to a data file using a similar process. Instead of generating a separate output file for each stimulus configuration, one data file containing the modeled DCN P-cell spike trains from all input configurations was stored and later used to generate response maps.

AN fibers simulated using the Carney model were simulated on the same computational system used for simulating DCN cell responses. The AN data simulated using the Zilany and Bruce model was generated on the Grid computational network at McMaster University. Initial attempts to integrate Zilany and Bruce AN data with the Zheng and Voigt DCN model provided difficult due to incompatible binary data formats between the two computational systems. The IBM pSeries 655 uses an IEEE standard big endian format of storing data. By forcing the *PRECISION* variable of the *fwrite()* command in MATLAB to “ieee-be”, all simulated Zilany and Bruce AN inputs were compatible with the DCN model code, regardless of computational system used.

Response maps (RMs) were generated from the simulated DCN cell spike data using the statistical method outlined by Davis *et al.* (1995). The spontaneous rate of the simulated DCN cell was defined as the mean of the calculated firing rate of the last 160 ms of the silence following each stimulus over all stimulus configurations. Driven firing rates were computed using the last 160 ms of each presented tone burst. RMs were viewed as a matrix where each point represents a particular stimulus configuration and is assigned a value of 1, -1 or 0 to represent an excitatory, inhibitory or spontaneous state, respectively. All raw driven and spontaneous rate were filtered using a 3x3 spatial low-pass filter with coefficients of 1/9 before any processing. The *filter2* function in MATLAB was used to accomplish this. An asymmetric statistical criterion was used to determine whether or not the DCN cell was in an excitatory, spontaneous, or inhibitory state. If the driven rate for a particular stimulus was greater than $2 \cdot \sigma_{SR}$, where σ_{SR} is the standard deviation of the DCN cell SR, then the cell was said to be in an excitatory state. If driven rate was more than $0.5 \cdot \sigma_{SR}$ below the SR, the DCN cell was said to be in an inhibitory state. Otherwise, the cell was said to be in a spontaneous state. Once each region was classified, the data was spatially filtered using a median filter function (*medfilt2*) in MATLAB. Prior to applying the spatial median filter, the entire 0 dB column of the RM matrix was set to 0. Without this, the spatial filter averaging would cause the computed response

map to spread out to the edges of our matrix.

3.3 Healthy Modeled Neurons in the DCN

Prior to examining the effects of hearing loss on modeled DCN neurons, it is important to ensure that healthy modeled neurons are producing the correct response properties. Once the Zheng and Voigt (2006) DCN model had been integrated with the Zilany and Bruce (2007) model of the auditory periphery, it was found that modeled DCN cell responses had changed significantly. The effects an improved model of the auditory periphery had on modeled DCN neuron responses is shown. An analysis of the differences between the Carney (1993) and Zilany and Bruce (2007) model response properties was performed. Following this analysis, a framework for accounting for these differences is presented. Finally, sample healthy modeled DCN cells showing correct response properties using Zilany and Bruce (2007) AN inputs are presented.

3.3.1 Comparison of the response maps of simulated DCN units using the two different AN fiber models

Figure 4 of Zheng & Voigt outlined a set of parameter settings for their DCN model that were able to reproduce the canonical response properties of type III, type IV and type IV-t cells of the DCN. Using the same parameter values, we simulated DCN P-cells using AN fiber inputs produced from both the Carney and Zilany & Bruce models. The results can be seen in Fig. 3.6.

It is evident that the responses produced by using each of the AN models as input differ greatly. The responses obtained using the Zilany & Bruce model show a much greater level of excitation. The response maps tend to not only produce much broader regions of excitation but tend to be more excitable at significantly lower stimulus intensities. We also notice substantially smaller regions of inhibition, especially at higher stimulus levels in our type IV and type IV-t cells. The type-III units simulated using the Zilany & Bruce model completely lack a low-frequency region of inhibition.

3.3.2 Comparison of the response properties of the AN fiber inputs produced by each AN model

The results shown in Fig. 3.6 make it extremely clear that the change in AN model inputs significantly alters the response properties of DCN P-cells. Figure 3.7 compares the response properties of AN fibers with low, medium and high CFs. Carney model fibers can be seen on the left and Zilany and Bruce fibers can be seen on the right.

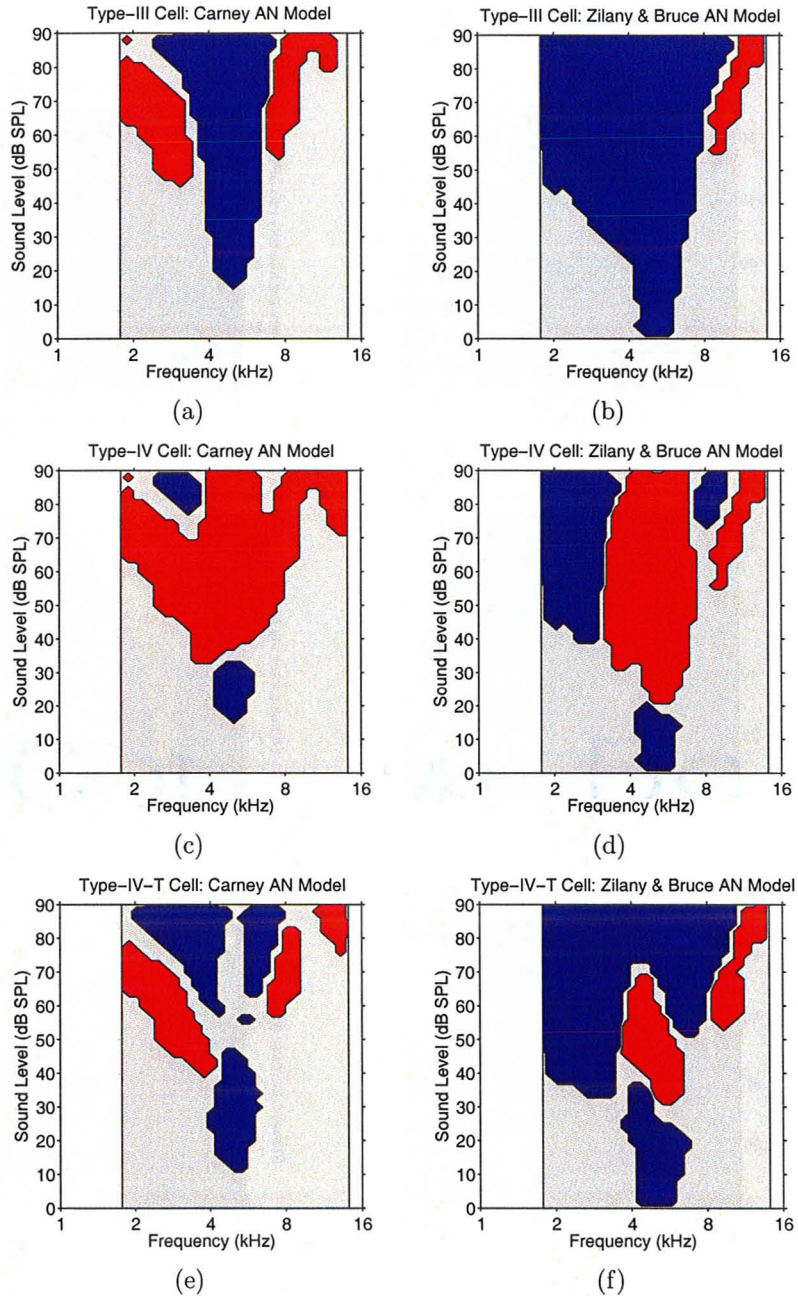


Figure 3.6: Response maps of typical P-cell types are shown. Type III, type IV and type IV-T cells simulated using the Carney AN model are shown in subfigures (a), (c) and (e), respectively. Type III, type IV and type IV-T cells simulated using the Zilany & Bruce AN model are shown in subfigures (b), (d) and (f), respectively. Blue regions represent excitation and red regions represent inhibition.

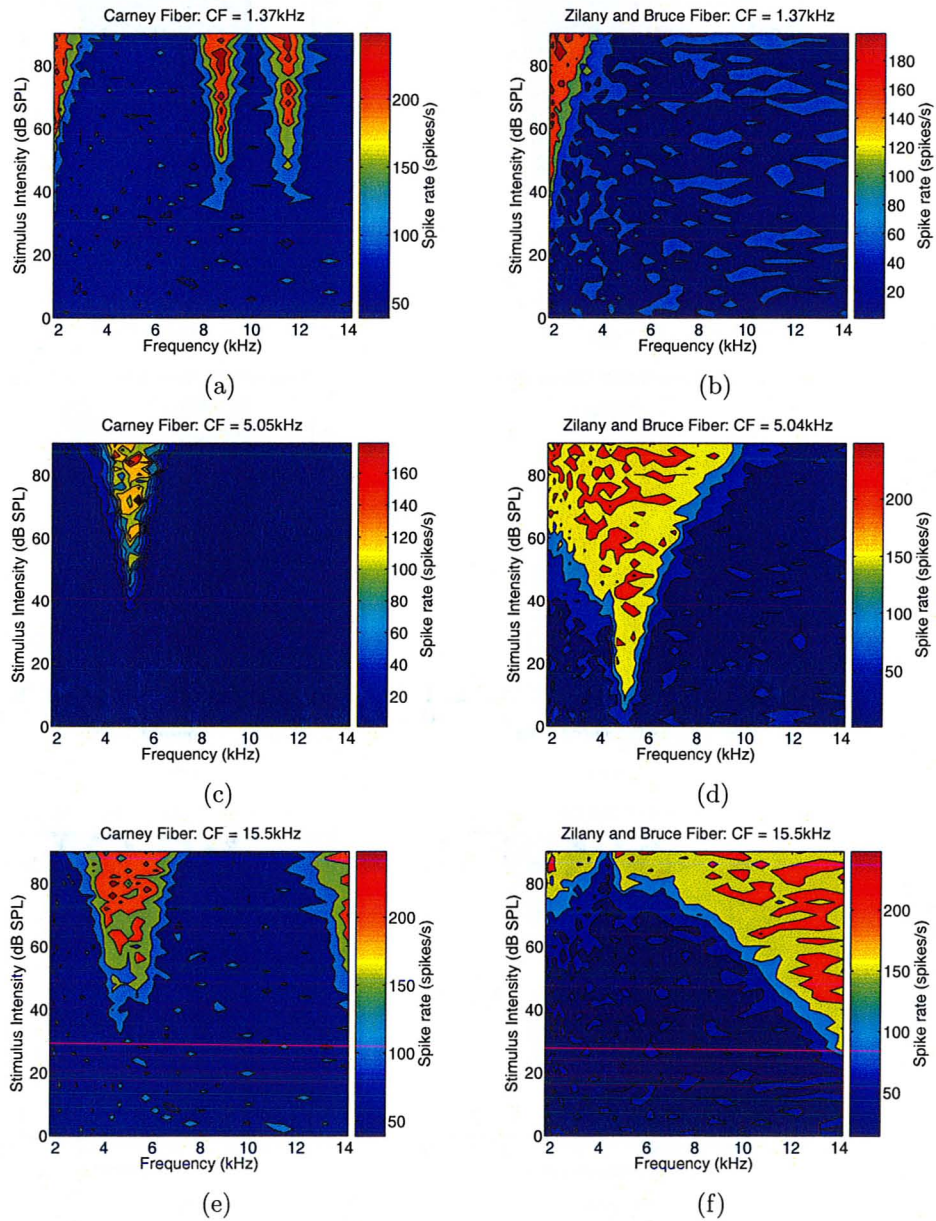


Figure 3.7: Response maps of AN fibers. Carney AN model are shown in subfigures (a), (c) and (e), respectively. Zilany & Bruce AN model are shown in subfigures (b), (d) and (f), respectively.

Figure 3.7 shows significant differences between the two models. Common across all AN fibers we see a significantly wider tuning at higher intensities for all fibers produced using the Zilany & Bruce model. We also see much lower excitation thresholds in Zilany & Bruce model fibers.

The most striking difference between the two models is the presence of the distortions in the Carney model. We see significant levels of excitation at higher frequencies for the low-CF fiber and vice versa for the high-CF fiber.

3.3.3 Effects of DCN connection parameter changes on DCN cell response properties

While statistically based response maps are excellent tools for examining the response properties of excitable cells, we will use plots of excitation rates to examine the effects of parameter changes on the response properties of DCN cells. These types of plots provide a more detailed description of the behavior of excitable cells and provide better direction in determining a parameter change strategy.

Figure 3.8 shows contour plots of the discharge rates of type-II DCN cells using both the Carney and Zilany and Bruce AN fiber models as input. We can see that the type-II cells simulated using the Zilany & Bruce AN fiber model have much lower thresholds of excitation and much broader regions of excitation at higher frequencies. This is quite similar to the observations of the differences between the two AN fiber response properties. We also notice that the Zilany & Bruce type-II cells show slightly less excitation at higher intensities. This observation accounts for the observed higher levels of excitation at higher intensities in P-cells simulated using Zilany & Bruce model AN fibers. Type-II cells provide significant inhibitory input to P-cells and if their responses are weaker at higher stimulus intensities, they will provide less inhibition to the P-cells at those intensities.

Figure 3.9 shows the W-cell responses arising from each of the AN models. We can see that the W-cell produced using the Carney model has an extra region of excitation in the 12–14-kHz range. This region of excitation is well beyond the W-cell input AN fiber bandwidth of 2.0 octaves. This region likely stems from the high frequency distortions in the Carney low-CF fibers shown in Fig. 3.7. The second thing we notice is that the Zilany & Bruce W-cell has a slightly wider response than the Carney W-cell and the presence of a notch at 4 kHz. This is the result of the 4-kHz notch in the middle-ear filter of the Zilany & Bruce model. All AN fibers have their responses to frequencies around 4 kHz significantly attenuated and as such cause a decrease in excitation. Away from 4kHz, however, we see that the Zilany & Bruce W-cells have higher levels of excitation than the Carney W-cells.

The results shown in Figs. 3.8 and 3.9 provide us with concrete goals for integrating the two models. We need to increase the levels of excitation at higher stimulus

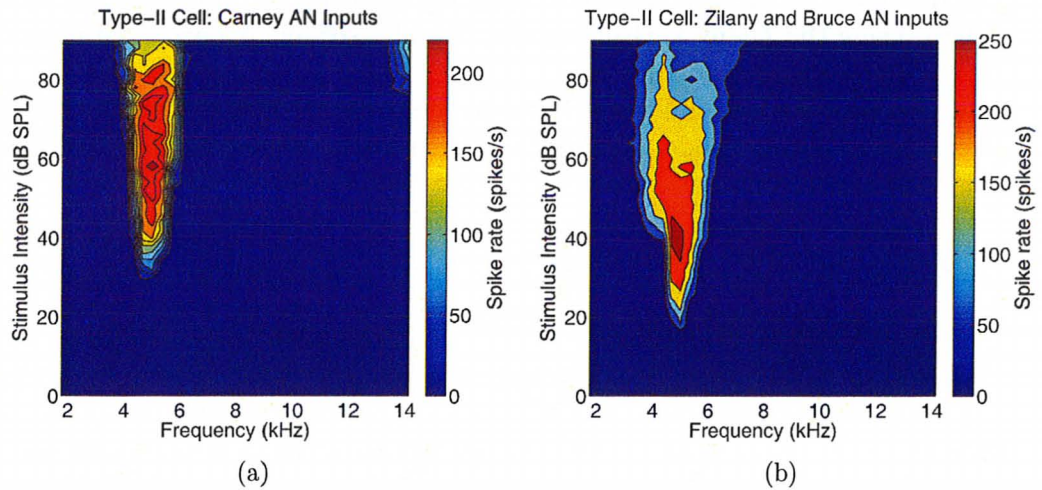


Figure 3.8: Type-II cell responses with identical DCN model parameters. The type-II cells simulated using the Carney and Zilany & Bruce AN model inputs can be seen in (a) and (b), respectively.

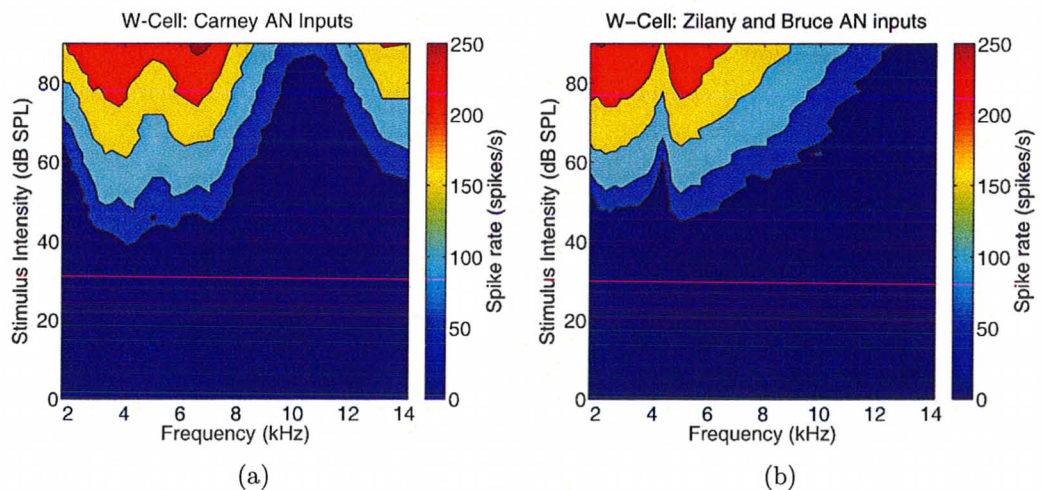


Figure 3.9: W-cell responses with identical DCN model parameters. The W-cells simulated using the Carney and Zilany & Bruce AN model inputs can be seen in (a) and (b), respectively.

intensities for our type-II cells and narrow their responses. Doing so will allow for increased inhibition of P-cells at higher intensities which would help to decrease the regions of excitation and begin to match the two outputs.

Figure 3.10 shows the effects of certain parameter changes on the responses of type-II cells. In an attempt to increase excitation in type-II cells we first explored decreasing the level of inhibition from input W-cells. The AN connection strength to the W-cells was decreased to 0.04 from 0.06 and the AN connection strength to the type-II cell was decreased to 0.45 from 0.55 in 3.10(a). These changes had the desired effects of slightly increased excitability at higher intensities and decreases in the excitation thresholds of the type-II cell.

In Fig. 3.10(b) we decreased the bandwidth of AN fiber inputs to the type-II cell to 0.3 from 0.4. This had the effect of increasing the overall excitation but widening the response of the type-II cell. This is likely the result of having greater overlap between the responses of AN fibers as they begin to get closer and closer.

Finally in Fig. 3.10(c) we increased the AN fiber connection strength to the type-II cell back to 0.55 and decreased the W-cell connection strength to the type-II cell to 1.3. Both of these parameters were changed individually and produced the same result, a widening of the response and increased levels of excitation. Figure 3.10(c) shows the effect of changing them both together which greatly enhances the behavior.

3.3.4 Ideal DCN Connection Parameters

In the previous section we showed and accounted for the changes in response properties of simulated DCN cells that occur when using Zilany and Bruce (2007) AN inputs. We also showed the effects that changing individual DCN model connection parameters had on simulated responses. Using the insight gained from those simulations, we were able to find a set of DCN model connection parameters that was able to reproduce physiological DCN principal cell responses to Zilany and Bruce (2007) model AN fiber inputs. The same simulation method originally used by Zheng and Voigt (2006) to determine the DCN model parameter set that generated the responses in Figure 3.6 was repeated to determine the new parameter set. In essence, all connection parameters other than $\sigma_{AN \rightarrow P}$ and $\sigma_{I2 \rightarrow P}$ are treated as constants. A 10 by 10 matrix of DCN cell RMs was simulated with $\sigma_{AN \rightarrow P}$ varying along the column and $\sigma_{I2 \rightarrow P}$ varying along the row of the matrix. The RMs in each matrix were then examined to find the $\sigma_{AN \rightarrow P}$ and $\sigma_{I2 \rightarrow P}$ combinations that resulted in a response that most closely resembled those of physiology. New 10 by 10 matrices were then simulated centered around those points only with parameters varying over a much smaller range. This process was repeated until the RMs ceased varying significantly around the center point of the generated matrix. After that, the rest connection parameters were varied to compensate for any remaining discrepancies using the insight from

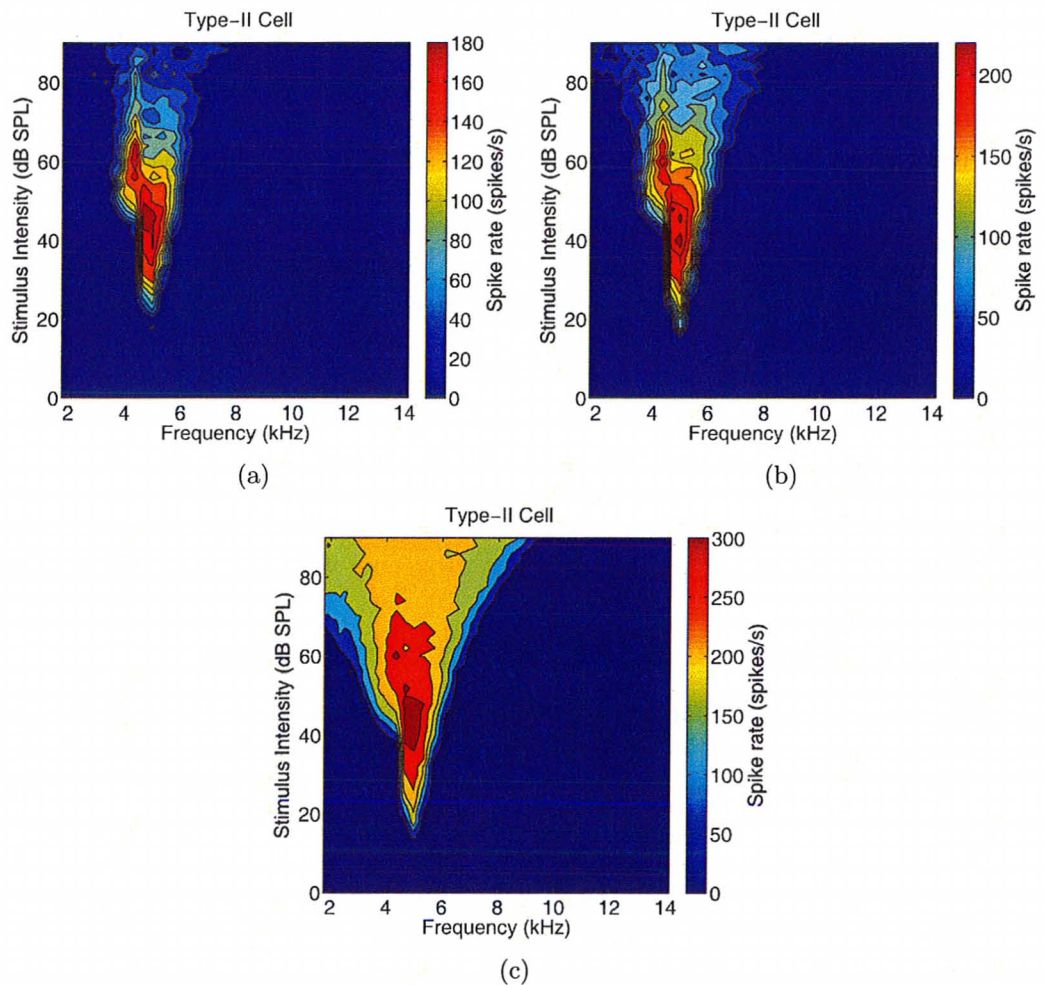


Figure 3.10: Changes to type-II cell responses resulting from changes to DCN model connection parameters. (a) shows the effect of decreasing the AN connection strength to W-cells to 0.04 the type-II response. (b) shows the further effect of decreasing the input AN bandwidth to type-II cells to 0.3 octaves. (c), shows the effects of increasing the AN fiber connection strength to the type-II cell to 0.55 and decreasing the W-cell connection strength to 1.3. The changes from each figure are carried into the next. Zilany and Bruce AN fibers were used as input.

section 3.3.3.

The resulting response maps (RMs) from these simulations can be seen in Figure 3.11. Comparing these results to those of DCN cells modeled using the Carney (1993) model (shown in Figure 3.6) we see that our type III and type IV cells shows similar response characteristics. There was a significant level of difficulty in matching the RMs of type IV-T cells. The response shown was the closest response we could generate. While it may not be immediately evident, this simulated cell still shows many of the characteristics of type IV-T behaviors. The main discrepancy is a significant amount of excitatory behavior to tones significantly below BF at high intensities. Figure 3.12 shows iso-intensity plots of our simulated type IV-T cell. Excluding the extra excitatory regions below BF at high intensities, these results are quite similar to unimpaired DCN type IV-T cells recorded by Ma and Young (2006).

An important result of these simulations is the importance of the non-specific afferents in the DCN model. The DCN cell responses simulated in Zheng and Voigt (2006) were generated with $\sigma_{NSA \rightarrow P}$ set to zero. The Carney (1993) model AN fibers Zheng and Voigt (2006) were using produced canonical DCN cell RMs without the need for modeled non-specific afferents because of properties of the Carney (1993) model, not because non-specific afferents have no effect on DCN cell responses. DCN cells simulated using the Zilany and Bruce (2007) model of the auditory periphery are all characterized by much broader responses as well as lower thresholds, in all cases. An overall increase in inhibition for each cell would serve to raise the cell firing thresholds. Additional sideband inhibition could be used to constrict DCN cell responses, allowing for increased frequency resolution. Finally, DCN cells simulated using Zilany and Bruce (2007) model AN inputs have a tendency to behave strangely at extremely high stimulus intensities. This is due to the saturation that occurs in AN input firing rates at these intensities. This suggests that the GABAergic, cartwheel cell and granule cell afferents (shown in the physiological DCN cell model in section 2.2.4.2) may also be involved in changing the overall excitability of DCN principal cells in response to loud stimuli to maintain the efficacy of their desired function. These findings also suggest that the non-specific afferents modeled in the Zheng and Voigt (2006) model may actually be inhibitory. The broad responses of simulated DCN cells receiving Zilany and Bruce (2007) AN inputs may be the result of the nature of synaptic connection strengths assigned in the Zheng and Voigt (2006) DCN model. Zheng and Voigt (2006) assigned synaptic connection strengths uniformly for all inputs. Due to the much broader responses of Zilany and Bruce (2007) AN fibers, this results in extremely broad DCN cell responses. Assigning connection strengths using a normal distribution based on distance from target cell BF could counteract these effects by ensuring that inputs further away from BF do not have as strong a connection as inputs at BF. The net result would be similar to the additional sideband inhibition described above. Lomakin and Davis (2008) used a

similar method of assigning synaptic connection strengths when simulating wideband inhibitors and were able to reproduce physiological responses.

3.4 Impaired Modeled Neurons in the DCN

Ma and Young (2006) recently performed a study that showed the response properties of DCN neurons both prior to and after being exposed to acoustic trauma. The recorded data of exposed animals did not show the typical organization of excitatory and inhibitory areas that characterized unexposed animals. DCN neurons showed either no response to sound, extremely weak responses, or “tail” responses. The two types of “tail” responses, as described by Ma and Young (2006), are shown in Figure 3.13. Class A tail responses are characterized by strong excitatory regions that extend deep into the low frequency ranges below BF. Class A responses have a low-pass filter shape that lacks any significant excitatory or inhibitory behavior above the cutoff frequency. In some cells exhibiting class A tail responses, excitatory regions can be seen with a two-tone stimulus pattern is used. Class B tails show significant excitation in the high frequency ranges, above BF. Due to the significant difference in response characteristics between impaired and unimpaired DCN cells, Ma and Young (2006) were not able to directly determine which DCN cell types were producing which tail responses.

We will attempt to examine the effects a modeled hearing impairment in the auditory periphery has on the response properties of simulated DCN principal cells in an attempt to see if the tail distributions viewed by Ma and Young (2006) are primarily the result of changes in the auditory periphery or plastic changes within the DCN. To do this we simulated three sets of Zilany and Bruce (2007) model inputs. Each set of AN inputs was given a different compound action potential (CAP) threshold shift function from which estimates of C_{OHC} and C_{IHC} were obtained for each simulated AN fiber using the *fitaudiogram()* function provided with the Zilany and Bruce (2007) model. A CAP threshold shift function is like an AN tuning curve only instead of looking at the firing threshold of one fiber you are looking at the net firing rate of a large number of AN fibers. The three CAP threshold shift functions modeled three different scenarios: (i) significant threshold shifts extending to frequencies well below DCN cell BF (from 1 kHz and above), (ii) threshold shifts beginning just above BF (6 kHz and above) and (iii) threshold shifts starting at frequencies well above BF (10 kHz). These three cases are important because they allow us to determine if the tail distributions shown by Ma and Young (2006) were dependant on the DCN cell BF relative to the rising edge of CAP threshold shift function. CAP threshold shift functions were reproduced from Figure 1A of Ma and Young (2006) to allow more direct comparisons to the recorded data.

Figures 3.14, 3.15 and 3.16 show the response maps of simulated cells for each DCN

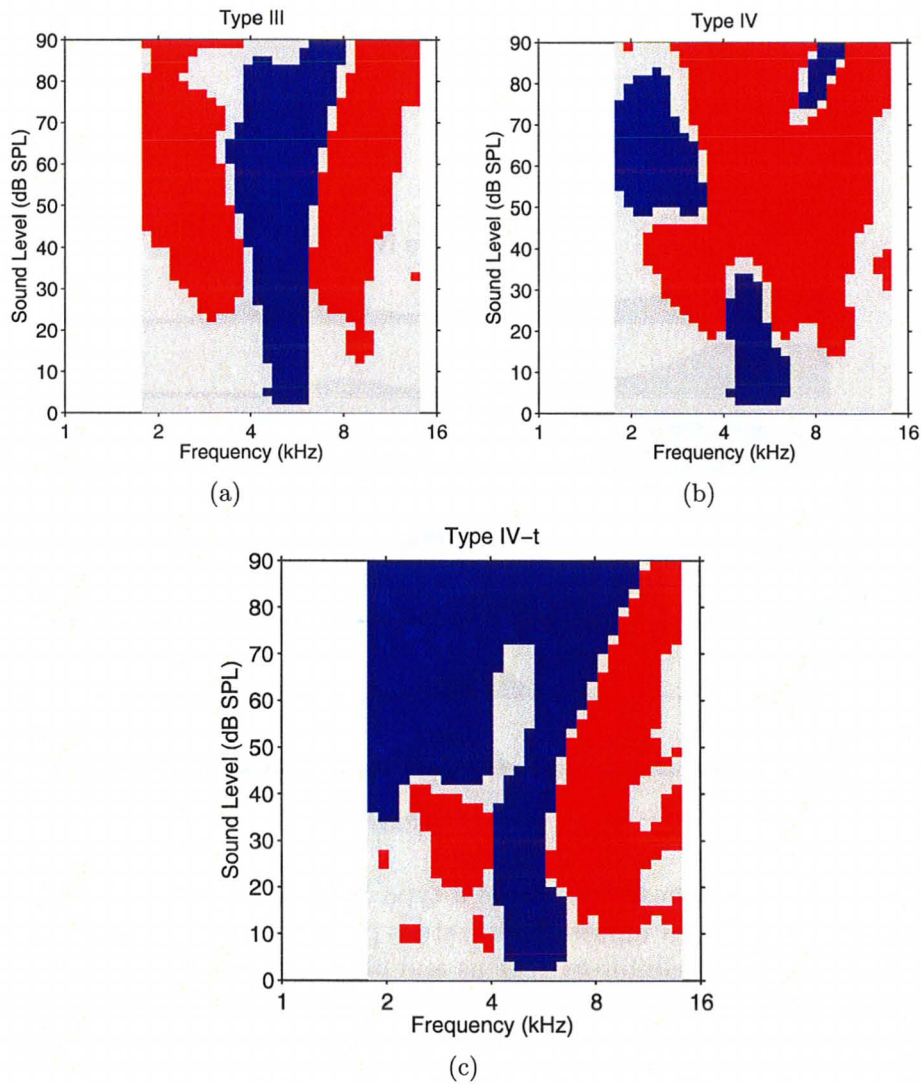


Figure 3.11: Response maps of simulated DCN principal cells receiving Zilany and Bruce (2007) AN inputs. Inhibitory regions (red) and excitatory regions (blue) are shown for each principal cell response type at each tone stimulus frequency and intensity. All non-coloured regions indicate spontaneous activity. (a), (b) and (c) show type III, IV and IV-T responses, respectively. Zheng and Voigt (2006) model parameters used to generate these responses can be found in Appendix A.4.

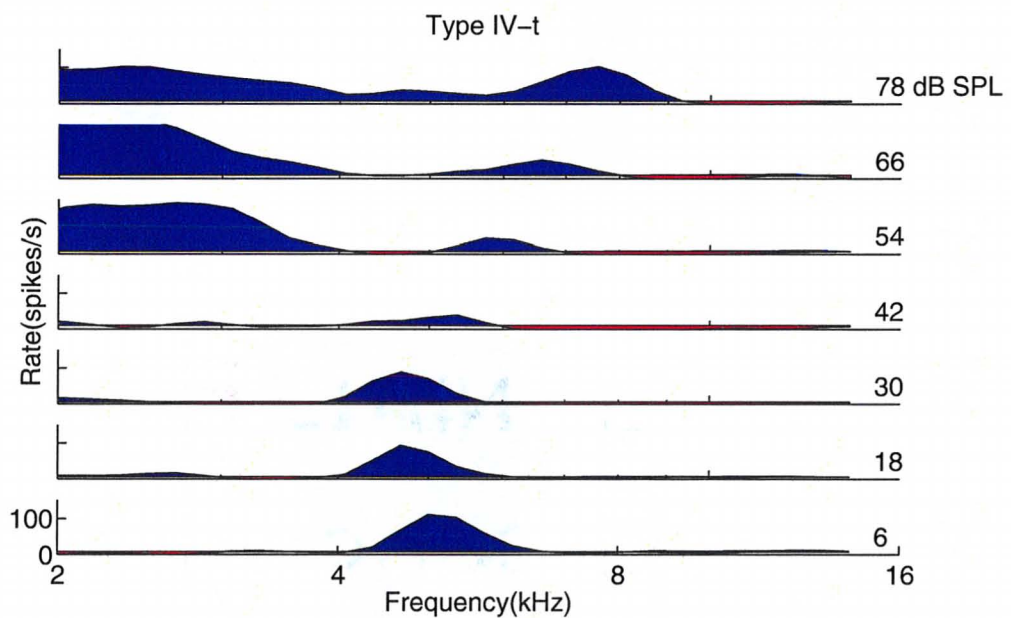


Figure 3.12: Iso-intensity curves of a type IV-T DCN principal cell receiving Zilany and Bruce (2007) AN inputs. Spike rate is plotted relative to spontaneous firing rate. Red areas indicate inhibitory regions and blue areas indicate excitatory regions. The stimulus intensity of each curve is listed to the far right. Frequencies were varied in 0.1 octave steps within a 1.5 octave band above and below 5 kHz. Zheng and Voigt (2006) model parameters used to generate these responses can be found in Appendix A.4.

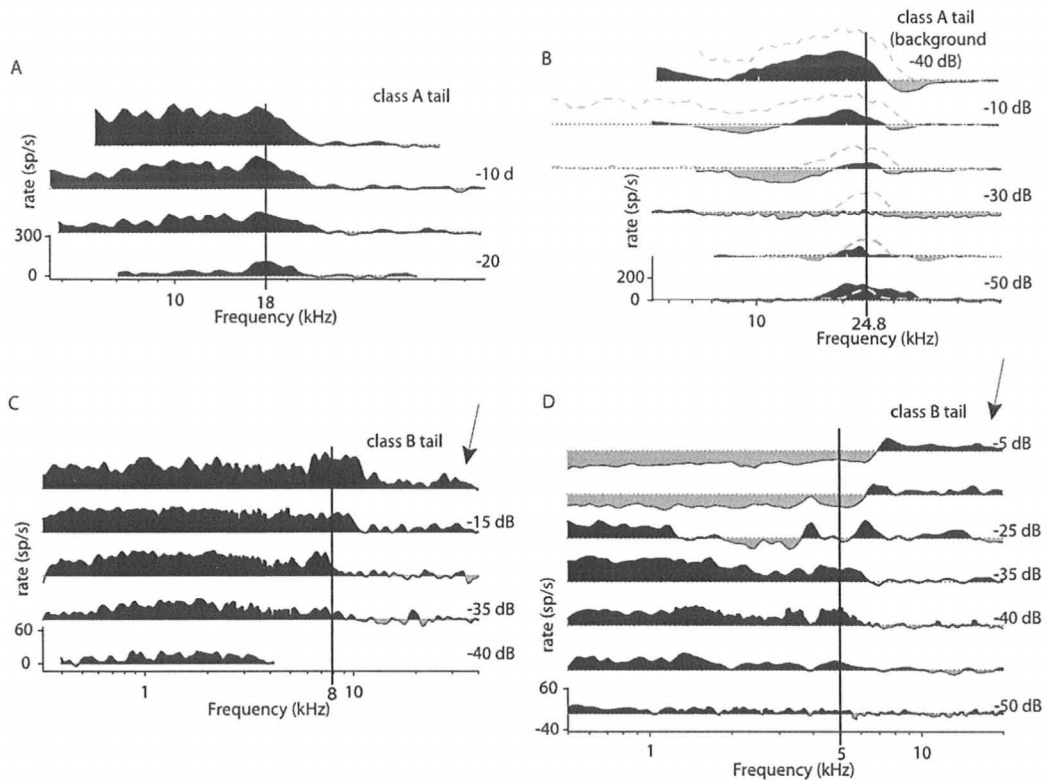


Figure 3.13: All figures show iso-intensity curves with spike rate relative to spontaneous being plotted against stimulus frequency. Filled grey areas indicate inhibitory regions and filled black regions indicate excitatory regions. The stimulus intensity relative to 100 dB SPL is shown to the far right of each figure. (A) A class A tail response map showing no inhibition. (B) Class A tail response map with inhibition. Single-tone (dashed line) and two-tone (filled map) response maps are shown. Second tone is required to reveal inhibitory regions. (C) Class B tail response. Note that region of excitatory activity that extends to high frequencies. (D) Class B tail response map showing inhibition. (Figures 2 E-H reprinted from Ma and Young (2006))

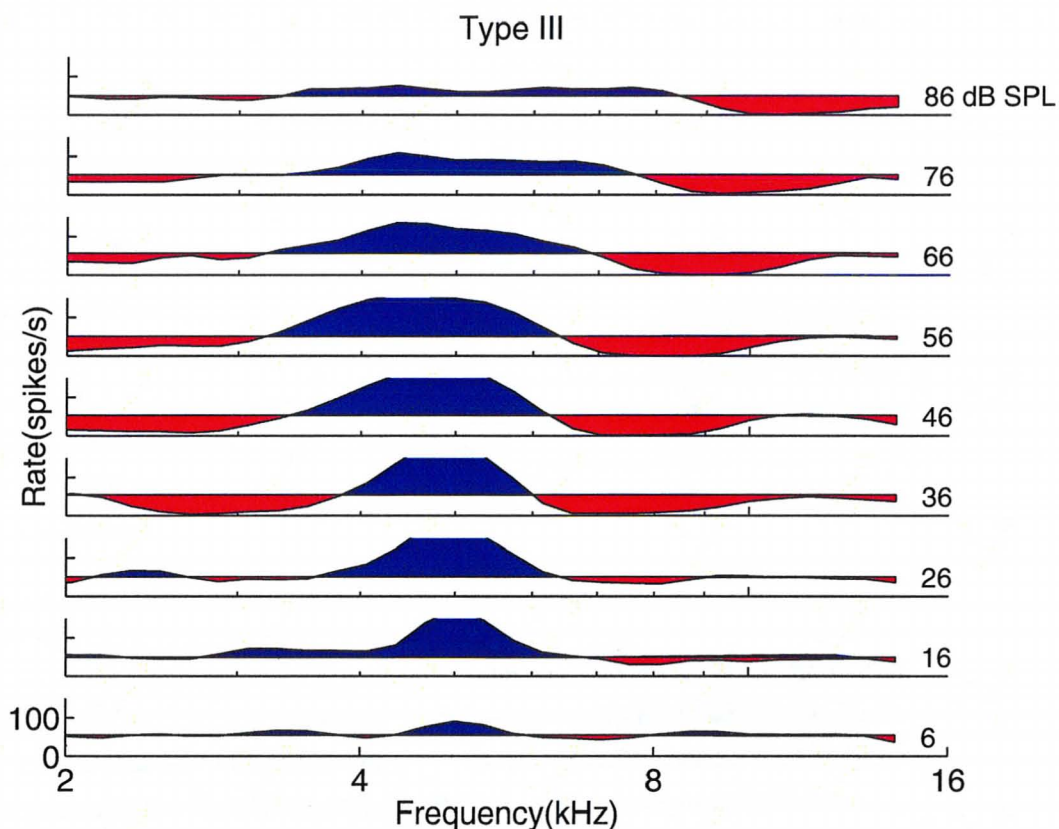


Figure 3.14: Iso-intensity curves of a simulated type III DCN principal cell receiving impaired Zilany and Bruce (2007) AN inputs with CAP threshold shifts beginning at 10 kHz. Similar to Figure 3.12.

primary cell type receiving simulated impaired Zilany and Bruce (2007) AN model fibers with a CAP threshold shift function with a rising edge at 10 kHz. Therefore almost all modeled AN fibers with CFs below 10 kHz will not be exhibiting any effects of hearing impairment. Our simulated DCN primary cells have BFs of 5 kHz, well below the rising edge of the CAP audiogram. As such, we would not expect any significant differences in our simulated DCN cell responses. Figures 3.14, 3.15 and 3.16 confirm this hypothesis by exhibiting no noticeable changes in behavior.

Responses of DCN cells simulated using impaired AN inputs with a CAP threshold shift function rising edge just above BF (6 kHz) are shown in Figures 3.17, 3.18 and 3.19. Our simulated type III response shows tail distributions similar to the single tone response in panel B of Figure 3.13. The inhibitory sideband that was present at high intensities in Figure 3.14 has now been replaced by a region of excitation that extends throughout the lower frequency region. Our type IV cell shows regions of

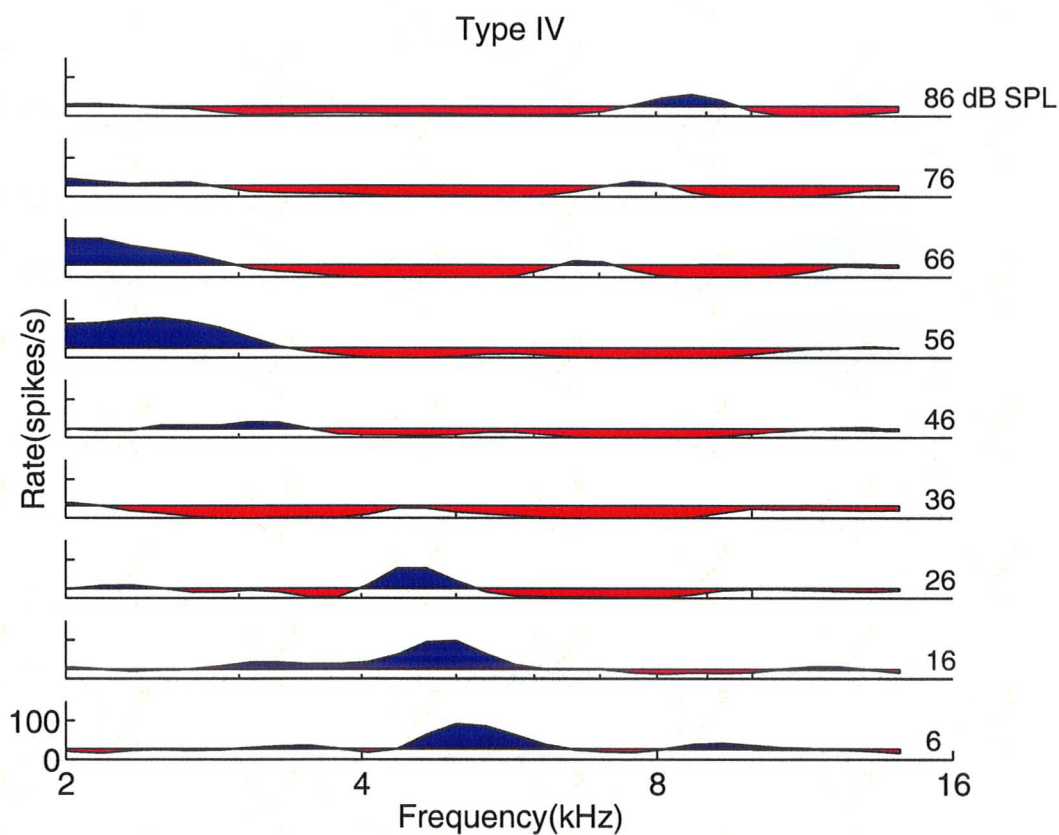


Figure 3.15: Iso-intensity curves of a simulated type IV DCN principal cell receiving impaired Zilany and Bruce (2007) AN inputs with CAP threshold shifts beginning at 10 kHz. Similar to Figure 3.12.

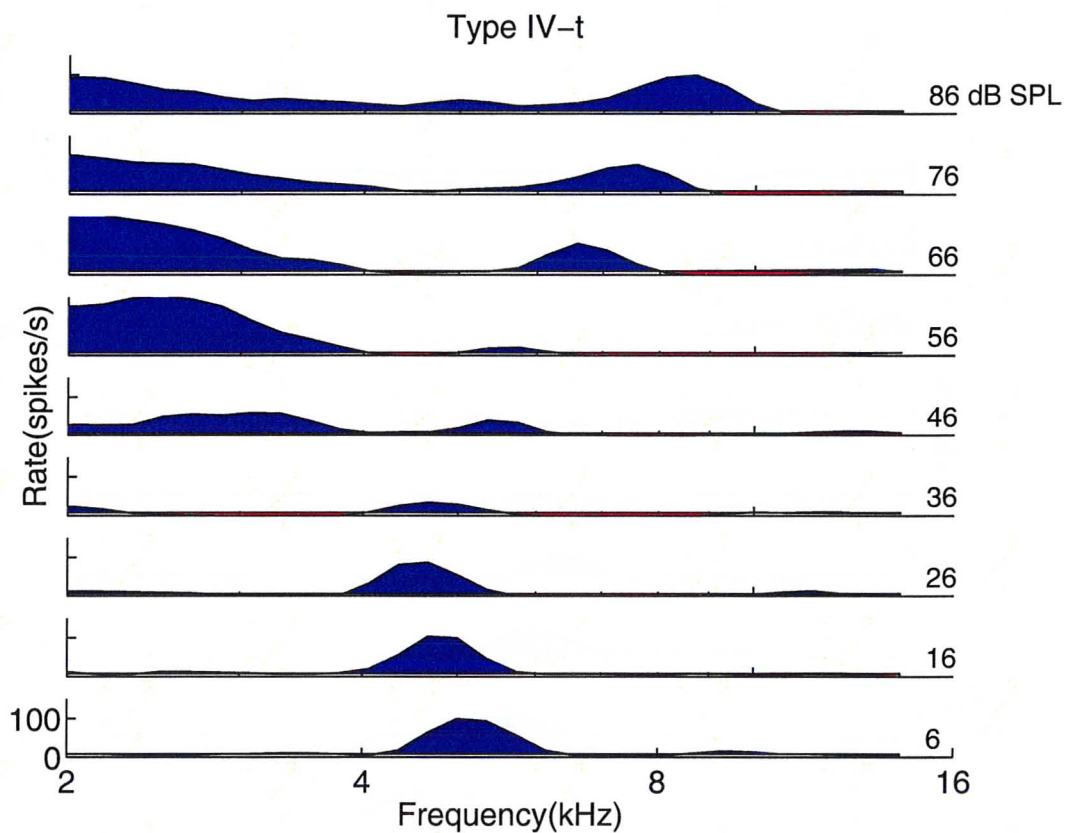


Figure 3.16: Iso-intensity curves of a simulated type IV-T DCN principal cell receiving impaired Zilany and Bruce (2007) AN inputs with CAP threshold shifts beginning at 10 kHz. Similar to Figure 3.12.

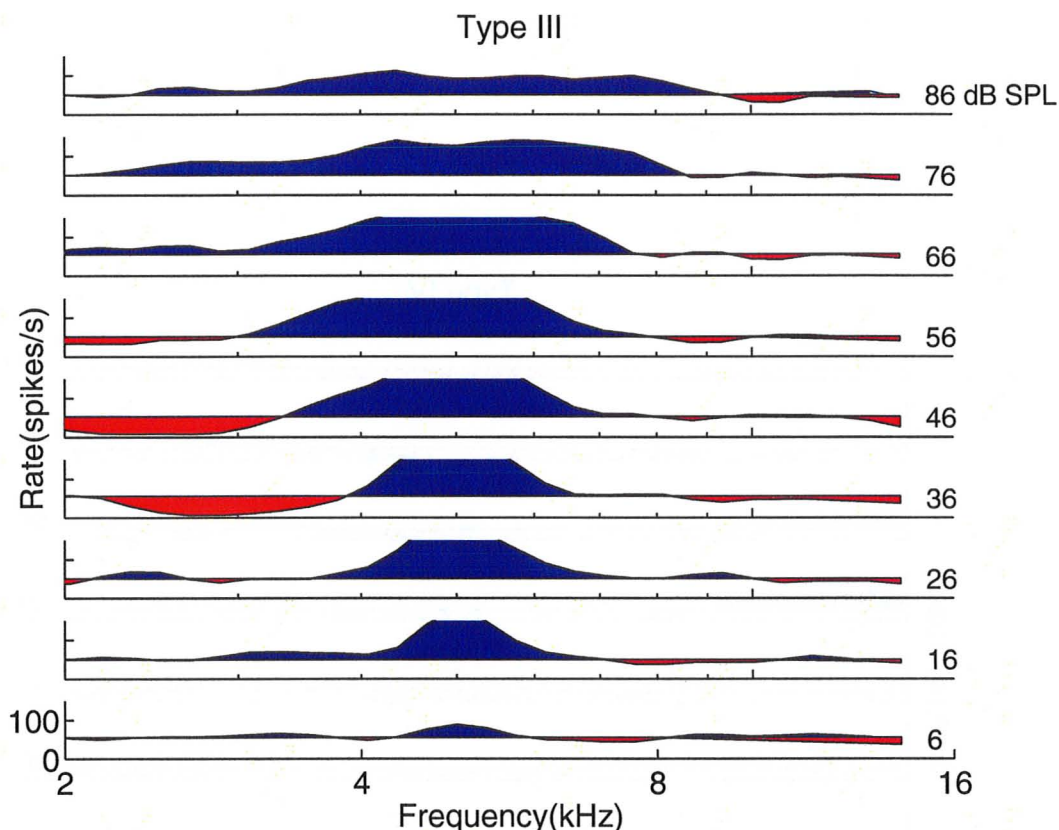


Figure 3.17: Iso-intensity curves of a simulated type III DCN principal cell receiving impaired Zilany and Bruce (2007) AN inputs with CAP threshold shifts beginning at 6 kHz. Similar to Figure 3.12.

excitation extending through the high frequency region similar to panel D of Figure 3.13 that did not exist when the AN inputs were not impaired which suggests the formation of class B tail. Our simulated type IV-T cell showed a similar result at high frequencies. Figure 3.19 shows a class B-like tail at high intensities and frequencies.

We finally examine the case where there is hearing impairment across, virtually, all simulated AN inputs to our simulated Zheng and Voigt (2006) model cells. In this case, our CAP threshold shift function has threshold increases starting at 1 kHz. Figures 3.20, 3.21 and 3.22 show the responses of type III, IV, and IV-T DCN cells receiving AN inputs with significant threshold shifts. Each figure showed increases in threshold intensity and overall decreases in firing rate. Our simulated type III and IV DCN cells did not show tail distributions in response to impaired AN fiber inputs. Our type IV-T cell (shown in Figure 3.22) did show an increase in excitation at higher frequencies suggesting the presence of a class B tail. The region of excitation at higher

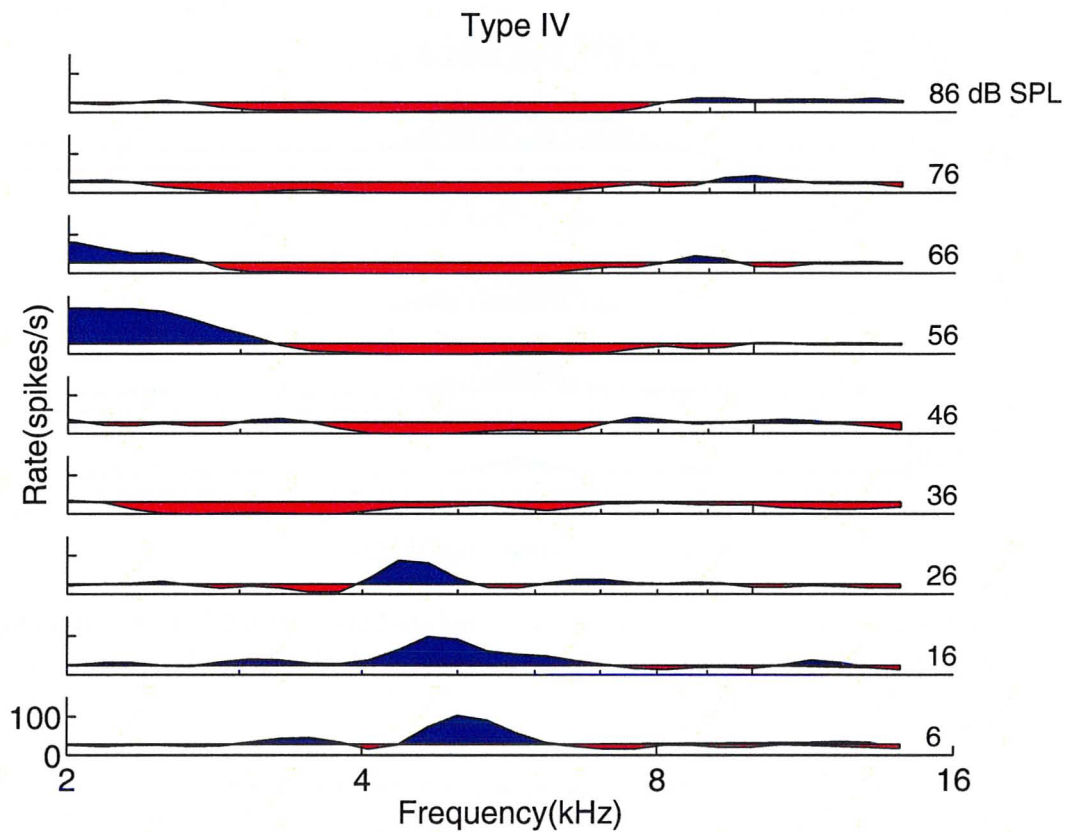


Figure 3.18: Iso-intensity curves of a simulated type IV DCN principal cell receiving impaired Zilany and Bruce (2007) AN inputs with CAP threshold shifts beginning at 6 kHz. Similar to Figure 3.12.

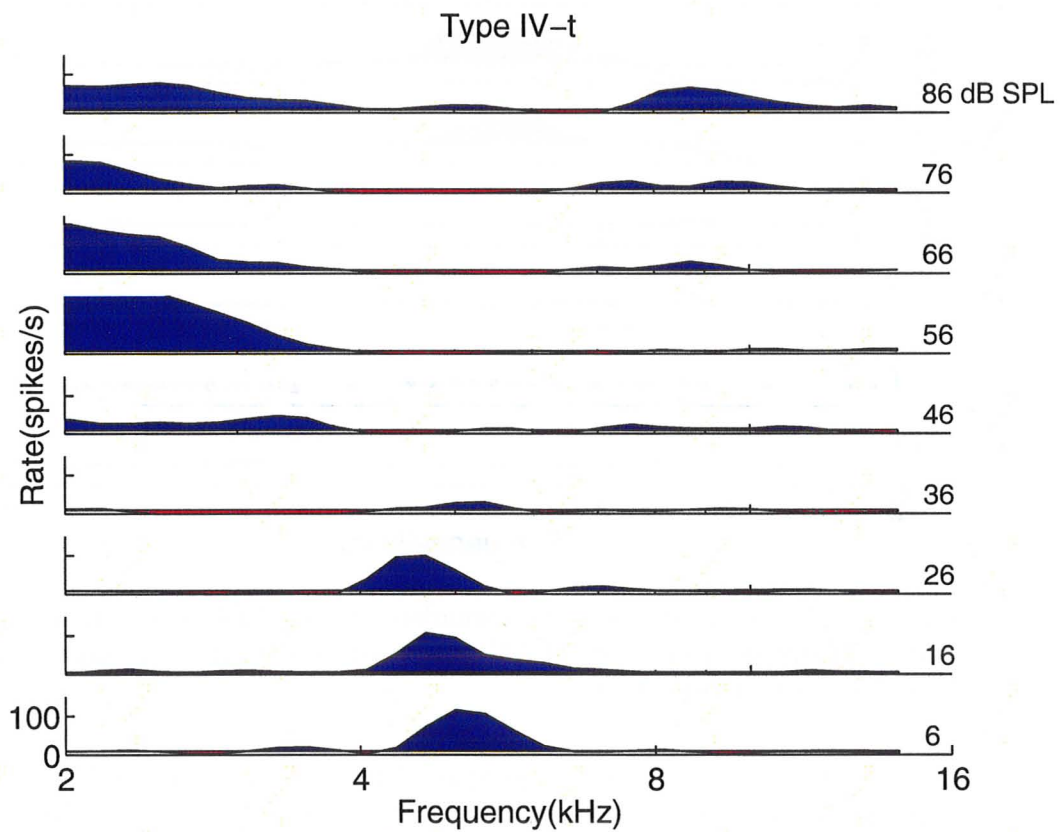


Figure 3.19: Iso-intensity curves of a simulated type IV-T DCN principal cell receiving impaired Zilany and Bruce (2007) AN inputs with CAP threshold shifts beginning at 6 kHz. Similar to Figure 3.12.

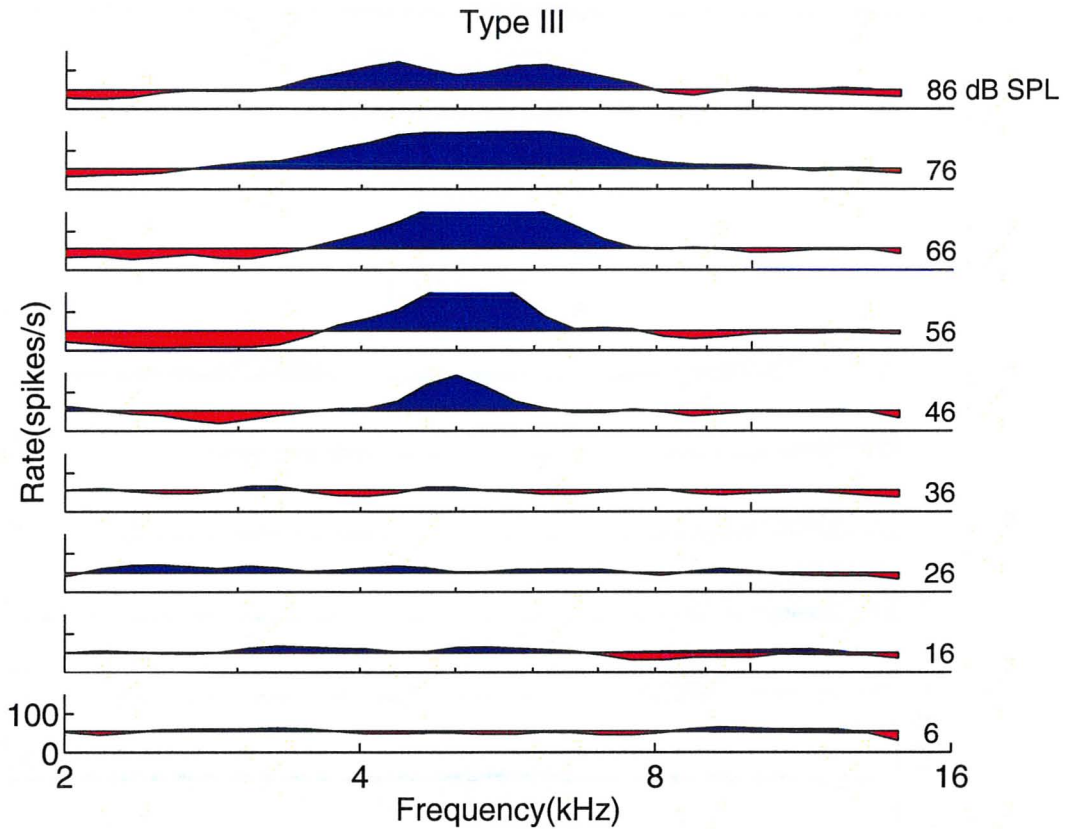


Figure 3.20: Iso-intensity curves of a simulated type III DCN principal cell receiving impaired Zilany and Bruce (2007) AN inputs with CAP threshold shifts beginning at 1 kHz. Similar to Figure 3.12.

frequencies was not as prominent as that of the simulated type IV-T cell receiving impaired AN inputs with CAP threshold shifts beginning just above BF.

From these results we see that tail distributions are primarily caused by DCN cells whose AN inputs have a CAP threshold shift function with a rising edge just above BF. Class A tails appear to come from type III cells and class B tails appear to occur in type IV and type IV-T cells. When the rising edge of the CAP threshold shift is significantly above BF (~ 1 octave), there is very little noticeable change in the response properties of DCN cells. When the rising edge of the CAP audiogram is well below BF, simulated DCN cell responses show minimal spike activity and increased spike thresholds. Type IV-T cells receiving this configuration of impaired AN inputs showed possible class B tail distributions. These results confirm previous indications by Zheng *et al.* (2008) that the Zheng and Voigt (2006) DCN model in conjunction with the Zilany and Bruce (2007) model is able to model the tail distributions that

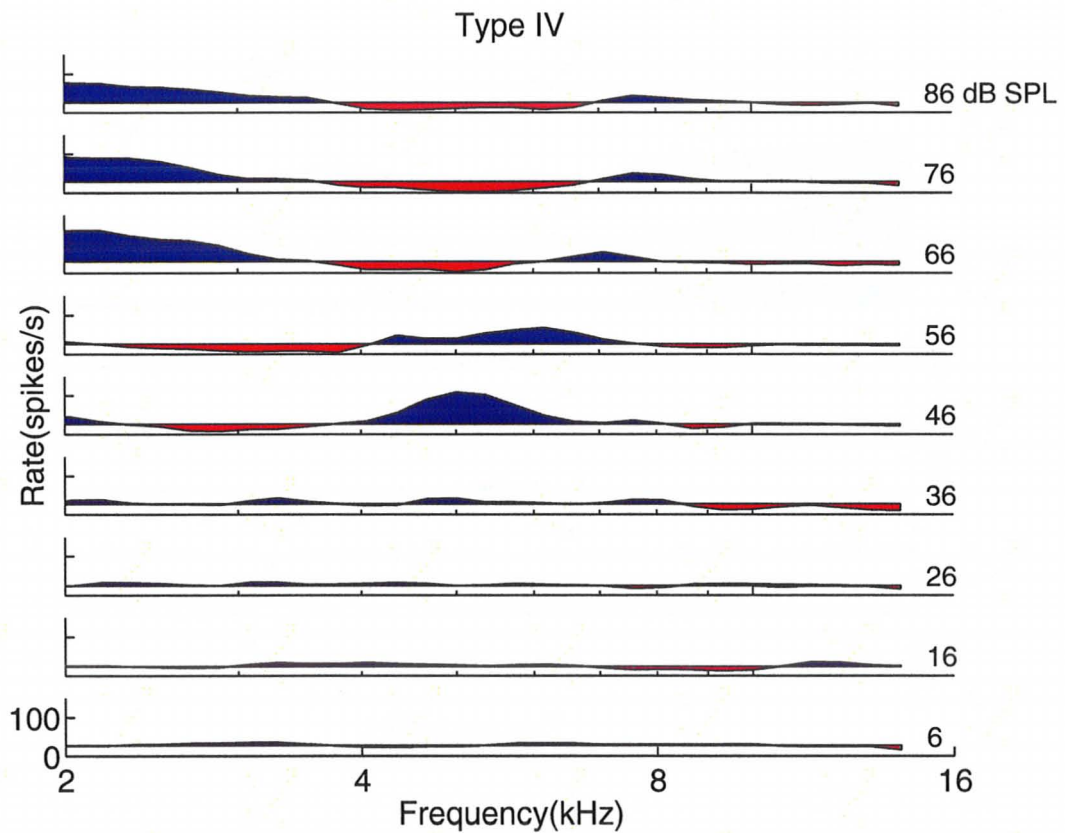


Figure 3.21: Iso-intensity curves of a simulated type IV DCN principal cell receiving impaired Zilany and Bruce (2007) AN inputs with CAP threshold shifts beginning at 1 kHz. Similar to Figure 3.12.

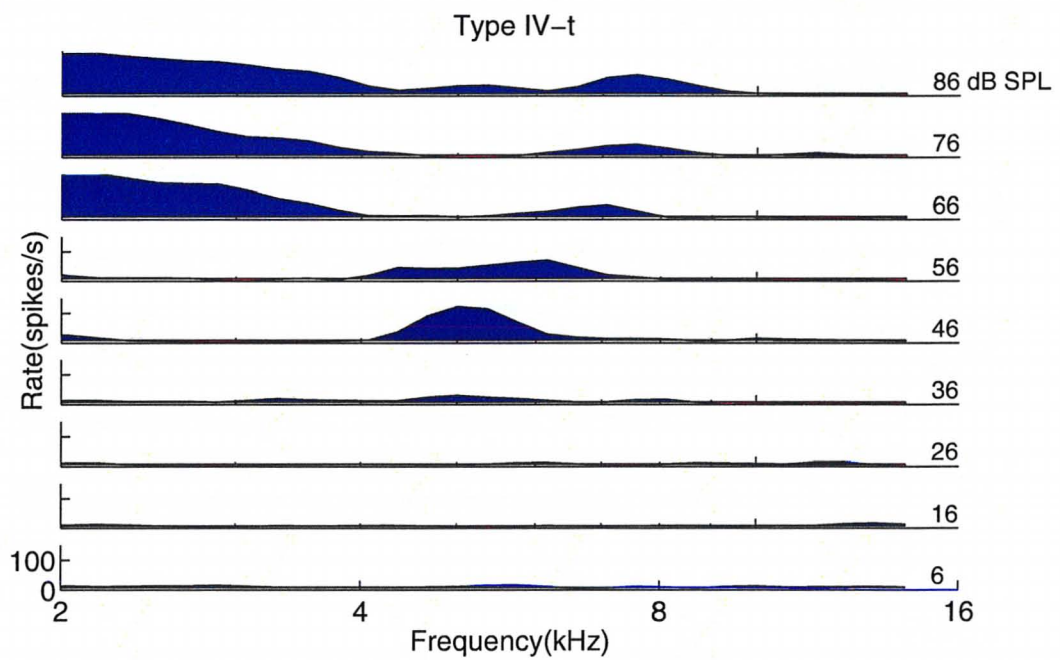


Figure 3.22: Iso-intensity curves of a simulated type IV-T DCN principal cell receiving impaired Zilany and Bruce (2007) AN inputs with CAP threshold shifts beginning at 1 kHz. Similar to Figure 3.12.

arise in impaired DCN cells. It should be noted that the results shown for simulated type IV-T cells should be approached with caution as they provided the least accurate responses to unimpaired AN inputs.

Chapter 4

The Effects of Hearing Loss on Modeled Neurons in the VCN

In this chapter, the Rothman and Manis (2006c) model of VCN cells is implemented receiving AN synaptic inputs produced by the Zilany and Bruce (2007) model. The implementation of the Rothman and Manis (2006c) model used in these works is described as well as issues encountered. A set of physiological AN input configurations for each type of VCN cell is presented. A computational study of the responses of VCN cells receiving Zilany and Bruce (2007) model AN inputs to a variety of acoustic stimuli is presented and results are compared to physiological recordings. Hearing impairment is then modeled in the auditory periphery and the effects on VCN cell response properties are examined and compared to physiological recordings of VCN cells following acoustic trauma by Cai *et al.* (2008). Simulation results are compared to physiological recordings to determine if the responses shown by Cai *et al.* (2008) can be entirely explained by impairment in the auditory periphery.

4.1 Rothman and Manis Model

The VCN circuit model used in these works is the Rothman and Manis (2006c) model. This VCN model is a Hodgkin-Huxley type neuron model. It consists of six different ionic currents, the membrane capacitive current and synaptic input currents. The current equation for the VCN cell is

$$-C_m \frac{dV}{dt} = I_A + I_{LT} + I_{HT} + I_{Na} + I_h + I_{lk} + I_E - I_{ext} \quad (4.1)$$

where C_m is the membrane capacitance (12 pF).

Of the ionic currents modeled by Rothman and Manis (2006c), three are different types of potassium (K^+) currents. These ionic currents represent the different K^+

currents found in the various types of VCN neurons (outlined in 2.2.4.1 on page 45). I_A is the fast inactivating K^+ current, I_{LT} the slow-inactivating low-threshold K^+ current and I_{HT} the high-threshold delayed-rectifier-like K^+ current. Rothman and Manis (2006a) performed a series of voltage clamp experiments on guinea pig VCN neurons. They found that they were able to sub-divide VCN neurons into different types, depending on the ionic currents present. Type II VCN neurons (bushy cells) showed the presence of both I_{HT} and I_{LT} , whereas type I VCN neurons (stellate cells) possessed only I_{HT} . Type I neurons were further subdivided into I-c or “classic” types and I-t or “transient” types. The differentiating factor between the two was the presence of I_A . Type I-t neurons showed signs of I_A whereas type I-c neurons did not (Rothman and Manis, 2006a).

Using the results of the voltage clamp experiments, Rothman and Manis (2006b) were able to characterize the K^+ current kinetics. The ionic currents were defined in the classical Hodgkin-Huxley formalism (see 2.1.2.2 on 13). The equations for the K^+ currents can be seen below:

$$I_A = \bar{g}_A a^4 b c (V - V_k) \quad (4.2)$$

$$I_{LT} = \bar{g}_{LT} w^4 z (V - V_k) \quad (4.3)$$

$$I_{HT} = \bar{g}_{HT} (\varphi n^2 + (1 - \varphi) p) (V - V_k) \quad (4.4)$$

I_A was found to have fourth-order activation kinetics (a^4). Two inactivation particles (b and c) were required to fully characterize I_A recovery from inactivation. I_{LT} is characterized by an activation particle with fourth order kinetics (w^4) and an inactivation particle (z). The kinetics of I_{HT} are slightly more complicated. I_{HT} has two activation gating particles with unique kinetics. The n^2 particle has second-order kinetics and the p particle has first order kinetics. When the effects of the two activation particles are summed together ($n^2 + p$), the resulting behavior matches current clamp recordings. The φ variable in I_{HT} is a weighting factor that best matches the gating particle dynamics to the recordings (Rothman and Manis, 2006b).

The rate of change for all gating particle variables in the VCN model is calculated using the following first-order differential equation

$$\frac{dx}{dt} = \frac{(x_\infty - x)}{\tau_x} \quad (4.5)$$

where x is a particular gating particle, x_∞ is the steady-state value of the gating particle (as $t \rightarrow \infty$) and τ_x is the state time constant. The steady state behavior of the gating particles was modeled using curve-fitted Boltzmann functions (Rothman and Manis, 2006b). Equations for the steady state behavior of each K^+ current gating

particle, as a function of membrane potential, is described by

$$a_{\infty} = [1 + \exp(-(V + 31)/6)]^{-1/4} \quad (4.6)$$

$$b_{\infty} = [1 + \exp((V + 66)/7)]^{-1/2} \quad (4.7)$$

$$c_{\infty} = b_{\infty} \quad (4.8)$$

$$w_{\infty} = [1 + \exp(-(V + 48)/6)]^{-1/4} \quad (4.9)$$

$$z_{\infty} = 0.5[1 + \exp((V + 71)/10)]^{-1} + 0.5 \quad (4.10)$$

$$n_{\infty} = [1 + \exp(-(V + 15)/5)]^{-1/2} \quad (4.11)$$

$$p_{\infty} = [1 + \exp(-(V + 23)/6)]^{-1} \quad (4.12)$$

State time constants as a function of voltage were fit to bell-shaped functions. The resulting functions for each of the K^+ current state time constants are

$$\tau_a = 100[7 \exp((V + 60)/14) + 29 \exp(-(V + 60)/24)]^{-1} + 0.1 \quad (4.13)$$

$$\tau_b = 1000[14 \exp((V + 60)/27) + 29 \exp(-(V + 60)/24)]^{-1} + 1 \quad (4.14)$$

$$\tau_c = 90[1 + \exp(-(V + 66)/17)]^{-1} + 10 \quad (4.15)$$

$$\tau_w = 100[6 \exp((V + 60)/6) + 16 \exp(-(V + 60)/45)]^{-1} + 1.5 \quad (4.16)$$

$$\tau_z = 1000[7 \exp((V + 60)/20) + \exp(-(V + 60)/8)]^{-1} + 50 \quad (4.17)$$

$$\tau_n = 100[11 \exp((V + 60)/24) + 21 \exp(-(V + 60)/23)]^{-1} + 0.7 \quad (4.18)$$

$$\tau_p = 100[4 \exp((V + 60)/32) + 5 \exp(-(V + 60)/25)]^{-1} + 5 \quad (4.19)$$

The sodium current (I_{Na}) model used by Rothman and Manis (2006c) was derived from previous studies of rat neurons. Voltage clamp studies by Belluzzi *et al.* (1985)

and Costa (1996) of neurons in the rat were used to derive the following expression for Na^+ current:

$$I_{\text{Na}} = \bar{g}_{\text{Na}} m^3 h (V - V_{\text{Na}}) \quad (4.20)$$

The steady state behavior for the Na^+ activation (m) and inactivation (h) particles, as functions of voltage, are shown below, respectively:

$$m_{\infty} = [1 + \exp(-(V + 15)/5)]^{-1/2} \quad (4.21)$$

$$h_{\infty} = [1 + \exp(-(V + 23)/6)]^{-1} \quad (4.22)$$

I_{Na} gating particle state time constants as functions of voltage are described by:

$$\tau_m = 10[5 \exp((V + 60)/18) + 36 \exp(-(V + 60)/25)]^{-1} + 0.04 \quad (4.23)$$

$$\tau_h = 100[7 \exp((V + 60)/11) + 10 \exp(-(V + 60)/25)]^{-1} + 0.6 \quad (4.24)$$

Similar to the Na^+ current, the model for the hyperpolarization-activated cation current (I_h) used by Rothman and Manis (2006c) in their VCN model was derived from previous studies. Patch-clamp studies of auditory neurons by Fu *et al.* (1997), Banks *et al.* (1993) and non auditory neurons in rats by Huguenard and McCormick (1992) and Travagli and Gillis (1994) were the source of the following relationship for I_h :

$$I_h = \bar{g}_h r (V - V_h) \quad (4.25)$$

The steady state behavior for the I_h activation particle (r) as a function of voltage is given by:

$$r_{\infty} = [1 + \exp((V + 76)/7)]^{-1} \quad (4.26)$$

The state time constant for r as a function of voltage is:

$$\tau_r = 10^5[237 \exp((V + 60)/12) + 17 \exp(-(V + 60)/14)]^{-1} + 25 \quad (4.27)$$

The membrane leakage current is modeled by:

$$I_{\text{lk}} = \bar{g}_{\text{lk}} (V - V_{\text{lk}}) \quad (4.28)$$

where \bar{g}_{lk} is the maximum steady-state conductance (2 nS).

Excitatory post-synaptic currents (I_E) were modeled using:

$$I_E = g_E(V - V_E) \quad (4.29)$$

where g_E is the time-dependant conductance change in response to an excitatory synaptic input. g_E was modeled as an α -wave of the form:

$$g_E = \bar{g}_E(t/\tau_E) \exp[1 - (t/\tau_E)] \quad (4.30)$$

where \bar{g}_E is the peak conductance and τ_E the time to peak.

The VCN model uses various configurations of AN synaptic inputs. Due to the differences between the types of synaptic connections to the various VCN cell types, \bar{g}_E takes on different values for the various cell types. The VCN model has two different types of synaptic inputs: (i) subthreshold inputs and (ii) suprathreshold inputs. Suprathreshold AN inputs are strong synaptic inputs that are able to cause an action potential in a VCN cell individually. Subthreshold inputs are weaker synaptic inputs that are unable to raise the VCN cell potential beyond the action potential threshold on their own. Several coincident synaptic subthreshold inputs would be required to generate an action potential in a VCN cell. To allow for these different synaptic inputs, the VCN model uses a parameter called the synaptic efficacy ($\bar{g}_{E\theta}$). $\bar{g}_{E\theta}$ is defined as the minimum value of \bar{g}_E necessary for a single AN synapse to generate an action potential. For a subthreshold synaptic input $\bar{g}_E = 0.5\bar{g}_{E\theta}$. For suprathreshold inputs $\bar{g}_E = 3\bar{g}_{E\theta}$.

Table 4.1 lists the current parameters and cell properties for all of the cell types modeled by the Rothman and Manis (2006c) model. Table 4.2 contains the reversal potentials for all of the ionic currents used in the Rothman and Manis (2006c) model.

Unless otherwise specified, the equations shown above are all for VCN responses for cells measured at room temperature. In order to match the model to physiological temperatures (38°C), all time constants were multiplied by 0.17 (a reciprocal Q10 factor of 3) and all peak conductance values were multiplied by 3.03 (a Q10 factor of 2). τ_E was set to 0.07ms for simulations at 38°C (Rothman and Manis, 2006c).

4.1.1 Model Implementation

The Rothman and Manis (2006c) model was coded in MATLAB version 7.1.0.246, revision 14. An ordinary differential equation (ODE) solver was coded for the system of differential equations outlined above. A fourth order Runge-Kutta method of numerical integration was implemented with a constant time step for integration. Instead of having a distinct I_E current for each AN input, all synaptic input spike trains were summed and g_E was computed for the net result.

Table 4.1: VCN model parameters and properties. (Reproduced from Rothman and Manis (2006c))

	Model Type				
	I-c	I-t	I-II	II-I	II
\bar{g}_{Na} , nS	1000	1000	1000	1000	1000
\bar{g}_{HT} , nS	150	80	150	150	150
\bar{g}_{LT} , nS	0	0	20	35	200
\bar{g}_A , nS	0	65	0	0	0
\bar{g}_h , nS	0.5	0.5	2	3.5	20
\bar{g}_{lk} , nS	2	2	2	2	2
V_{rest} , mV	-63.9	-64.2	-64.1	-63.8	-63.6
R_{rest} , M Ω	473	453	312	244	71
τ_m , ms	7.0	4.0	3.7	2.9	0.9
V_{th} , mV	-38.3	-34.9	-51.2	-58.0	-62.2
$S_{-50/-70}$, nS	0.3	0.3	5.0	12.6	49.5
$\bar{g}_{E\theta}$ @ 22°C, nS	2.0	2.2	2.8	3.2	8.6
$\bar{g}_{E\theta}$ @ 38°C, nS	11	12	15	17	34

Table 4.2: VCN model reversal potentials. (Reproduced from Rothman and Manis (2006c))

Current Type	Reversal Potential (mV)
V_k	-70
V_{Na}	55
V_h	-43
V_{lk}	-65
V_E	0

In this particular implementation of the VCN model an α -wave vector was generated and convolved with the input AN spike train to create a g_E vector for the length of the simulation. The MATLAB “filter” function was used to perform the convolution since it produces an output vector of identical length to the input AN spike train, unlike the “conv” function. This computation gives a $g_E(t)$ vector as a function of time. The ODE solver is called for each time t and the value of g_E at that particular instance of t is provided as a constant for use in computing $\frac{dV}{dt}$.

All input AN spike trains were computed using a slightly-modified version of the Zilany and Bruce (2007) model. The original version of the Zilany and Bruce (2007) model used the GSL random number generator from the GNU scientific library on Win32 platforms and the drand48 on Unix platforms for the random spike time generating portion of the AN model. Both of these random number generators use the C “time” function to generate the initial seed for the random number generators. It was found that due to the extremely short length of the VCN stimuli (50ms for the tone stimulus followed by 50ms of silence) we would see several (~ 8) identical, repeating spike trains of successive simulated spike trains. The Zilany and Bruce (2007) model would finish computing an AN spike train so quickly that by the time it was called a second time the C “time” function would return an identical value and produce an identical spike train. After several iterations, enough time would pass that a new initial seed would occur resulting in another new set of repeating AN spike trains. This phenomenon can be seen in Figure 4.1.

To solve this issue, the Zilany and Bruce (2007) model was altered to use the MATLAB number generator instead. The MATLAB number generator was called by the C coded Zilany and Bruce (2007) model using the MEX C library functions. As shown by the raster plot on the right of Figure 4.1, the resulting spike trains showed random behavior in successive trials.

The system of ODEs used in the Rothman and Manis (2006c) VCN model is a stiff system. A stiff system is a system of differential equations that involves both rapidly changing and slowly changing components (Chapra and Canale, 2002). In such a system it is imperative that the step size used in computing the changes in the system of equations is small enough to maintain stability in the solution and allow sufficient accuracy. To ensure this was the case in our VCN simulations, the values of the state time constants for each gating particle were computed over a range of voltages (-100mV to 20mV). The fastest state time constant over that range of voltages for all gating particles was found to be approximately $63.4\mu s$.

A time step (Δt) of $1\mu s$ was selected for the ODE solver. This was done for two reasons. The first was to ensure that the ODE solver was at least ten times faster than the fastest state time constant in the VCN model. The second reason was to allow for easy up-sampling of AN fiber inputs. Our AN fiber inputs were simulated with a sampling frequency of 100kHz. In order to up-sample our AN fiber inputs, we

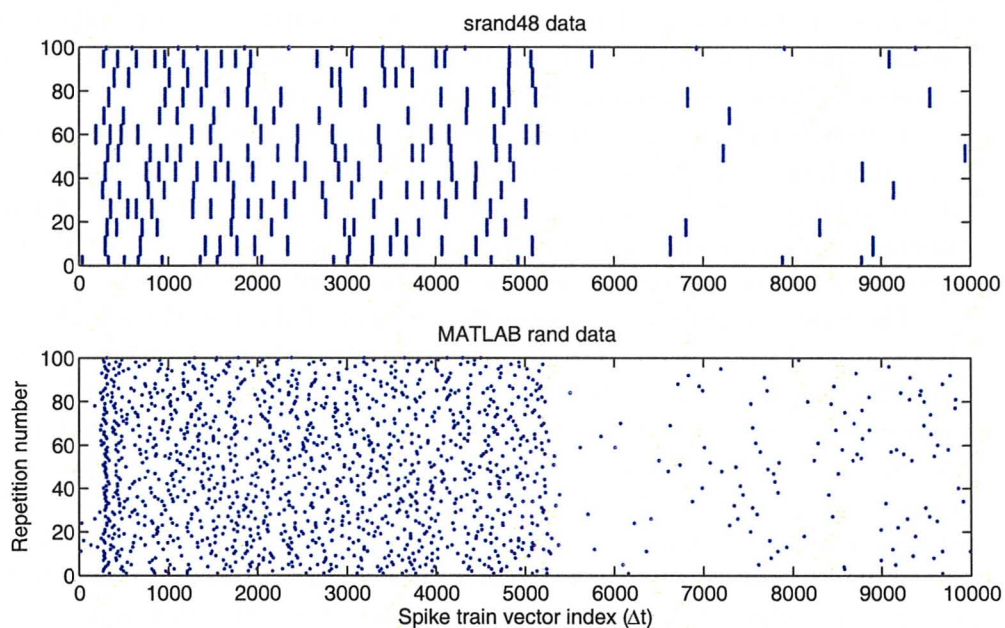


Figure 4.1: Shows raster plots of simulated Zilany and Bruce (2007) model AN fibers using two different random number generators for the spike generator. Each line on the curve represents a single stimulus repetition and each blue point indicates the time of an action potential in terms of simulation time steps (Δt). (Top) Shows raster plots of AN fibers using the *srand48* random number generator. Notice the replication of the exact same response over successive simulation repetitions. (Bottom) Shows raster plots of an AN fiber simulated using the MATLAB random number generator (*rand*). Notice the increased variability between stimuli following the onset response of each stimulus repetition. Both figures show an AN fiber stimulated by 100 repetitions of a CF stimulus (5 kHz) at 30 dB SPL.

needed to select a Δt that would produce an integer value in the following expression

$$x = \frac{1}{F_S \Delta t} - 1 \quad (4.31)$$

where F_S is the AN model sampling frequency, Δt the VCN model ODE solver step size and the x the number of extra bins required to up-sample our input AN spike train vector. With a Δt of $1\mu s$, we require $x = 9$ extra bins to upsample our AN fibre spike trains for use in the ODE solver. To achieve this we simply add another 9 bins of zeros following each bin of the input AN spike train.

The output of our VCN model code is a transmembrane potential waveform ($V(t)$) as a function of time. This vector was then turned into a spike time waveform by use of a spike detection algorithm. $V(t)$ was, simply, scanned for peaks and at the location of each peak, an action potential was said to have occurred. The resulting spike time vectors were then used in all subsequent data analysis.

The most computationally intensive element of these works was the calculation of $V(t)$ by our ODE solver. In order to minimize total computational time, the model MATLAB scripts were parallellized as much as possible. Each MATLAB script was defined as a function with input variables corresponding to the desired input stimulus. A separate BASH script was created to concurrently submit several jobs to the GRID computing network at McMaster University. The simulations were split into two stages. First, all AN input data was generated in parallel and saved to “mat” files. Secondly, the previously generated AN input data was used to compute VCN output spike trains which were subsequently saved as “mat” files themselves.

For further details of how the VCN model was implemented see the MATLAB code in Appendix A.1.

4.1.2 Using Zilany-Bruce Model AN inputs

In their modeling study of VCN neurons, Rothman and Manis (2006c) used a simplified AN spike train model. The model was a modified version of the works of Johnson *et al.* (1986). Their method generates a renewal process described by its instantaneous rate function. The instantaneous rate process is able to produce a series of exponentially-distributed interspike intervals from a uniformly distributed series of random numbers (Rothman *et al.*, 1993). In essence, this method of modeling AN fiber inputs tries to produce a statistical model that reproduces the characteristics of the PSTHs of AN fiber inputs. While the model can reproduce some of the physiological phenomena of AN inputs, such as phase locking, adaptation characteristics and refractoriness, it limits possibilities for analysis. This particular AN model creates AN-like PSTHs for BF-tone stimuli. However, stimulus intensity and frequency are not variables in the model, only the BF or CF of the AN fiber. This prevents us from

being able to perform more robust analyses of VCN cell response properties, such as rate-level curves and response maps. We are also unable to model the effects of hearing loss using this method.

We shall, again, turn to the Zilany and Bruce (2007) model for generating our AN inputs. This model allows us three main benefits: (i) it allows us to generate rate-level and response map curves to perform a more robust analysis of the VCN cell responses, (ii) it allows us to explore the VCN model's ability to model the responses of VCN neurons with AN inputs that have configurations more similar to their anatomical counterparts and (iii) it allows us to model the effects of hearing impairment.

Two sets of AN input data were generated using the Zilany and Bruce (2007) model. The first set of data did not attempt to mimic anatomical AN input configurations to VCN cells. A set of data was generated with all AN fibers having identical CFs at the VCN cell BF. When simulating VCN cells with only 1 or 3 AN synaptic inputs, the spontaneous rates of the fibers were all set to 50 spikes/s. When simulating VCN cells with 50 inputs, AN fiber spont rates were randomly generated to give an anatomical distribution of spontaneous rates. Figure 4.2 shows the distribution of AN fiber SRs used in all VCN cell simulations with 50 synaptic inputs. AN input spike trains were computed in responses to tonal stimuli over a broad range of stimulus frequencies and intensities.

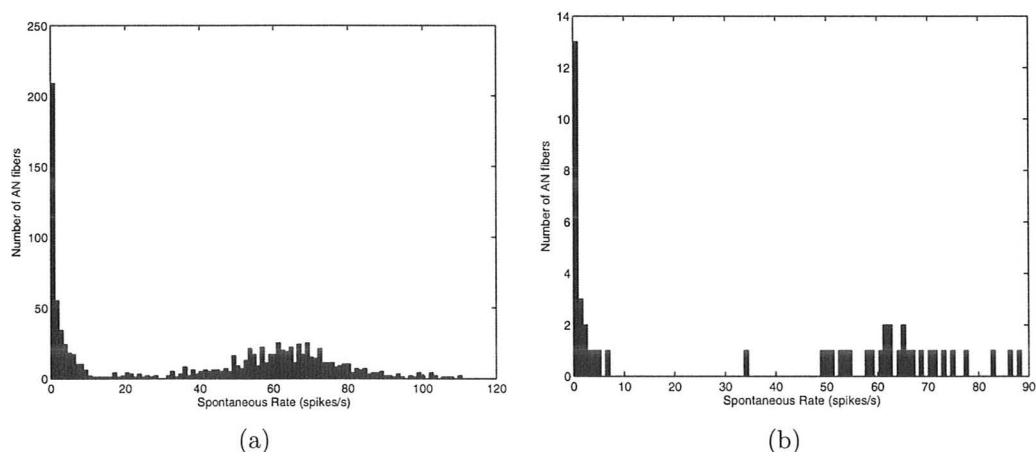


Figure 4.2: (a) shows a histogram of spontaneous firing rates of a population of 1000 AN fibers. This histogram is similar to distributions amongst recorded AN fiber populations. (b) show a histograms of the randomly generated spontaneous rates of the 50 simulated AN fibers used as inputs to our VCN cells. Notice how despite this fact this is a very small population of AN fibers, it matches the, overall, characteristics shown in (a) for a large population. Each histogram is divided into 100 linearly spaced bins.

The second set of data attempted to mimic the input configuration of real VCN neurons. Spherical bushy cells receive few AN inputs. AN fibers are connected to spherical bushy cells by endbulbs of Held, which provide extremely strong and reliable synaptic connections. As such, spherical bushy cells take on primary-like response properties which are virtually identical to AN fibers in terms of tuning curves and PSTHs. Rothman *et al.* (1993) showed that endbulbs of Held can be accurately modeled using a single AN suprathreshold input. From a practical standpoint this makes sense in that endbulbs of Held provide approximately 50 very strong synaptic connections to spherical bushy cells which result in an action potential in the spherical cell almost every time an action potential arrives from the AN fibers. Liberman (1991) showed that AN fibers of all SR groups (high, low, medium) project with an equal probability to spherical bushy cells. In our simulations, we used a VCN cell BF of 5kHz. The data in the Liberman (1991) study showed a high spont rate fiber with a CF of 5kHz. We decided to assign a SR of 50 spikes/s second to mimic this case although, based on the data shown, any SR would have been anatomically appropriate.

Unlike spherical cells, globular bushy cells showed preferential contact from high-SR fibers (Liberman, 1991). Therefore, all AN inputs to modeled globular bushy cells were given high SRs of 50 spikes/s. Globular bushy cells receive few AN inputs from AN fibers with similar CFs (Rhode, 2008; Rhode and Smith, 1986). The numbers range from 3 to 4 AN inputs. To model the effects of hearing impaired we require multiple AN fibers with different CFs. As such, we assigned 3 AN inputs to globular bushy cells. We were unable to find a good estimate of the bandwidth (BW) of CFs providing inputs to globular bushy cells. In an attempt to estimate this BW, we used the Greenwood (1990) function which relates the CF of an AN fiber to the position of the hair cell it innervates along the basilar membrane. Knowing that there are approximately 2500 hair cells along the basilar membrane in cats, we assumed that they were linearly distributed along the basilar membrane (Liberman, 1982). Converting these distances to AN fiber CFs, we found that successive AN fibers were separated by approximately 0.0028 octaves. We used this estimate to provide the 3 AN inputs to globular bushy cells with a BW of 0.0056 octaves.

T-stellate cells, like globular bushy cells, receive very few AN inputs over a very small bandwidth (Palmer *et al.*, 2003). Specific estimates range from 3 to 4 AN fibers (Ferragamo *et al.*, 1998). Like globular bushy cells, specific measurements and estimates of input AN fiber BW were unavailable. However, visual comparisons of tuning curves of globular bushy cells and T-stellate cells showed similarly sized regions of excitation (Rhode and Smith, 1986). Therefore, we used similar input characteristics for T-stellate cells as well (BW = 0.0056oct and 3 input AN fibers). Using the results of the Liberman (1993) study, we assign high-SRs to all 3 fibers.

D-stellate cells receive a large number of AN inputs over a wide BW of CFs. We

were unable to find specific mentions of whether or not D-stellate cells were targeted by any fibers of specific SRs. As such, we assigned SRs to the AN fibers using the same physiological distribution discussed in section 3.2.1. Estimates of number of AN inputs to D-stellate cells ranges from 20 to 100 (Pickles, 2008). We chose to use 50 AN inputs for D-stellate cells both because it was approximately in the middle of the estimates and also because Rothman and Manis (2006c) were able to successfully model onset-chopping units with 50 AN fibers using their VCN model. Visual inspection of response maps and tuning curves of D-stellate cells shown in Rhode (2008), Rhode and Smith (1986) and Cai *et al.* (2008) provided us with an estimate of AN input bandwidth of 2 octaves for D-stellate cells. AN CFs were estimated using the Greenwood (1990) function under the assumption that AN fibers were received evenly from hair cells spread linearly along the basilar membrane

Octopus cells, like D-stellate cells, receive a large number of AN inputs over a wide BW of CFs. Liberman (1993) found that they are preferentially contacted by high-SR AN fibers. Octopus cells are estimated to receive inputs from auditory nerve fibers that encode approximately 2 octaves (Oertel *et al.*, 2000). Estimates of number of AN inputs is in the range of 50 to 60 AN fibers per octopus cell. Our simulated octopus cells had 50 AN inputs spread over 2 octaves, similar to the D-stellate cells. AN fibers were given a SR distribution of 70% high-SR fibers, 20% medium-SR fibers and 10% low-SR fibers.

4.2 Healthy Modeled Neurons in the VCN

Historically, VCN cell responses have been defined by their post-stimulus time histograms (PSTHs), as discussed in section 2.2.4.1 and shown in Figure 2.33. VCN cells were simulated with Zilany and Bruce (2007) AN inputs and PSTHs were generated for each VCN cell type. Each simulated VCN cell was provided with 100 repetitions of a 50 ms tone stimulus followed by 50 ms of silence. PSTHs were generated by dividing the stimulus into 0.1 ms bins and calculating the total number of VCN cell action potentials that occurred in each bin over all repetitions of the same stimulus.

VCN cells can also be classified by the regularity of their firing which is quantified by the coefficient of variation (CV) (Young *et al.*, 1988). CV is defined as

$$CV = \frac{\sigma_{R_j}}{\mu_{R_j}} \quad (4.32)$$

where σ_{R_j} is the standard deviation and μ_{R_j} is the mean of ISIs in each bin. Like PSTH plots, CVs are calculated in individual time bins over a stimulus. In this case, a bin size of 1 ms was used. ISIs in each bin are computed and their statistics analyzed. In essence, the CV provides a way of quantifying the variability in the time between successive neuron spikes over a stimulus. A high CV means that there is a

large variability in ISIs. A low CV means that there is very little variability which implies that the cell is firing at an extremely regular rate. Further details on the CV can be found in Young *et al.* (1988) and code of the specific implementation used in these works can be found in Appendix A.2.

Figure 4.3 shows the PSTHs of a simulated spherical bushy cell at 30, 60 and 90 dB SPL. Plots of ISI mean and ISI standard deviation can be seen next to each PSTH. We can see from these plots that our simulated spherical bushy cell shows primary-like behaviours. As the stimulus intensity is increased, the onset spike in the PSTH becomes far more prominent. This is similar to AN responses as well as primary-like VCN neuron responses (Young *et al.*, 1988). Our average calculated CV is approximately 0.55. This indicates that our spherical bushy cell is firing at a highly irregular rate which is consistent with primary-like neurons recorded in the VCN by Young *et al.* (1988).

Next we will look at a simulated globular bushy cell. PSTHs and spike regularity plots can be seen in Figure 4.4. We can clearly see a prominent notch following the onset peak in the PSTH as stimulus intensity is increased. At low stimulus intensities the PSTH matches that of a primary-like neuron. This matches the behaviour shown in measured VCN cells (Young *et al.*, 1988). Looking at our calculated CV value, we see that our simulated cell is firing at a highly irregular rate, but not as irregularly as our simulated primary-like neuron. This is consistent with the findings of Young *et al.* (1988).

The cell simulated in Figure 4.4 received 3 AN inputs from fibers with identical CFs. Figure 4.5 shows PSTHs and spike regularity plots for a globular bushy cell receiving 3 AN inputs with CFs spread over 0.0056 octaves. Looking at Figures 4.5(a) and 4.5(c), there is no discernable difference between a globular bushy cell with a spread of CFs and 3 AN inputs of identical CFs. This is reasonable due to the fact that the AN inputs only span a bandwidth of 0.0056 octaves. The spread of CFs also has no effect on CV calculations. The values of CV shown in Figure 4.5 are virtually identical to those calculated in Figure 4.4.

Octopus cells are characterized by their strong onset responses to a stimulus followed by very low levels of sustained firing activity. They receive a large number of AN inputs over a wide bandwidth. Our simulated octopus cells using the Rothman and Manis (2006c) model show both of those behaviors. Simulated PSTHs and regularity plots can be seen in Figure 4.6. We can see that as the stimulus intensity is raised, the octopus cells onset response becomes extremely prominent from the sustained response. While the calculated values of CV are higher than our simulated primary-like neurons, we can see from the PSTHs that the octopus cells are firing regularly. Another indicator that the octopus cell responses are relatively regular can be seen in the calculated means and standard deviations of ISIs in each bin. At the onset of the stimulus the mean and standard deviations are extremely low implying

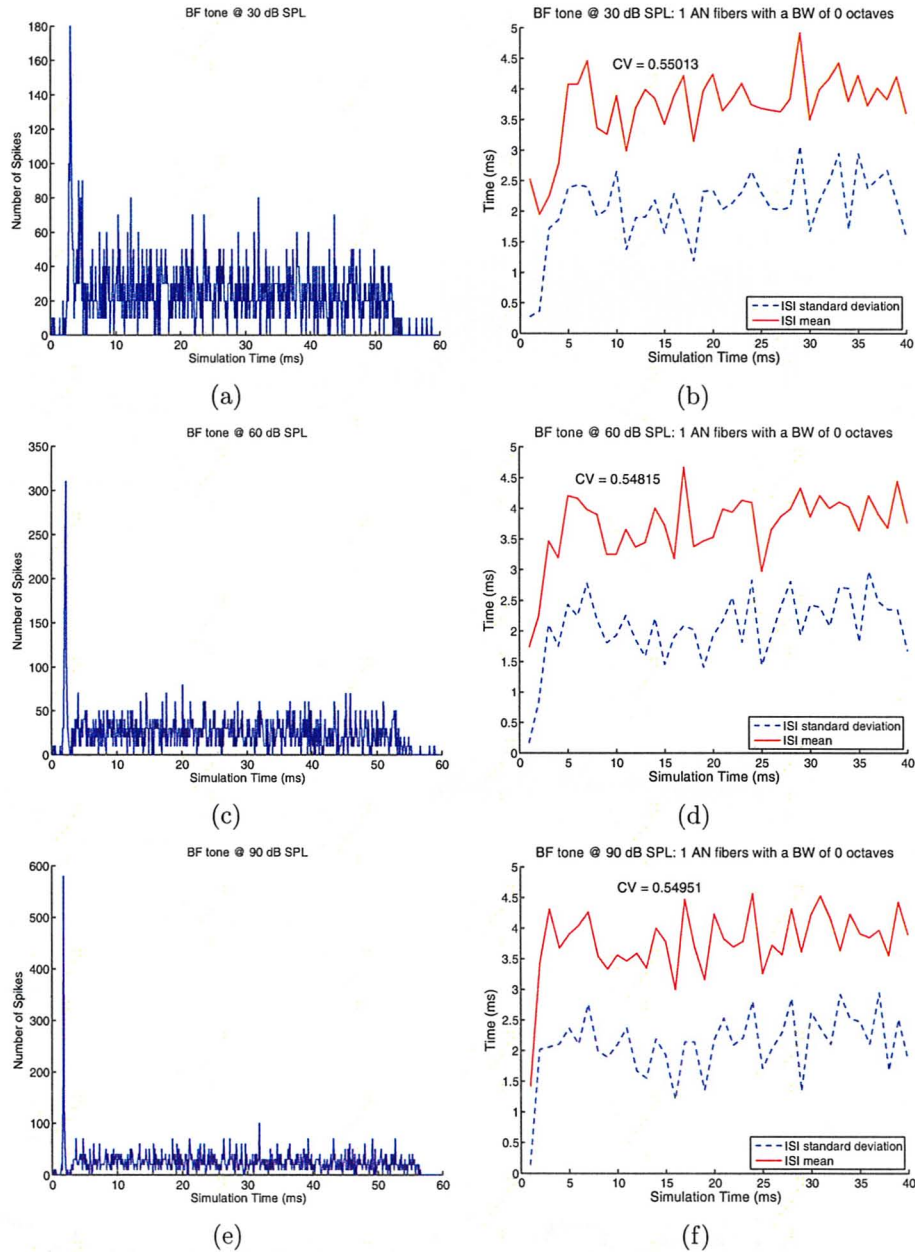


Figure 4.3: PSTHs of a simulated spherical bushy cell are shown in (a), (c) and (e) at stimulus intensities of 30, 60 and 90 dB SPL, respectively. PSTHs are for 100 repetitions of the same stimulus and 0.1 ms bin sizes are used. (b), (d) and (f) show the mean (blue) and standard deviation (red) of ISIs in each 1ms bin. The average CV over the entire stimulus is shown on each regularity figure. Type II VCN model cells were simulated with 1 AN input at BF.

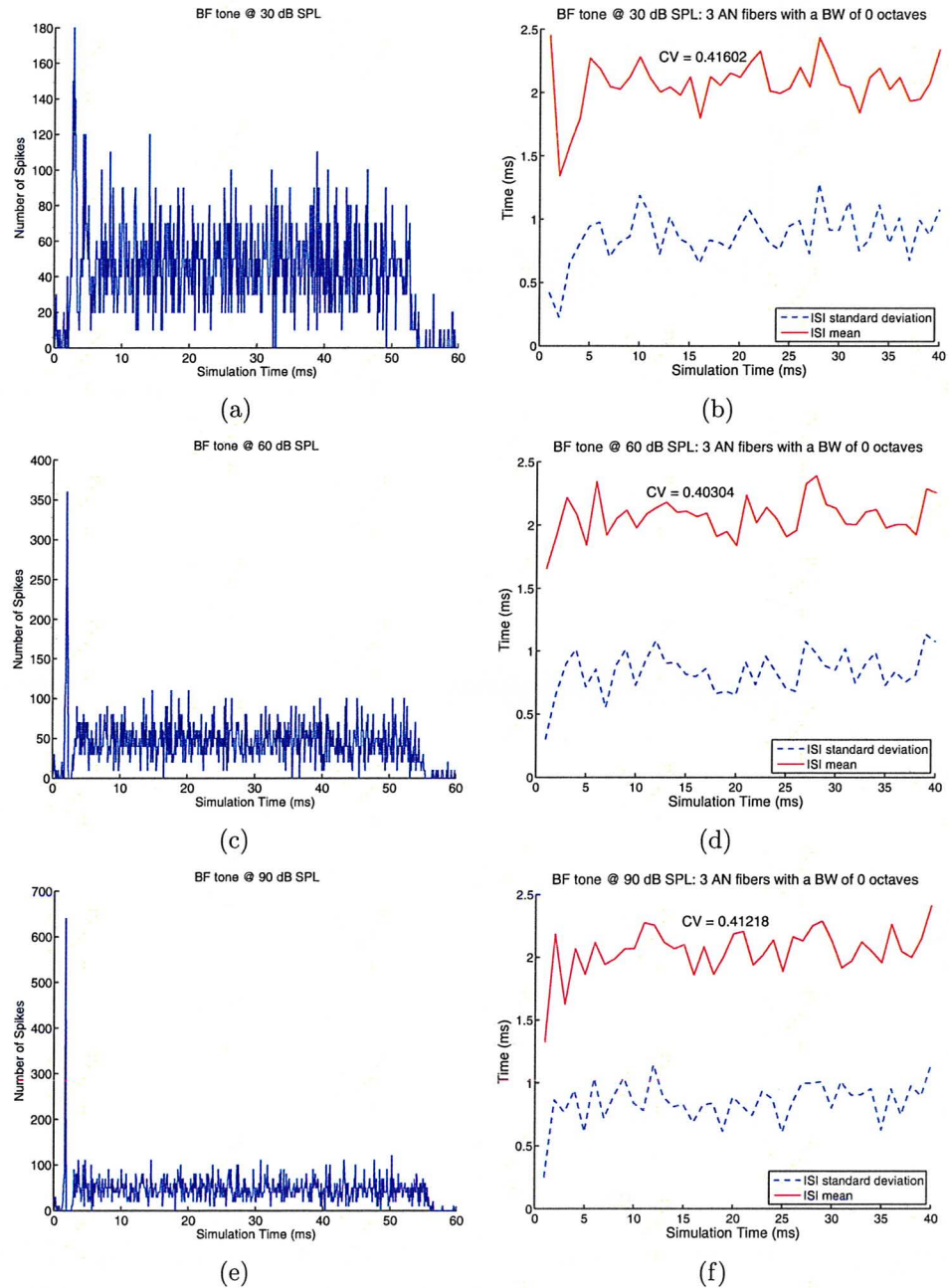


Figure 4.4: PSTHs and regularity plots of a simulated globular bushy cell are shown. Similar to Figure 4.3. The average CV over the entire stimulus is shown on each figure. Type II VCN model cells were simulated using 3 AN inputs with CFs at BF.

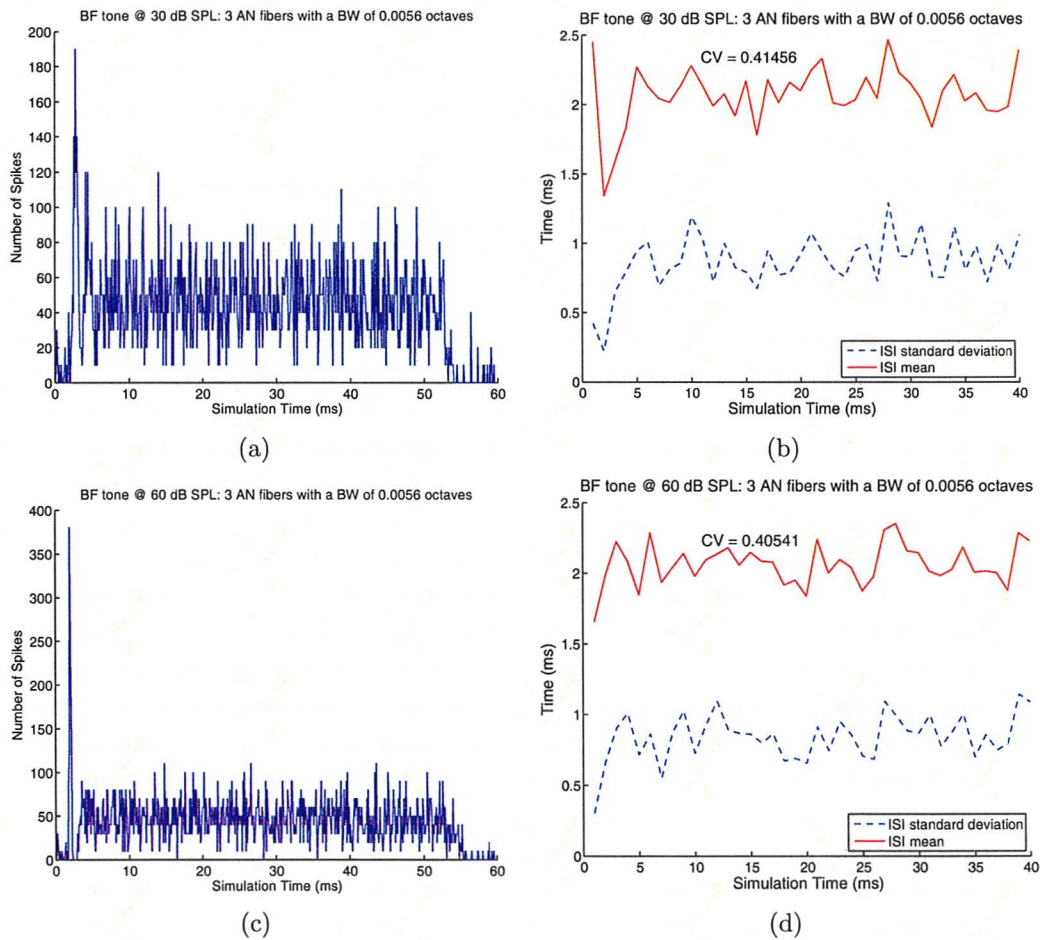


Figure 4.5: PSTHs and regularity plots of a simulated globular bushy cell are shown. Similar to Figure 4.3. Type II VCN model cells are simulated using 3 AN inputs with CFs spread 0.0056 octaves apart centered around 5kHz.

relatively regular firing. However, after the onset spike of the octopus cell, mean ISIs rise to extremely long time periods (tens of milliseconds). These time periods are approximately ten times larger than those of our simulated primary-like neurons. Our stimulus is only 50 ms long. If our average ISI, after the onset spike, is in the tens of milliseconds, that means that the simulated octopus cell only fires approximately once or twice after each onset spike. Clearly, this is a very small sample size of spikes with which to calculate ISI and, as such, it is expected that our calculated CVs would provide erratic results. The results shown in Figure 4.6 are of a cell receiving 50 AN inputs with CFs spread over 2 octaves centered around 5 kHz. Simulated PSTHs and regularity plots of an octopus cell receiving 50 AN fibers with CFs at 5 kHz showed almost identical results and, as such, are not shown here for comparison.

Figure 4.7 shows the PSTHs and regularity plots of a simulated D-stellate cell receiving 50 AN inputs with identical CFs. We can see chopping behavior at the beginning of each PSTH that becomes more prominent with increasing stimulus intensity, similar to chopper cells recorded by Young *et al.* (1988). While chopping behavior is directly visible in the PSTHs, we also notice a relatively high sustained firing rate after the initial chopping response. This is atypical of onset chopper cells. Our calculated CV values at 30 dB SPL is approximately 0.35. This indicates that our onset chopper cell is firing more regularly than our primary-like units, as expected. At higher stimulus intensities however, we notice some discrepancies. We see that there are cases where the standard deviation of the ISI jumps for some bins. This can be attributed, mainly, to the fact that only 100 stimulus repetitions were used in the calculation of CV which makes our regularity data susceptible to sampling noise. If we ignore the large spikes that deviate from the overall trend in each curve we see that, for larger stimulus intensities, the standard deviation of ISIs is comparable (in terms of ms) to primary-like units which contradicts physiological observations.

Though the PSTHs shown in Figure 4.7 did show canonical onset chopping behavior, the simulated AN input configuration did not match physiology. We now examine the effects a spread of CFs has on simulated D-stellate cells by providing our simulated cell with 50 AN inputs with CFs spread over 2 octaves. The results can be seen in Figure 4.8. The PSTHs in Figure 4.8 look very similar to those in Figure 4.7 however, the regularity plots show significant differences. We see that our calculated CV value, is substantially lower than those of simulated primary like units for all stimulus intensities except 90 dB SPL. Apart from some occasional sampling noise, the standard deviation of ISIs in each bin is significantly lower than the mean. This is consistent with results by Young *et al.* (1988). The simulated D-stellate cell is receiving AN fiber inputs from fibers with CFs ranging from 2.5kHz to 10kHz. The fibers with CFs significantly above and below our stimulus frequency of 5kHz are not firing significantly in response to our stimulus which results in the D-stellate cell being driven less, overall. Also, the spread in phase between the responses of

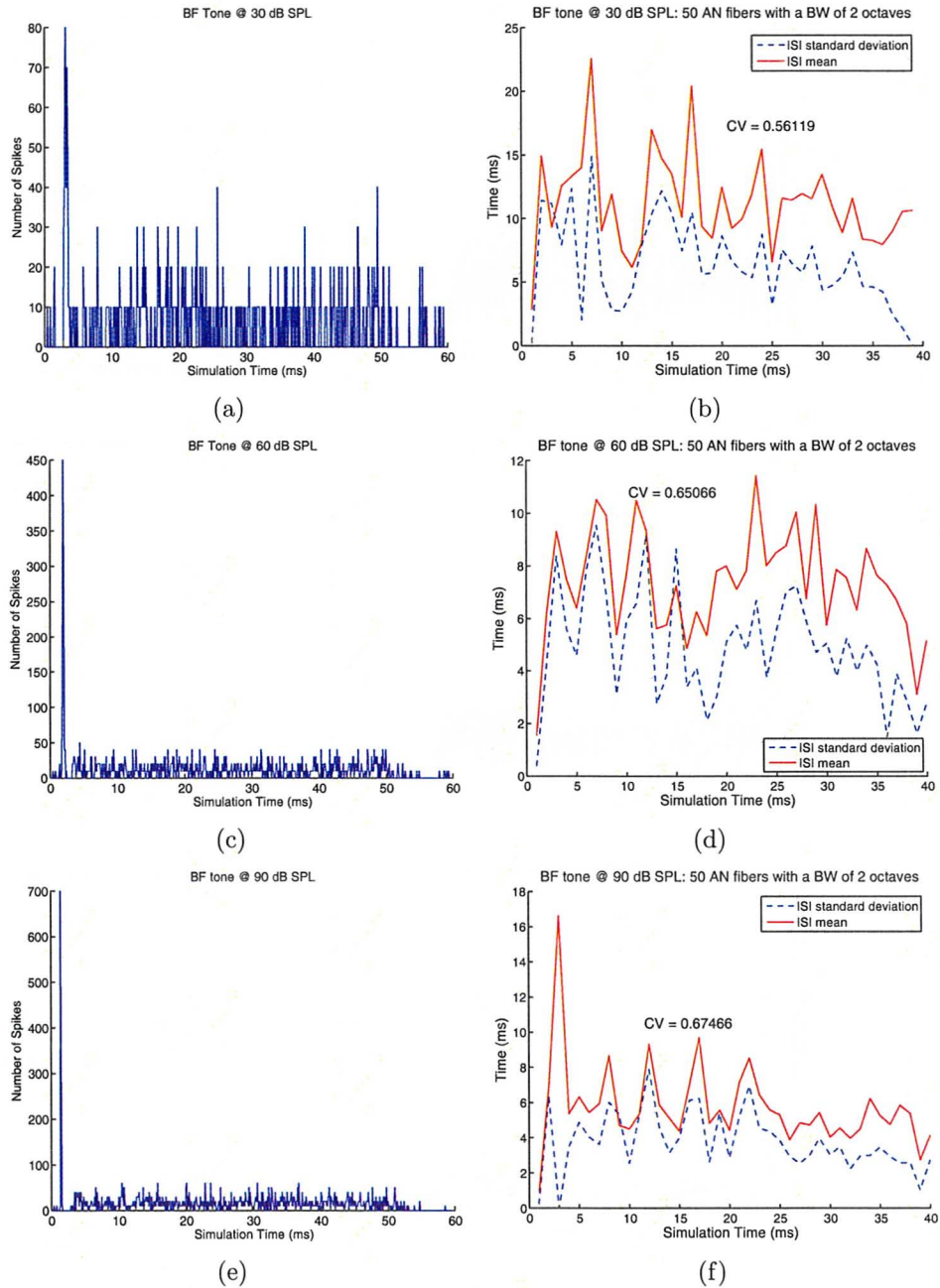


Figure 4.6: PSTHs and regularity plots of a simulated octopus cell are shown. Similar to Figure 4.3. Type II VCN model cell were simulated with 50 AN inputs with CFs spread over 2 octaves centered around BF.

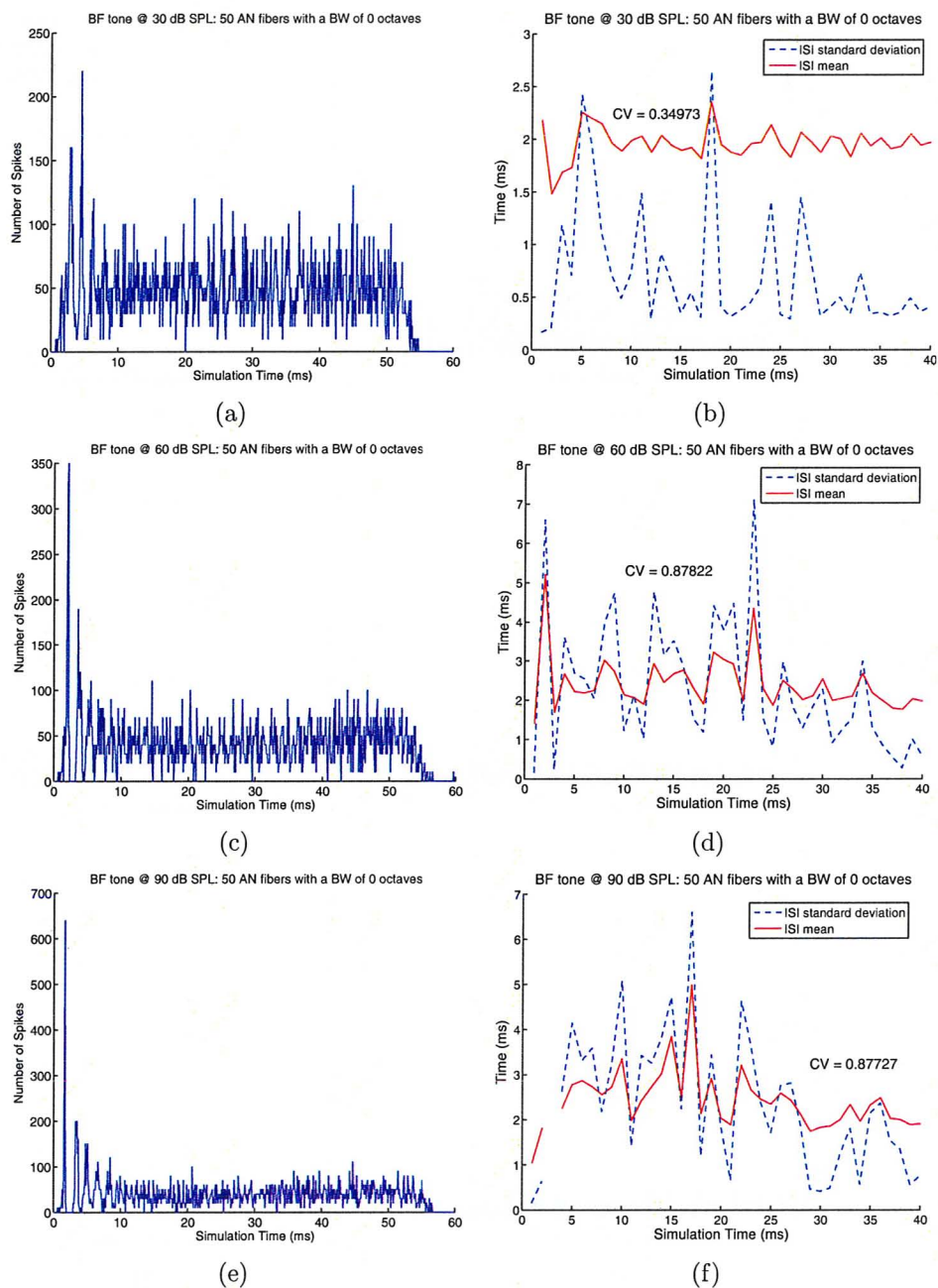


Figure 4.7: PSTHs and regularity plots of a simulated D-stellate cell are shown. Similar to Figure 4.3. Type I VCN cells were simulated with 50 AN inputs having identical CFs (5kHz)

each of the AN fiber inputs decreases the effectiveness of the limited amount of phase locking that occurs in AN fibers with high-frequency CFs. The spikes in standard deviation seen in panel (f) are the result of our small number of stimulus repetitions and are responsible for the large CV value shown. With only 100 stimulus repetitions, we occasionally end up with inaccurate estimates of standard deviation due to the fact that a much larger sample size of data is required for accurate measurements of standard deviation than for calculating the mean.

We saw how the addition of a spread of CFs to a simulated D-stellate cell can result in regularity of firing that is more in line with measured onset chopper cells, however the change in input configuration cannot correct for the relatively high sustained firing rates observed. Rothman and Manis (2006c) developed mathematical models for five different observed cell types but used only the type I-c and type II cell models to simulate VCN cells. While they were able to produce reasonable responses using their AN spike generator, we now see that discrepancies arise when the auditory periphery model is changed. We simulated D-stellate cells using the type I-t cell model outlined by Rothman and Manis (2006c) and found that the net result was a significant decrease in sustained firing. PSTHs and regularity plots can be seen in Figure 4.9. We can also see from the PSTHs that the onset chopping response is more pronounced in D-stellate cells simulated using the type I-t cell model. The main difference between the type I-c and type I-t cell model is the presence of the fast-inactivating K^+ current (I_A) which serves to counteract the depolarizing effects of excitatory synaptic inputs, effectively increasing the threshold of AP generation (Rothman and Manis, 2006c).

Finally, we examine the response properties of a simulated T-stellate cell. We first simulate a T-stellate cell with 3 AN inputs with identical CFs (5kHz). While we expect our T-stellate cell to have a sustained chopper shaped PSTH, we observe in Figure 4.10 that our simulated cell does not exhibit this type of response. In fact, the PSTH looks almost more like that of a primary-like with notch neuron. However, if we examine the regularity data, the calculated CV values are significantly lower than the primary-like neuron shown in Figure 4.4, which indicates that the cell is chopping despite the fact that it is not visible in the PSTH. This is likely the result of the overlapping of several responses that are out of phase in the PSTH. The CV values are also comparable to our simulated onset chopper (D-stellate) cell.

We now simulate a T-stellate cell using 3 AN inputs with CFs spread of a bandwidth of 0.0056 octaves. The PSTH and regularity plots are only shown for a BF stimulus at 60 dB SPL in Figure 4.11. We can see from this figure that the results are virtually identical to the previous case with 3 AN inputs with identical CFs. This is to be expected as the bandwidth of AN inputs is not significantly large enough for differences in phase and AN fiber excitation to present themselves.

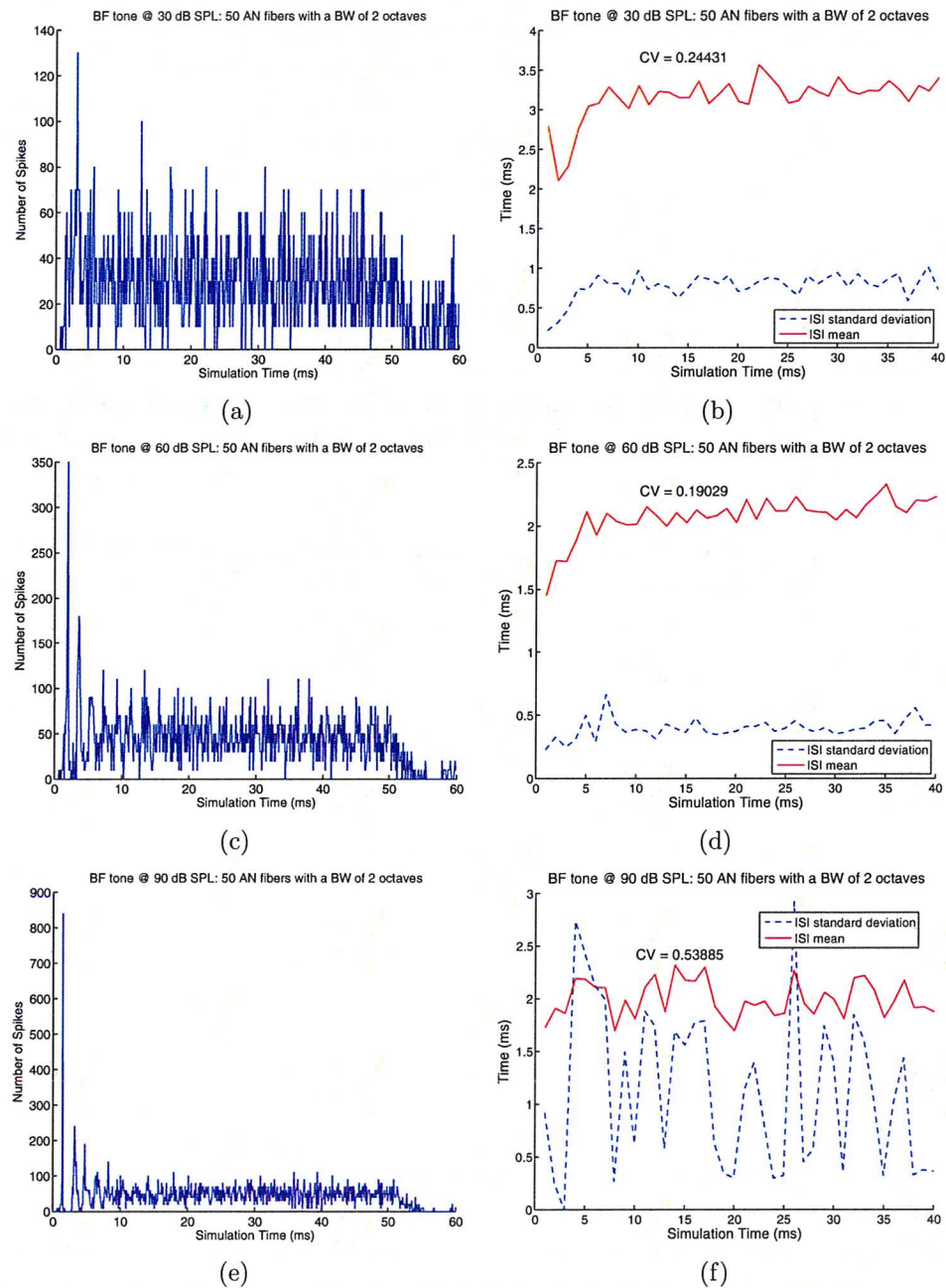


Figure 4.8: PSTHs and regularity plot of a simulated D-stellate cell receiving 50 AN inputs with CFs spread 2 octaves around 5 kHz are shown. Similar to Figure 4.3. Type I VCN model cells were simulated.

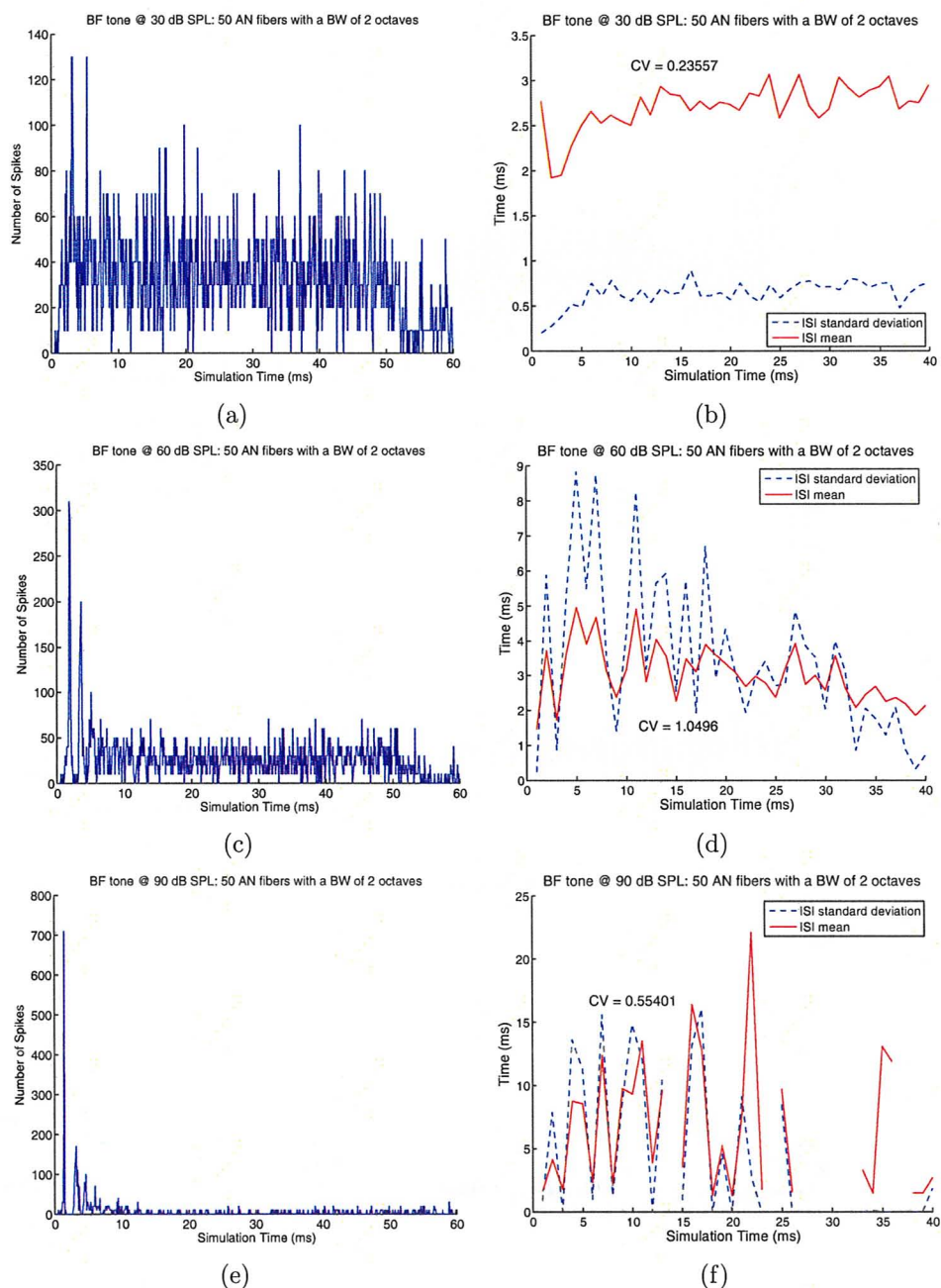


Figure 4.9: PSTHs and regularity plots of a simulated D-stellate cell using the type I-t cell model are shown. Similar to Figure 4.3. The simulated D-stellate cell is receiving 50 AN inputs with CFs spread over 2 octaves centered about BF (5 kHz).

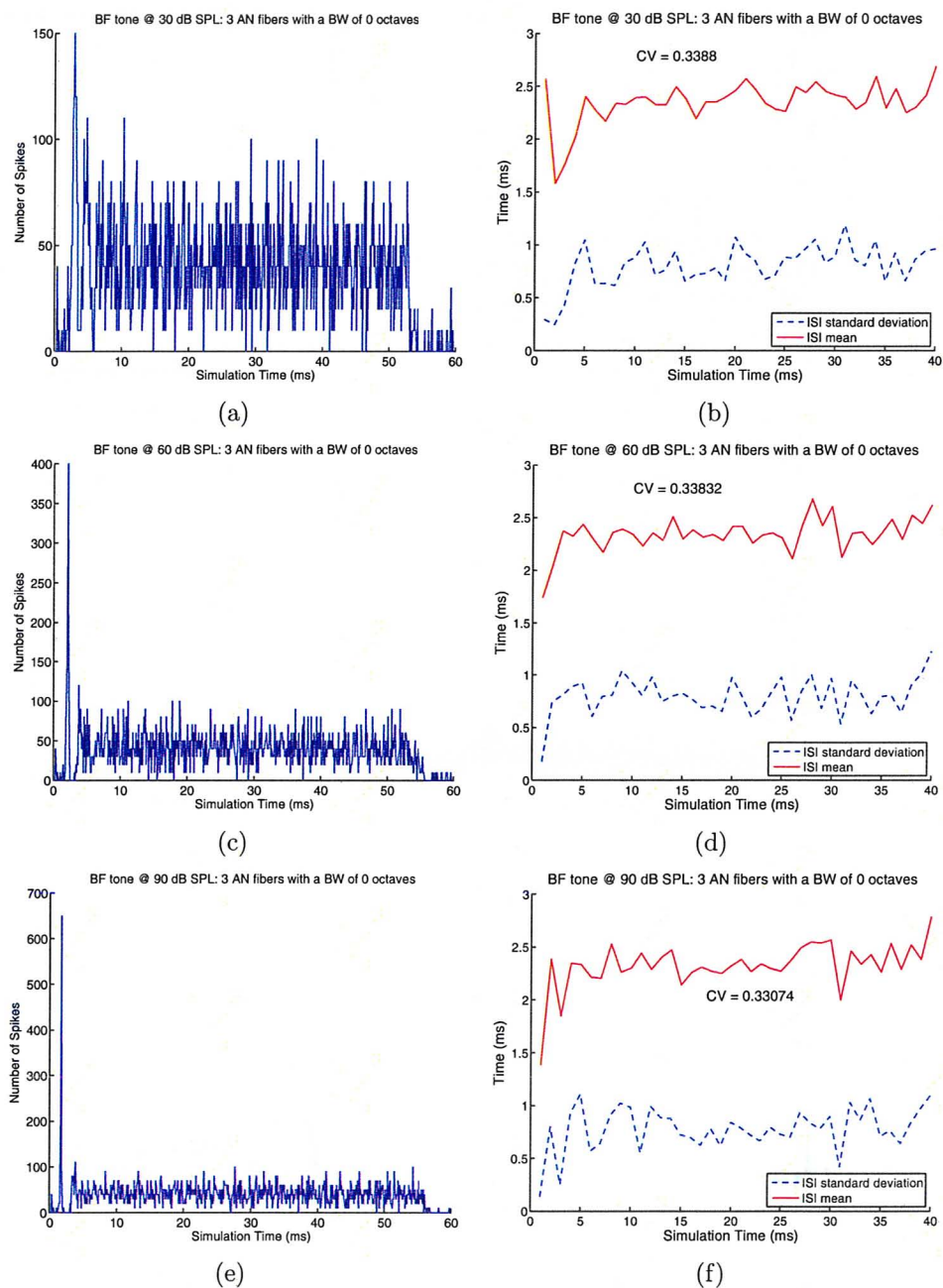


Figure 4.10: PSTHs and regularity plots of a simulated T-stellate cell are shown. Similar to Figure 4.3. Type I VCN model cells were simulated receiving 3 AN inputs with CFs of 5 kHz.

We also simulated a T-stellate cell using the type I-t cell model. While the resulting PSTHs shown in Figure 4.12 are still not identical to canonical sustained chopper responses, we do see some chopping peaks beginning to form. The rate of sustained firing is decreased as a result of the change in cell model, similar to our simulated D-stellate cell. Once again, we can see from our regularity plots in Figure 4.12 that our T-stellate cell is still firing at a relatively regular rate. We can conclude from these results that a currently unmodeled factor is responsible for the resulting PSTH shape seen in recorded sustained chopper cells.

Although VCN cells are often characterized by their PSTHs, not all response properties can be accounted for in that manner alone. For example, the T-stellate cell is characterized by its inhibitory sidebands in addition to its sustained chopper response. Octopus and D-stellate cells receive AN inputs over a broad range of CFs and, as such, have large regions of excitation in addition to their specific PSTH characteristics. For this reason, we will now show and analyze the spread of excitation of each of our simulated VCN cell types. We will do this in the form of iso-intensity curves. Iso-intensity curves show the driven firing rate of a cell in response to a variety of tone frequencies all presented at an identical stimulus intensity. Each plotted line on the curve represents a different stimulus intensity. Each driven rate is a normalized value of the cell firing rate defined by

$$DR = \frac{FR - SR}{FR_{30dB} - SR} \quad (4.33)$$

where FR is the firing rate of the cell in response to the stimulus, SR is the cells spontaneous rate and FR_{30dB} the firing rate of the cell at 30 dB above threshold. FR was computed as the number of spikes occurring in the last 30 ms of the stimulus duration and averaged over all 100 repetitions of the applied stimulus. This method of normalization was selected in order to be able to more directly compare our results to those of Cai *et al.* (2008) when we examine the effects of hearing loss later on.

Figure 4.13 shows an iso-intensity plot for a simulated spherical bushy cell. Note that frequencies are shown as the BF relative to the tone stimulus in octaves. A stimulus 2 octaves above BF will appear in Figure 4.13 as the cell's BF being -2 octaves relative to the tone stimulus. In essence, stimulus frequencies above BF are on the left side of the figure and stimulus frequencies below BF are on the right side of the curve. We can see that the behaviors shown here resemble those of AN fibers closely. At low stimulus intensities the spherical bushy cell is only responsive to an extremely narrow frequency region at the cell's BF. As stimulus intensity is increased the cell becomes more excitable to a wider range of frequencies. At extremely high intensities the cells firing rate is saturated (similar to the AN input) and the cell shows a tail response to large range of stimuli below BF. As the stimulus frequency is increased far enough above BF, we see a sharp decrease in the excitability of the simulated

VCN cell. This coincides with the stimulus frequency exiting the excitable region of the AN tuning curve. These AN-like responses are expected because spherical bushy cells receive very few AN inputs and have extremely strong synaptic connections in the form of endbulbs of Held. The iso-intensity curve for a globular bushy cell is not shown because it is virtually identical to Figure 4.13. Globular bushy cells receive AN inputs from fibers with similar CFs and as such, it is expected that their regions of excitation would be similar to spherical bushy cells. In fact, recorded globular bushy cell iso-intensity curves show similar properties and similar overall response regions to those shown in Figure 4.13 (Rhode, 2008).

We now look at an iso-intensity plot for a simulated D-stellate cell. Figure 4.14 shows an extremely broad range of excitation. The notch in the response at around 4 kHz is a result of resonances in the bulla in the middle ear and is expected. This iso-intensity curve shows a response similar to recorded iso-intensity curves by Rhode and Smith (1986), Palmer *et al.* (2003) and to W-cells simulated by the Zheng and Voigt (2006) DCN model. The only difference is that recorded iso-intensity curves show much steeper decreases in excitation above BF. A recorded D-stellate cell with a similar BF to our simulated cell has a steep decrease in excitation back to spontaneous levels at approximately 8 kHz. This discrepancy is likely due to our estimate of AN input bandwidth of 2 octaves. It is likely that D-stellate cells receive inputs from AN fibers over a much smaller bandwidth than 2 octaves. In fact, recent physiological results and computational studies have shown that the input bandwidth of AN fibers to cells providing wideband inhibition in the DCN may be much smaller than originally estimated (Lomakin and Davis, 2008).

Octopus cells have typically proven difficult to measure intracellularly and, as such, few specifically classified octopus cell iso-intensity curves have been reported (Oertel *et al.*, 2000). PSTHs showing octopus cell-like behavior have been shown next to response maps of unclassified VCN cells (Palmer *et al.*, 2003; Rhode and Smith, 1986). As such, we will compare our octopus cell responses, shown in Figure 4.15, to those results. We can see from our simulated octopus cell iso-intensity curves that their response regions are similar to our D-stellate cells but with a slightly stronger tail response. Similar responses were shown by unclassified cells shown in Palmer *et al.* (2003). Like our simulated D-stellate cell, our simulated octopus cell is more excitable at high frequencies than measured cells. While the estimate of octopus cells receiving input from AN fibers that encode roughly 2 octaves may be correct, it is possible that the spread of CFs is actually smaller than estimated. A more accurate estimate, due to the reasonably prominent tail region in our simulated octopus cells, might be that octopus cells have a greater bandwidth below BF than above. As stated earlier, these conclusions should be taken with a grain of salt due to a lack of published octopus cell data.

This leaves us with the final VCN cell type, the T-stellate cell. Our simulated T-stellate cell iso-intensity curves can be seen in Figure 4.16. We can see from our results that these simulated iso-intensity curves are identical to those shown for primary-like neurons in Figure 4.13. Looking at the results from a purely mathematical perspective, this makes sense. Our simulated T-stellate cell receives an AN input configuration that is similar to our simulated bushy cells. This, however, does not match physiological results. T-stellate cells are characterized by prominent inhibitory sidebands due to the inhibitory inputs they receive from D-stellate cells (Ferragamo *et al.*, 1998). As currently defined, the Rothman and Manis (2006c) model does not account for these inhibitory interconnections of VCN cells and it cannot fully model the response characteristics of T-stellate cells. This result also accounts for the fact that previously simulated T-stellate cell PSTHs did not show canonical forms. We can conclude from this that the Rothman and Manis (2006c) model, in its current state, cannot fully model T-stellate cell behavior and that inter-neuron inhibition must be added in order to allow for more robust and detailed analyses of T-stellate cell behaviors.

One final observation of note is that the AN fiber inputs originally used by Rothman and Manis (2006c) to simulate VCN cell PSTHs produced responses that were most closely matched by Zilany and Bruce (2007) AN fiber inputs modeled at extremely high intensities. While Rothman and Manis (2006c) were able to model some PSTHs that resembled physiological responses, their original AN model is not able to produce the broad range of responses shown in this thesis without significant changes to several model parameters.

4.3 Impaired Modeled Neurons in the VCN

Recently, Cai *et al.* (2008) performed a study of the effects of hearing impairment on the response properties of VCN neurons. The focus of their study was changes in loudness recruitment arising from hearing impairment. They measured a large population of both impaired and unimpaired VCN cells of all types and looked at changes in firing rates, firing thresholds and spreads of excitation. In order to be able to compare our simulated impaired VCN cells as directly as possible to the results presented by Cai *et al.* (2008), we averaged the compound action potential (CAP) audiograms of the unimpaired and impaired ears. The average CAP audiograms were then subtracted to obtain the threshold shift in dB SPL at each frequency which were then used to calculate the appropriate C_{IHC} and C_{OHC} constants for modeling hearing impairment in the auditory periphery.

Cai *et al.* (2008) found that common across all cell types was an overall firing threshold increase. Figure 4.17 shows rate level (RL) curves for the entire population of primary-like neurons. The increase in threshold is clearly evident between impaired

and unimpaired VCN primary-like neurons. Also evident is a diminished saturated driven rate in the overall population. Cai *et al.* (2008) also found that the slope of the RL curve at threshold is steeper in the overall population of unimpaired primary-like cells than in impaired cells.

The chopper cell population showed the exact opposite of the primary-like population. Figure 4.18 shows that the impaired chopper cell population saturates to a higher firing rate than the unimpaired population. Impaired chopper cells also show a steeper slope above threshold than unimpaired chopper cells.

Cai *et al.* (2008) also showed the overall spread of excitation of all recorded VCN cells. Cell's iso-intensity curves were overlapped at BF using a pseudopopulation analysis. Driven firing rates were normalized across each cell type using the method outlined in Equation 4.33. Figure 4.19 shows the plotted iso-intensity curves from Cai *et al.* (2008). Frequencies are plotted as cell BF octaves relative to tone stimulus frequency. We see that the main difference between the two populations is an increase in excitation at frequencies below BF following hearing impairment. The broadening in excitation that occurs as a result of hearing loss is not as large in VCN cells as it is in AN fibers.

We now examine the response properties of simulated VCN cells receiving impaired AN inputs. Figure 4.20 shows the rate level-curves of a simulated primary-like neuron receiving both impaired and unimpaired AN fiber inputs. We can see from the curve that there is a significant increase in threshold for the simulated cell receiving impaired inputs. Unlike the results of Cai *et al.* (2008), our simulated impaired VCN cell did not show a decrease in saturated firing rate at extremely high stimulus intensities. The slope after threshold of our simulated impaired VCN primary-like cell was not substantially shallower than that of our simulated unimpaired cell. Our simulated primary-like with notch VCN neuron produced a response identical to that shown in Figure 4.20. Upon initial reflection, it would seem that there may be some other physiological factors (e.g. plasticity) that are currently unaccounted for in the Rothman and Manis (2006c) model of primary-like neurons in the VCN. It is difficult to draw firm conclusions due to the nature of the data in the study by Cai *et al.* (2008). The animals recorded by Cai *et al.* (2008) were subjected to a narrowband noise signal centered around 2 kHz presented at 111 dB SPL. VCN cells with a large number of BFs were then recorded and then averaged together. Therefore there are some neurons with BFs below the narrowband noise signal and some neurons with BFs above the narrowband noise signal. The location of the BF of the cell is important because it will determine how affected the AN inputs to cell following acoustic trauma. Before any serious conclusions are drawn regarding whether or not there are any currently unaccounted changes in the physiology of VCN cells following acoustic trauma, further simulations of VCN cells at different BFs is required.

Cai *et al.* (2008) grouped onset choppers and sustained choppers together in their

analysis of chopper neuron response properties following acoustic trauma. For our analysis, we shall separately model both onset and sustained chopper cells. Figure 4.21 shows the rate-level curve for simulated onset chopper cells. We see that the impaired onset chopper has a much steeper slope at threshold than the unimpaired onset chopper, as shown by Cai *et al.* (2008). We already showed earlier the Rothman and Manis (2006c) model, as is, cannot properly model the responses of sustained chopper cells due to a lack of inhibitory inputs. It should come as no surprise that our simulated impaired sustained chopper cell (shown in Figure 4.22) does not show either of the characteristics of cells recorded by Cai *et al.* (2008). Like the simulated unimpaired sustained chopper, our impaired cell shows response properties identical to primary-like neurons as currently simulated. We know that T-stellate cells receive inhibitory inputs from D-stellate cells (Ferragamo *et al.*, 1998). If we were to apply a D-stellate cell response as an inhibitory input to the T-stellate cell, as currently modeled, we would see the behavior opposite to that of chopper cells in Cai *et al.* (2008). Our simulated impaired D-stellate cell shows a steeper slope at threshold. This would cause a decrease in the excitability of the T-stellate cell as the D-stellate cell inhibition grows more prominent. This would cause a decrease in the overall firing rate of the T-stellate cell which would, once again, result in primary-like behavior, as described by Cai *et al.* (2008). This is further indication that significant plastic changes occur in the VCN following acoustic trauma.

Figure 4.23 shows the rate level curves of simulated impaired and unimpaired octopus cells. Unfortunately, Cai *et al.* (2008) did not publish any detailed results of cells exhibiting similar responses for us to compare. Cai *et al.* (2008) did mention that cells exhibiting onset type behaviors did exhibit steeper slopes at threshold and saturated at higher rates following sound exposure. We can see that the simulated impaired octopus cell shows a steeper slope at threshold than its unimpaired counterpart. Our simulated impaired octopus cell does saturate to a lower rate at high intensities than the unimpaired octopus cell.

Common across all simulated VCN cells receiving impaired AN inputs is an inability to accurately model all of the rate-level effects of recorded cells in the VCN. All of our simulated cells saturated to identical firing rates at extremely high intensities. While our simulated onset chopper and onset (octopus) cell did show slopes at threshold with similar characteristics to those described in Cai *et al.* (2008), the rest of our simulated cells were unable to reproduce physiological responses. The average rates of firing for both unimpaired and impaired VCN cells were significantly different from those of Cai *et al.* (2008). This fact may imply that there are other physiological factors involved in the function of the VCN that were not previously known.

We now examine the changes in spread of excitation that arise from providing impaired simulated AN inputs to the Rothman and Manis (2006c) VCN model. Figures 4.24, 4.25 and 4.26 show iso-intensity curves for an onset chopper, sustained

chopper and octopus cell receiving simulated impaired AN inputs. The iso-intensity curves for primary-like and primary-like with notch neurons are not shown because they are identical to those shown in Figure 4.25. Both our onset chopper and octopus cell show significant increases in the spread of excitation both above and below BF. The remainder of the cell types show the opposite effect. Simulated Pri, Pri-N and sustained chopper cells all showed a decrease in region of excitation at frequencies above BF as well as a decrease in excitability at frequencies below BF. The unimpaired data shown in Figure 4.19 was averaged over a population of cells with varying types. When performing the averaging, Cai *et al.* (2008) assigned weights to each cell typed based on relative percentage of the population of recorded cells in previous studies. In doing so, Cai *et al.* (2008) assigned the highest weighting to primary-like neurons followed by sustained chopper neurons. These are the two cell types with the narrowest regions of excitation in the VCN. The sustained chopper, in particular, has inhibitory sidebands which would serve to decrease the overall average since the driven rate in those sidebands would be a negative value. While it is difficult to claim, specifically, whether or not each individual simulated response matches its physiological counterpart, we can see behaviors in the individual spreads of excitation of each of our simulated cell types that match some of the overall trends in the physiological data.

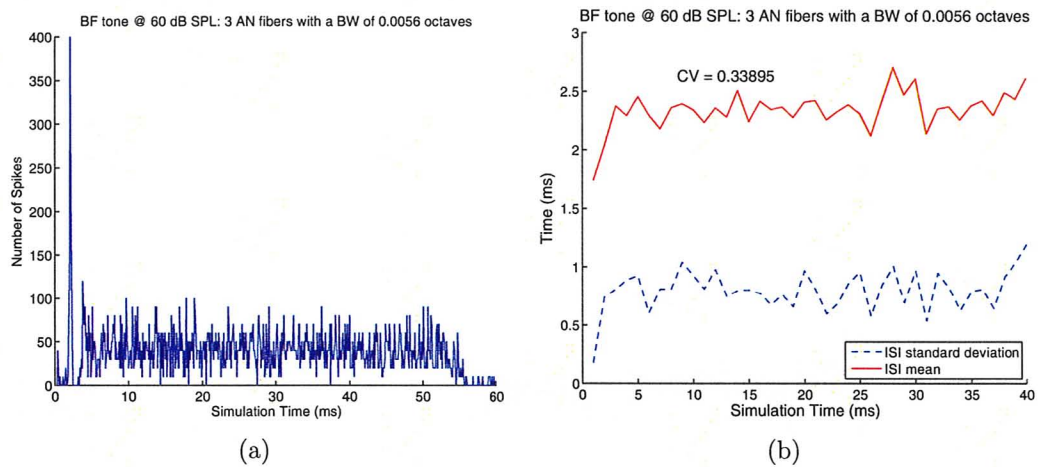


Figure 4.11: The PSTH of a simulated T-stellate cell receiving 3 AN inputs with CFs spread of a bandwidth of 0.0056 octaves is shown in (c) receiving a BF stimulus at 60 dB SPL. 100 repetitions of a BF-tone stimulus were presented and 0.1 ms bin sizes are used. (d) shows the mean (blue) and standard deviation (red) of ISIs in each 1ms bin. The average CV over the entire stimulus is shown on (d). A type I VCN cell model was used.

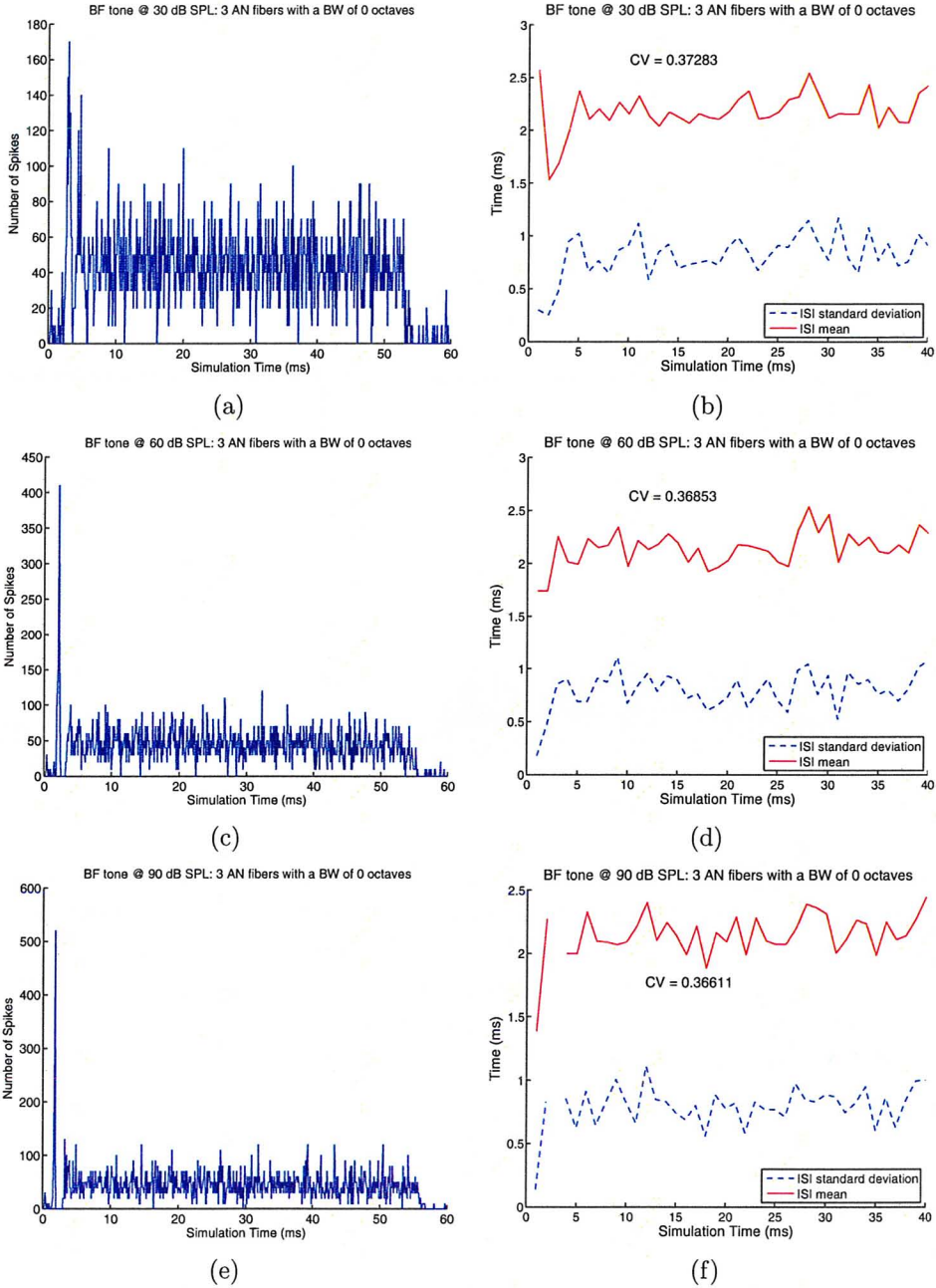


Figure 4.12: PSTHs and regularity plots of a simulated T-stellate cell are shown. Similar to Figure 4.3. T-stellate cells were simulated using the type I-t cell model receiving 3 AN inputs with CFs at 5 kHz.

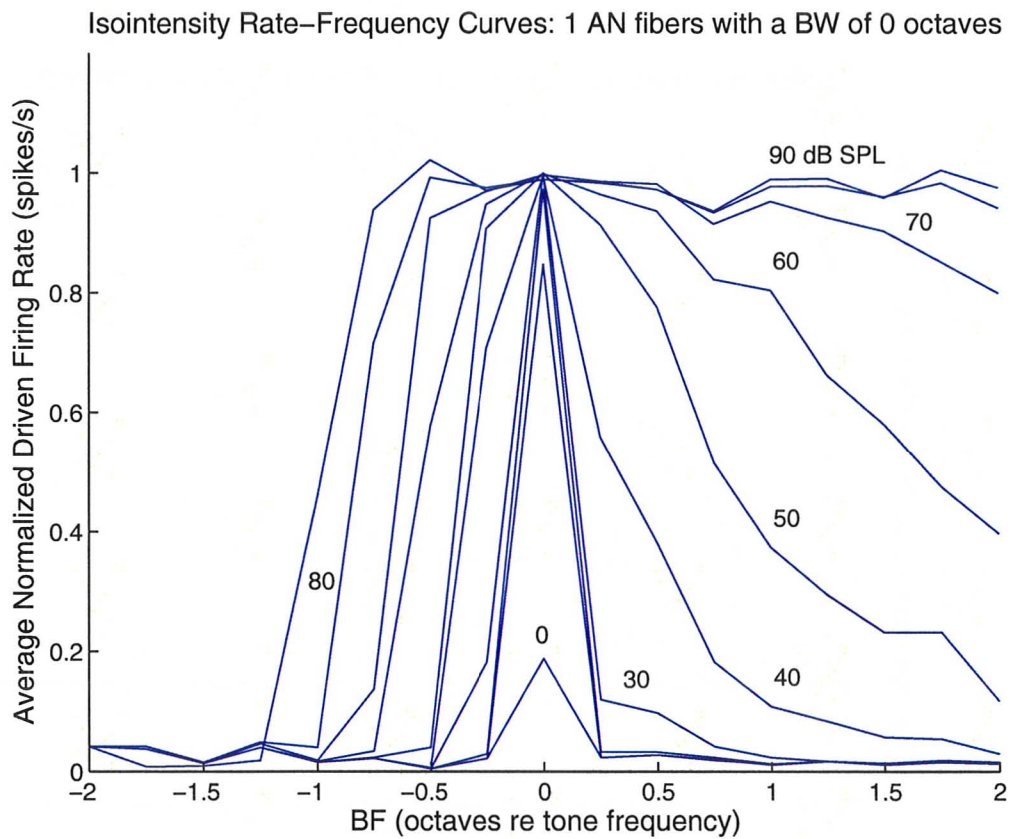


Figure 4.13: Iso-intensity curves of a primary-like neuron. Stimulus intensity is noted next to each curve. Frequencies are shown in BF relative to tonal stimulus (in octaves). Cell was stimulated with 50 ms tonal stimuli from -2 to 2 octaves around BF (5kHz) in 0.25 octave steps.

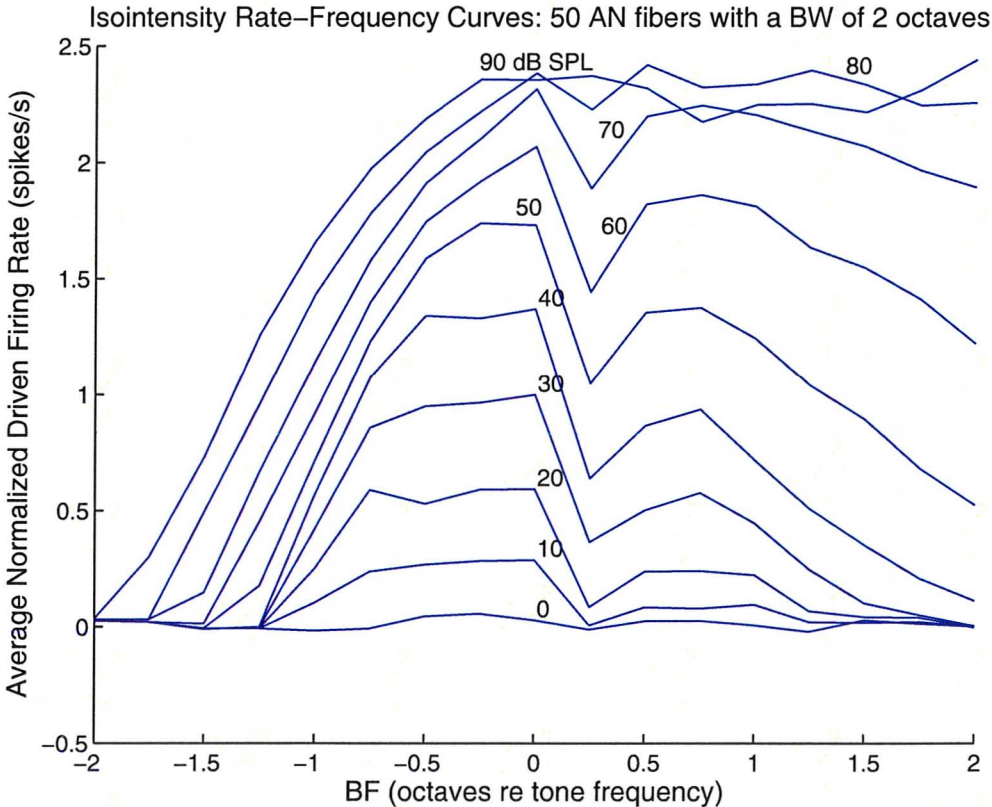


Figure 4.14: Iso-intensity curves of a simulated D-stellate neuron. Similar to Figure 4.13

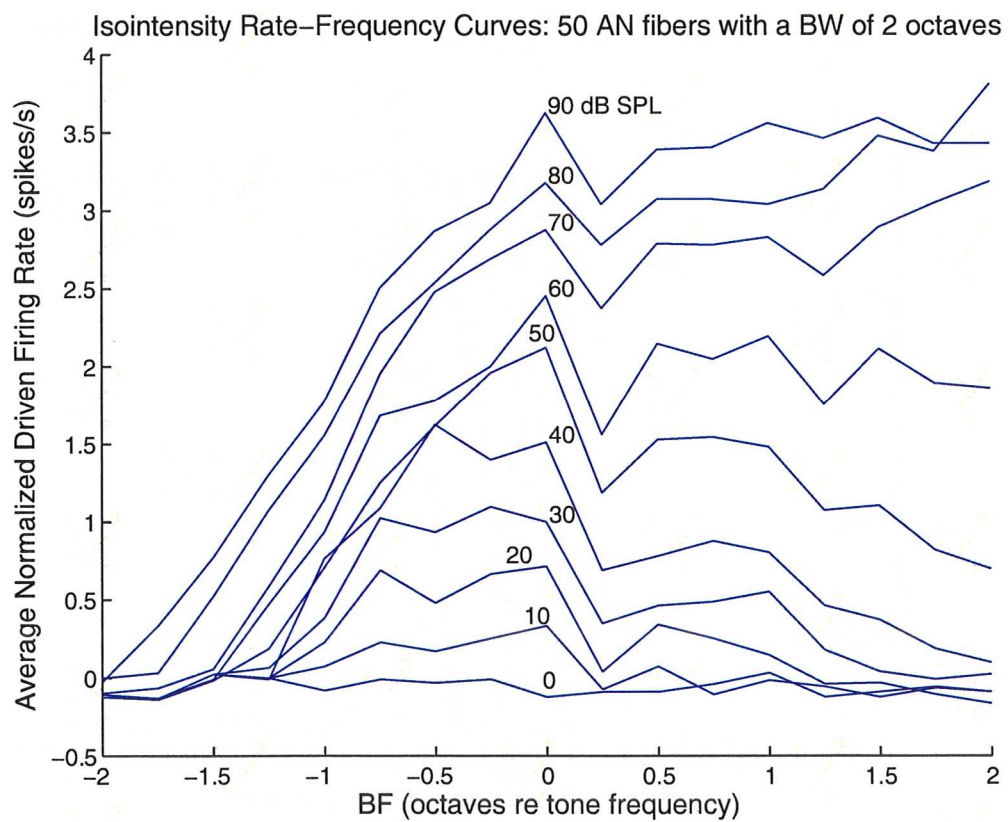


Figure 4.15: Iso-intensity curves of a simulated D-stellate neuron. Similar to Figure 4.13

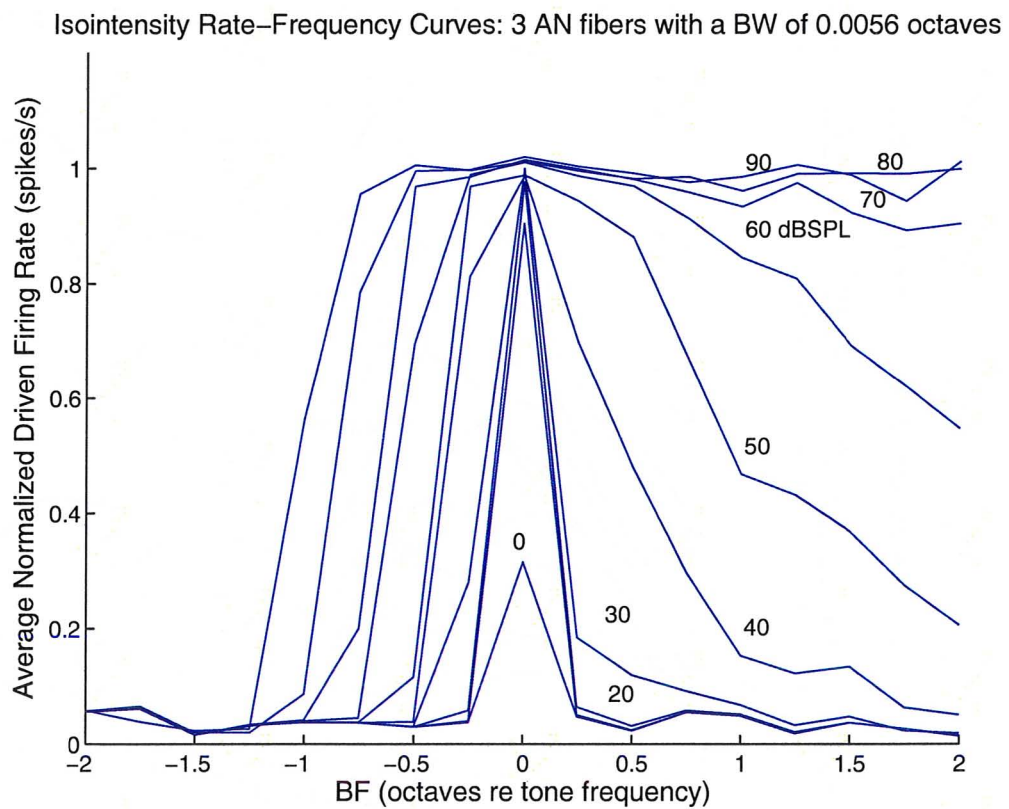


Figure 4.16: Iso-intensity curves of a simulated T-stellate neuron. Similar to Figure 4.13

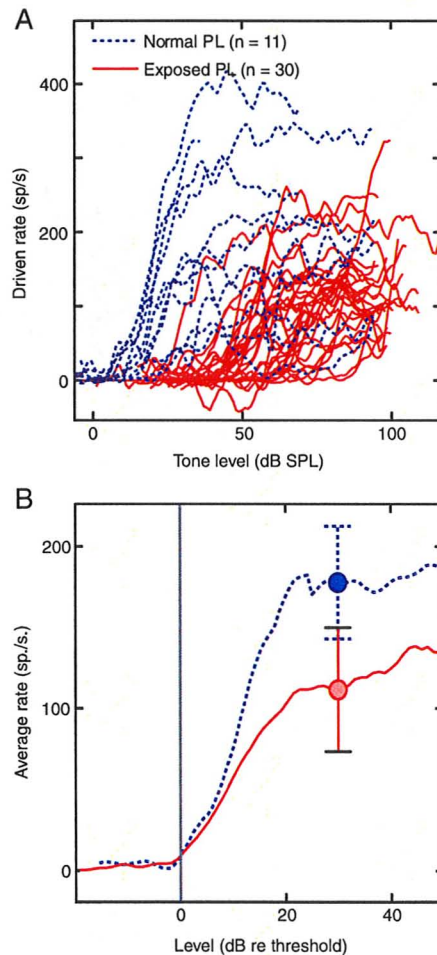


Figure 4.17: Rate-level curves of recorded impaired and unimpaired primary-like VCN cells. (A) shows the rate-level curves of the entire recorded population of primary-like cells recorded by Cai *et al.* (2008) in response to a BF tone. (B) shows the average firing rate of the entire population plotted against dB re threshold. RL curves from (A) were aligned at threshold and averaged. All red curves indicate hearing impaired VCN cells and blue curves indicate unimpaired VCN cells. (Figure 4 reprinted from Cai *et al.* (2008))

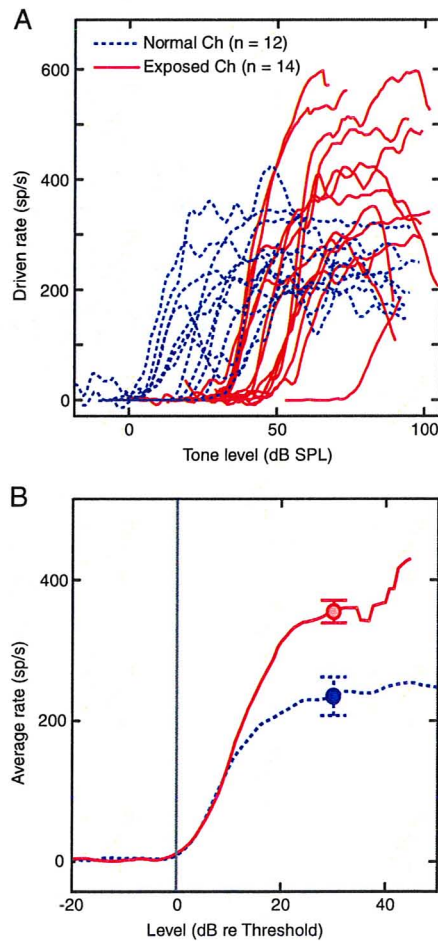


Figure 4.18: Rate-level curves of recorded impaired and unimpaired chopper cells in the VCN. (A) shows the rate-level curves of the entire recorded population of primary-like cells recorded by Cai *et al.* (2008) in response to a BF tone. (B) shows the average firing rate of the entire population plotted against dB re threshold. RL curves from (A) were aligned at threshold and averaged. All red curves indicate hearing impaired VCN cells and blue curves indicate unimpaired VCN cells. (Figure 5 reprinted from Cai *et al.* (2008))

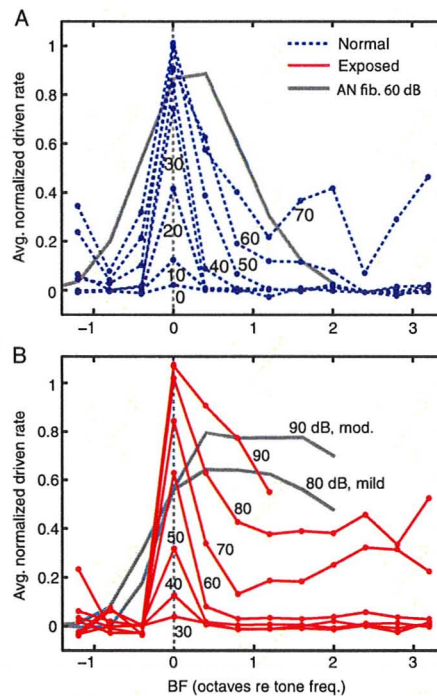


Figure 4.19: Normalized iso-intensity curves for the entire population of recorded VCN cells. (A) shows the spread of excitation of the entire population of unimpaired VCN cells recorded by Cai *et al.* (2008) (blue). The gray line shows the spread of excitation of an AN fiber at 60 dB SPL. (B) shows the spread of excitation of the entire population of impaired VCN cells recorded by Cai *et al.* (2008). The grey lines shows the spread of excitation of two impaired AN fibers. (Figure 6 reprinted from Cai *et al.* (2008))

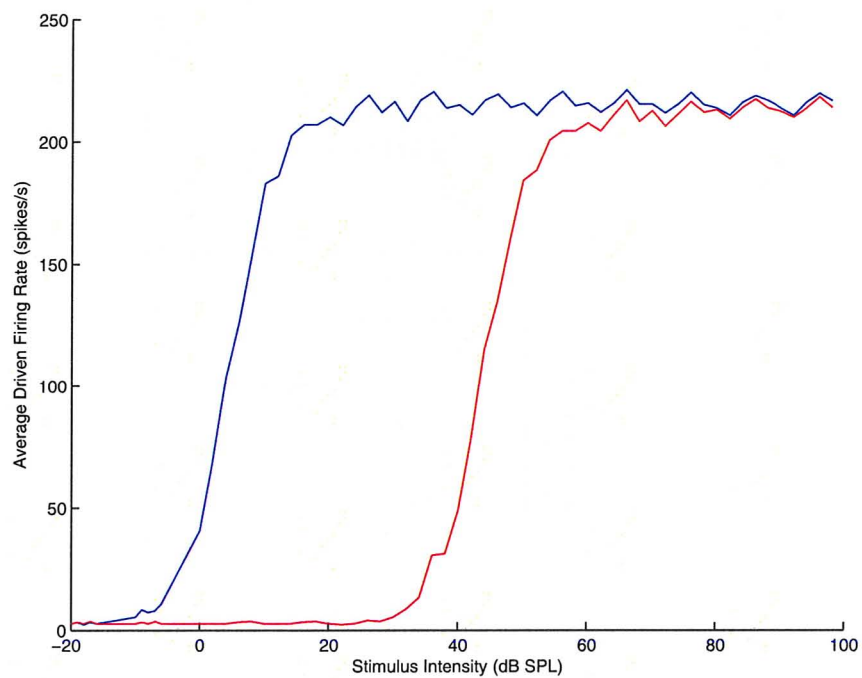


Figure 4.20: Rate-level curves of simulated impaired and unimpaired primary-like VCN neurons. Driven rate (firing rate minus SR) is plotted versus stimulus intensity. The blue curve indicates the unimpaired neuron and the red curve indicates the impaired neuron. Each neuron is presented with 100 repetitions of a 50 ms BF (5 kHz) tone. Firing rates are computed as the average of the firing rate over the last 30 ms of the stimulus over all 100 trials.

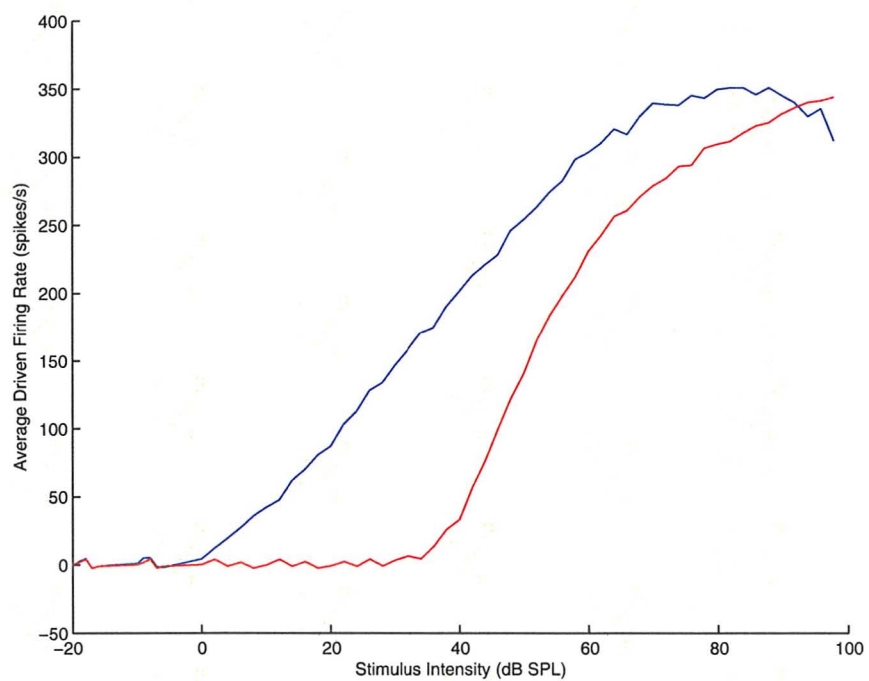


Figure 4.21: Rate-level curves of simulated impaired and unimpaired onset chopper neurons. Similar to Figure 4.20

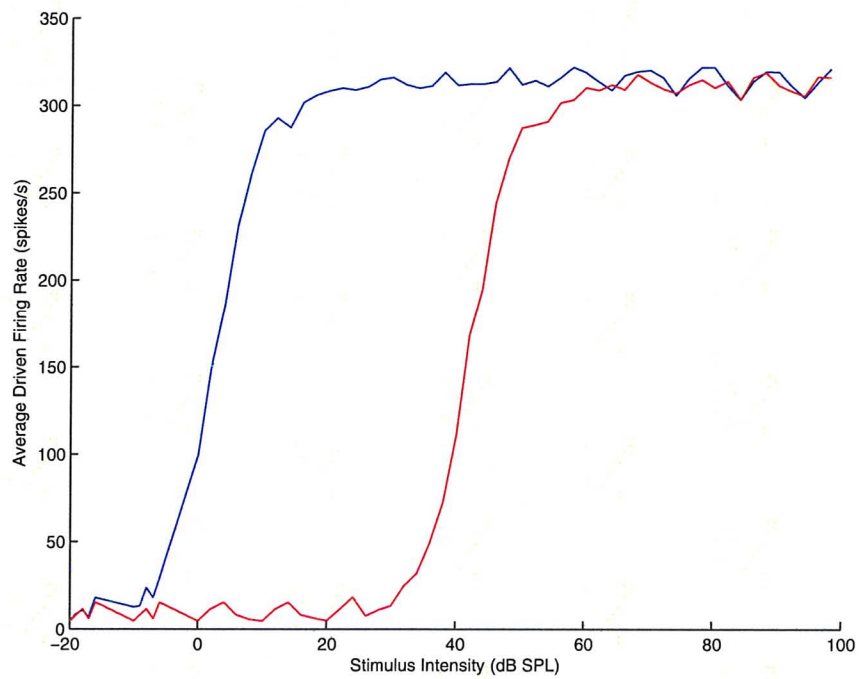


Figure 4.22: Rate-level curves of simulated impaired and unimpaired sustained chopper neurons. Similar to Figure 4.20

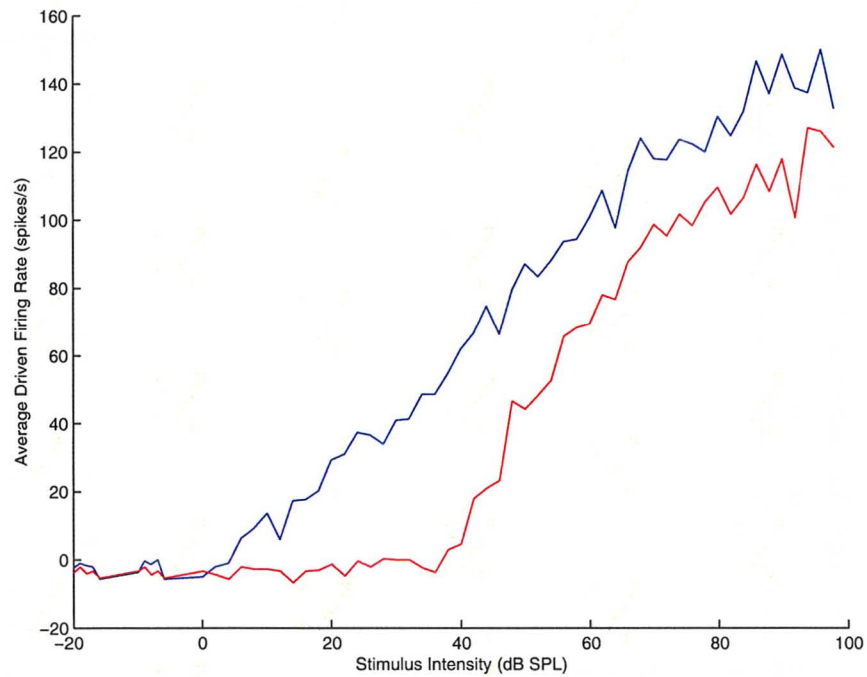


Figure 4.23: Rate-level curves of simulated impaired and unimpaired octopus cells. Similar to Figure 4.20

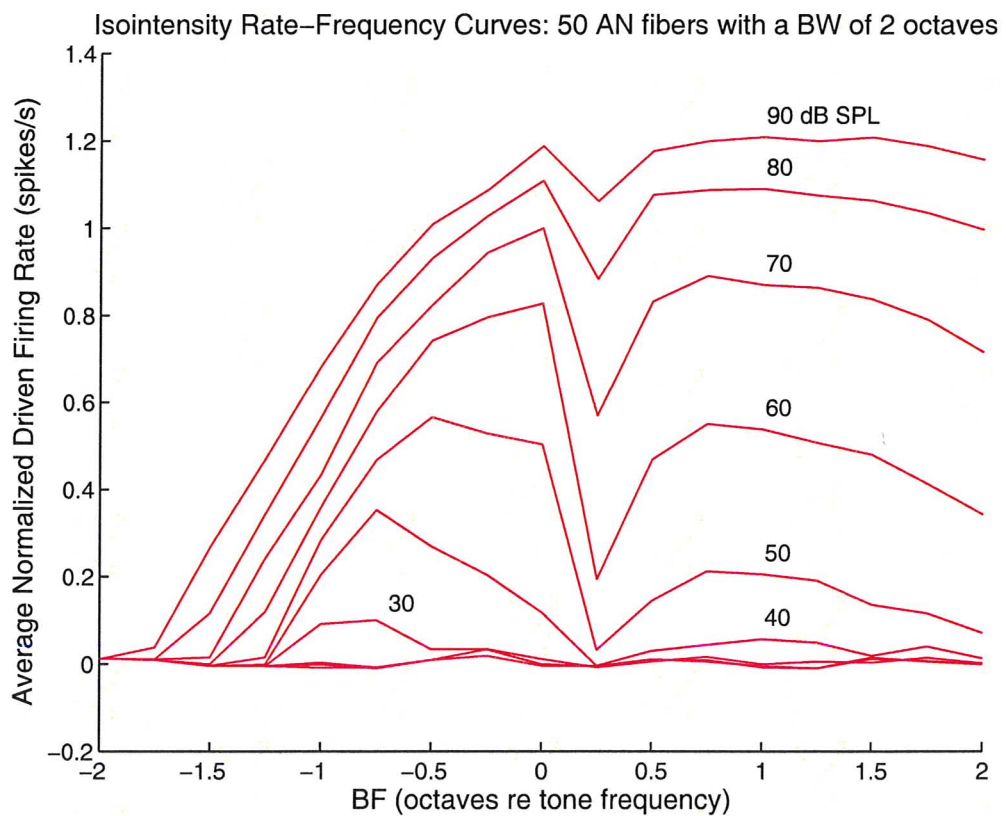


Figure 4.24: Iso-intensity curves of a simulated onset chopper cell receiving impaired AN inputs. Similar to Figure 4.13.

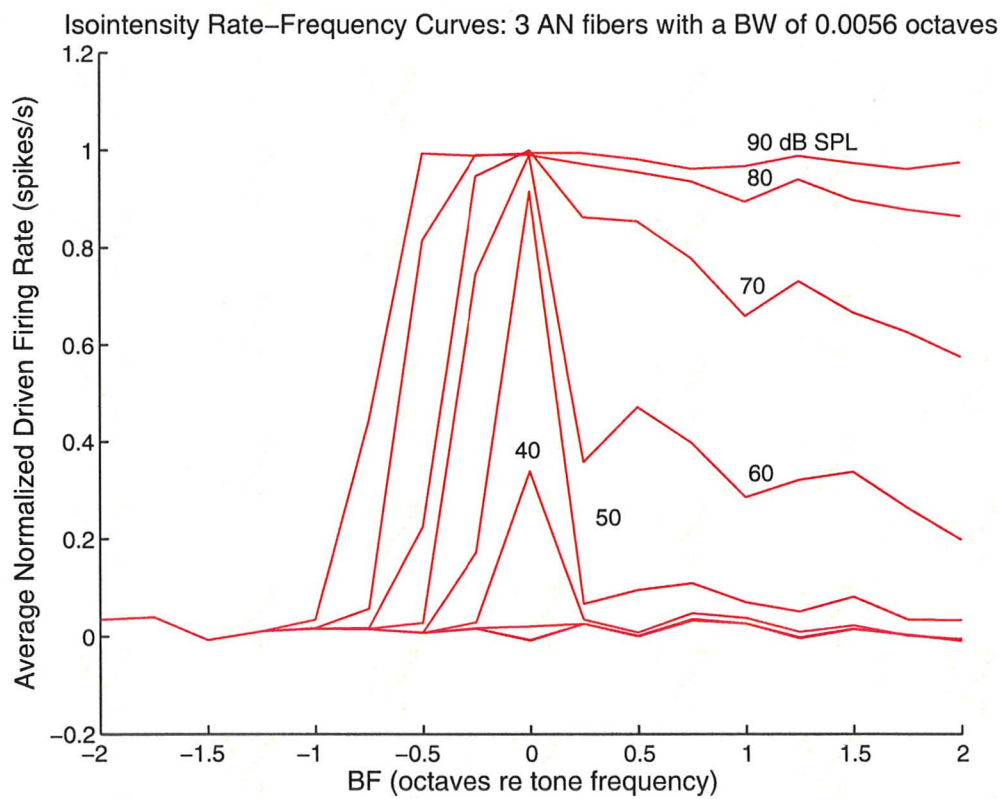


Figure 4.25: Iso-intensity curves of a simulated simulated chopper cell receiving impaired AN inputs. Similar to Figure 4.13.

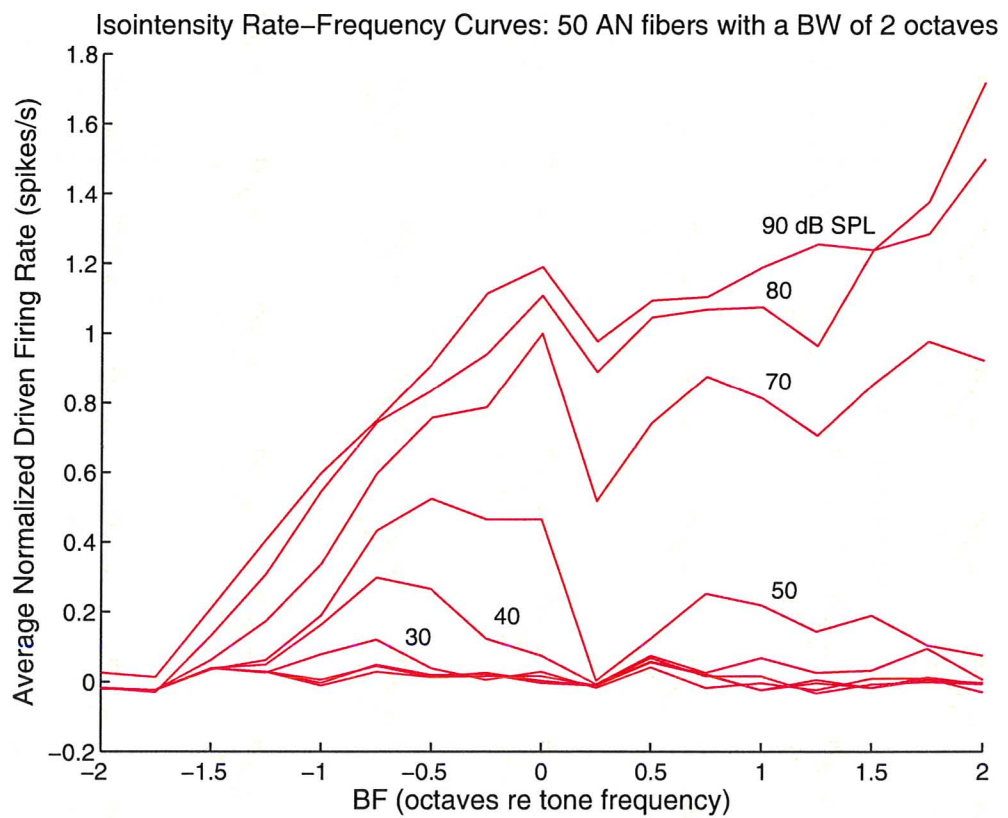


Figure 4.26: Iso-intensity curves of a simulated onset cell receiving impaired AN inputs. Similar to Figure 4.13.

Chapter 5

Conclusions & Future Works

5.1 Conclusions

The Zheng and Voigt (2006) model of neurons in the DCN was provided with AN inputs from the Zilany and Bruce (2007) model of the auditory periphery. The resulting DCN cell responses were drastically different from those originally published by Zheng and Voigt (2006). DCN cells modeled using Zilany and Bruce (2007) model AN inputs showed decreases in firing thresholds, significant widening of their responses and overall increases in excitatory behavior. In order to find the source of the differences, AN responses from the Carney (1993) model, originally used by Zheng and Voigt (2006), were compared to those generated by the Zilany and Bruce (2007) model. It was found that AN fibers modeled using the Carney (1993) model showed less broadening in their responses, saturated to higher firing rates and had significantly higher firing thresholds. It was shown that some of the differences in responses could be accounted for by changes in the connection parameters of the Zheng and Voigt (2006) model. A series of simulations were undertaken to determine the ideal parameter sets for generating the most physiological type III, type IV and type IV-T responses possible. Though responses that reasonably matched physiology were simulated, it was found that further modeling of the non-specific afferents providing inputs to DCN primary cells is required to account for the low firing thresholds and wide responses.

AN fibers modeling IHC and OHC impairment in the cochlea were simulated using the Zilany and Bruce (2007) and used in conjunction with the Zheng and Voigt (2006) DCN model to explore the effects that hearing impairment in the auditory periphery has on DCN cell responses. Type III, type IV and type IV-T primary cells were modeled using the ideal parameter set receiving impaired AN inputs with CAP threshold shifts well above, well below and just above BF. Results were compared to recent physiological measurements of DCN cell responses following acoustic trauma by Ma and Young (2006). Type III cells receiving impaired AN inputs with CAP

threshold shifts just above BF showed class A tail responses. Type IV and type IV-T primary cell receiving similar AN inputs showed class B tail responses. DCN cells with CAP threshold shifts well above threshold showed no noticeable changes in response. Primary cells receiving impaired AN inputs with CAP threshold shifts well below BF showed very minor activity overall. Type IV-T primary cells receiving impaired AN inputs with CAP threshold shifts well below BF show class B-like tail distributions.

Zilany and Bruce (2007) model AN inputs were also provided to the Rothman and Manis (2006c) VCN cells model. PSTH and regularity responses of all VCN cell types were modeled. It was shown that the Rothman and Manis (2006c) model was able to reproduce a wide array of physiological responses to a variety of stimuli for simulated bushy cells, octopus cells and D-stellate cells. Though regularity analysis showed chopper-like behavior, simulated T-stellate cells were not able accurately reproduce physiological responses. T-stellate cell PSTHs did not visually exhibit clear chopping behavior and plots of spreads of excitation showed a lack of the prominent sideband inhibition typically that characterizes their responses. It was determined that this was due to the lack of modeled D-stellate cell inhibition reported by Ferragamo *et al.* (1998). An attempt was made to provide physiological AN input configurations to modeled Rothman and Manis (2006c) VCN cells. The estimate of a 2 octave spread of AN fiber CFs was shown to be excessive when examining the spread of excitation in modeled octopus and D-stellate cells. A spread of CFs did show more accurate physiological response properties in D-stellate cells. Modeled onset and sustained chopper units showed high sustained rates of firing. It was shown that sustained firing rates could be limited by changing to a Rothman and Manis (2006b) type I-t cell. The I_A current present in the type I-t cell model served to lower the sustained firing rate.

Rothman and Manis (2006c) VCN cells were also modeled receiving impaired AN fiber inputs from the Zilany and Bruce (2007) model in order to compare the responses to physiological recording by Cai *et al.* (2008). Resulting simulated VCN cell responses did not match reported results by Cai *et al.* (2008). While, D-stellate cells did show steeper slopes at threshold following acoustic trauma, they did not show the higher saturated firing rates at high intensities typical of recorded hearing impaired VCN chopper neurons. Modeled primary-like neurons did not show the decrease in slope at threshold for their rate-level responses, nor did they show a decrease in sustained firing rate. These results lead us to suggest that the changes in VCN cell responses following acoustic trauma, reported by Cai *et al.* (2008), are mainly the result of plastic changes in VCN neurons and not of changes in AN fiber responses.

5.2 Suggestions for Future Works

The results of our DCN cell simulations suggest that the input provided to DCN principal cells by efferents from higher stages of the auditory system as well as afferents within the DCN play a role in increasing the frequency contrast of DCN cell responses. A further study of simulated DCN cell responses with the addition of the non-specific afferents described by Zheng and Voigt (2006) could serve to confirm hypothesis. The minor change to the Zheng and Voigt (2006) model would be to model the non-specific afferents as inhibitory as opposed to excitatory as an excitatory input would actually make the responses worse. Zheng and Voigt (2006) currently model these inputs as a renewal process with constant firing rate. It is highly unlikely that so simplistic a model is accurate and it would prove valuable to attempt to develop a physiologically based model of these afferents.

The Zheng and Voigt (2006) model assigns synaptic weights uniformly to all synaptic inputs regardless of the target cell's BF relative to the synaptic input. Lomakin and Davis (2008) recently performed a study of wideband inhibitors where they assigned synaptic weights using a Gaussian distribution such that synaptic inputs nearest to BF received the strongest synaptic connections. Such a model of synaptic inputs could also serve to accommodate for the wider responses exhibited by DCN cells simulated using Zilany and Bruce (2007) model AN inputs.

Modeled T-stellate cells using Zilany and Bruce (2007) AN inputs were unable to reproduce physiological response properties due to a lack of the inhibition provided by D-stellate cells. The addition of an inhibitory synaptic current to the Rothman and Manis (2006c) current model could reproduce the inhibitory sidebands typically shown by T-stellate cell responses. The ability to model all five VCN cell types in response to wide variety of stimuli would then allow us to attempt to model the next stage of the auditory system, the SOC.

Cai *et al.* (2008) presented their results for a population of VCN cells of various types and over a range of BFs. Our hearing impairment study only examined the responses of one cell of each type with a BF of 5 kHz. A further modeling study of a population of VCN cells, mirroring that in Cai *et al.* (2008), could be undertaken to further solidify our hypothesis that the effects of hearing loss on VCN cell responses is primarily the result of plastic changes in the VCN and not of changes in AN input responses due to hair cell loss.

Appendix A

MATLAB code and ideal DCN model parameters

Appendix A.1 contains the MATLAB code for the implementation of the Rothman and Manis (2006c) VCN model used in these works. Appendix A.2 contains the MATLAB scripts used to calculate CV and Appendix A.3 contains the MATLAB script used to generate AN inputs to the Zheng and Voigt (2006) DCN model. Most importantly, the DCN model connection parameters used to generate physiological responses to Zilany and Bruce (2007) model AN inputs can be found in Appendix A.4.

A.1 VCN Model Code

The MATLAB code used to simulate Rothman and Manis (2006c) model VCN cells can be found here. The main script of the model is `VCN_v9.m`. `VCN_RK4solv_main_v2.m` is the main function of the implemented ODE solver. The rest of the scripts are sub-routines for the ODE solver. Further details can be found in the comments at the start of each script.

A.1.1 `VCN_v9.m`

```
function V = VCN_v9(suborsup, celltype, spikeat, Spike_times)
% This function computes the transmembrane potential of a VCN cell
% receiving AN fiber inputs. Data is generated using
% VCN_RLinputgen.m.
%
% spikeat: defines the bin size in ms of the spike train vector
%
```

```

% Spike_times: a spike train vector
%
% suborsup: defines AN inputs as either suprathreshold or subthreshold.
%
% celltype: allows the user to select the type of VCN cell simulated. The
% input variable is an integer corresponding to the cell type.
%
% VCN Cell type | celltype value
% I-c           | 1
% I-t           | 2
% I-II          | 3
% II-I         | 4
% II           | 5

% VCN Model
% Prepared by: Stephen Vetsis

% Simulation parameters
dt = 0.001; % simulation time step in ms
simtime = 50*1.2;
Vinit = -63.9;

% Model Parameters
global Cm; % Membrane capacitance in pF
global Vth; % Threshold potential in mV
% Sodium Current Parameters
global gNa_max; % Sodium current peak conductance in nS
global VNa; % Sodium current reversal potential in mV
% Hyperpolarization-activated cation current parameters
global gh_max; % Ih current peak conductance in nS
global Vh; % h current reversal potential in mV
% Model leakage current
global glk_max; % Leakage current max conductance in nS
global Vlk; % Leakage current reversal potential in mV
% Model excitatory post-synaptic current
global tauE; % Excitatory synaptic current time constant in ms
global gE_theta; % Synaptic efficacy of synaptic inputs in nS
global VE; % IE reversal potential in mV
% IA: Fast transient K current
global Vk; % Fast transient K current reversal potential in mV
global gA_max; % Fast transient K current maximum conductance in nS
% Ilt: Low-threshold K current
global gLT_max; % Low-threshold K current maximum conductance in nS
global zeta; % gating particle dynamics constant
% High-threshold K current
global gHT_max; % High-threshold K current maximum conductance in nS

```

```
global fi; % constant for High-threshold K current activation particles

% set parameters according to cell type
if celltype == 1
    Vrest = -63.9;
    Cm = 12.0;
    Vth = -38.3;
    gNa_max = 1000.0;
    VNa = 55.0;
    gh_max = 0.5;
    Vh = -43.0;
    glk_max = 2.0;
    Vlk = -65.0;
    tauE = 0.07;
    gE_theta = 11.0;
    % gE_theta = 2.0;
    VE = 0.0;
    Vk = -70.0;
    gA_max = 0.0;
    gLT_max = 0.0;
    zeta = 0.5;
    gHT_max = 150.0;
    fi = 0.85;
elseif celltype == 2
    Vrest = -64.2;
    Cm = 12.0;
    Vth = -34.9;
    gNa_max = 1000.0;
    VNa = 55.0;
    gh_max = 0.5;
    Vh = -43.0;
    glk_max = 2.0;
    Vlk = -65.0;
    tauE = 0.07;
    gE_theta = 12.0;
    % gE_theta = 2.2;
    VE = 0.0;
    Vk = -70.0;
    gA_max = 65.0;
    gLT_max = 0.0;
    zeta = 0.5;
    gHT_max = 80.0;
    fi = 0.85;
elseif celltype == 3
    Vrest = -64.1;
    Cm = 12.0;
    Vth = -51.2;
    gNa_max = 1000.0;
```

```
VNa = 55.0;
gh_max = 20.0;
Vh = -43.0;
glk_max = 2.0;
Vlk = -65.0;
tauE = 0.07;
gE_theta = 15.0;
%   gE_theta = 2.8;
VE = 0.0;
Vk = -70.0;
gA_max = 0.0;
gLt_max = 20.0;
zeta = 0.5;
gHT_max = 150.0;
fi = 0.85;
elseif celltype == 4
    Vrest = -63.8;
    Cm = 12.0;
    Vth = -58.0;
    gNa_max = 1000.0;
    VNa = 55.0;
    gh_max = 3.5;
    Vh = -43.0;
    glk_max = 2.0;
    Vlk = -65.0;
    tauE = 0.07;
    gE_theta = 17.0;
%   gE_theta = 3.2;
    VE = 0.0;
    Vk = -70.0;
    gA_max = 0.0;
    gLT_max = 35.0;
    zeta = 0.5;
    gHT_max = 150.0;
    fi = 0.85;
elseif celltype == 5
    Vrest = -63.6;
    Cm = 12.0;
    Vth = -62.2;
    gNa_max = 1000.0;
    VNa = 55.0;
    gh_max = 20.0;
    Vh = -43.0;
    glk_max = 2.0;
    Vlk = -65.0;
    tauE = 0.07;
    gE_theta = 34.0;
%   gE_theta = 8.6;
```

```

    VE = 0.0;
    Vk = -70.0;
    gA_max = 0.0;
    gLT_max = 200.0;
    zeta = 0.5;
    gHT_max = 150.0;
    fi = 0.85;
else
    error('Unrecognized Cell Type: Celltype(%d), dB(%d), Hz(%d).', ...
          celltype, stimdb, stimfreq);
end

% External applied current
Iext = 0.0; % Applied external stimulus current in pA

% V = zeros(1,round(simtime/dt));
i = 1; % current V vector index for while loop

% Upsample AN spike train
spikeresamp = [Spike_times; zeros((spikeat/dt)-1,length(Spike_times))];

% Convolve with alpha wave to get AN input variable conductance vector

t = 0:dt:2;
alphawave = (t/tauE).*exp(1-(t./tauE));
% gE = gEtheta*filter(alphawave,1,(spikeat/1000)*spikeresamp(:)');
gE = gEtheta*filter(alphawave,1,spikeresamp(:)');

% Clear loaded data to save memory
clear Spike_times

% Instantiate transmembrane potential vector
V = zeros(1,round(simtime/dt));

% Initial conditions for V
V(i) = Vrest;

% Get initial values of gating particles and their time constants
[a b c w z n p m h r] = gateparts(V(i),zeta);

while(i<length(V))

    % calculate derivatives of parameters and value at next time step
    [dV da db dc dw dz dn dp dm dh dr] = VCN_RK4solv_main_v2(V(i),...
        a,b,c,w,z,n,p,m,h,r,Iext,suborsup*gE(i),dt);

    % Assign new values to current values
    a = a + dt*da;

```

```

b = b + Δt*db;
c = c + Δt*dc;
w = w + Δt*dw;
z = z + Δt*dz;
n = n + Δt*dn;
p = p + Δt*dp;
m = m + Δt*dm;
h = h + Δt*dh;
r = r + Δt*dr;
V(i+1) = V(i) + Δt*dV;

% increment index
i = i+1;
end

```

A.1.2 VCN_RK4solv_main_v2.m

```

function [dV da db dc dw dz dn dp dm dh dr] = ...
    VCN_RK4solv_main_v2(V,a,b,c,w,z,n,p,m,h,r,IExt_cur,gE,Δt)
% This is the main function of the VCN model RK4 solver. It takes as input
% the current values of all of the model parameters, the current applied
% extracellular current and the simulation time step. The function then
% returns the calculated derivatives for all of the model parameters using
% the 4-th order Runge-Kutta method of numerical differentiation.

% Calculate all K-values for all parameters
[K1V K1a K1b K1c K1w K1z K1n K1p K1m K1h K1r] = VCN_RK4solv_v2(V,...
    a,b,c,w,z,n,p,m,h,r,IExt_cur,gE);

[K2V K2a K2b K2c K2w K2z K2n K2p K2m K2h K2r] = VCN_RK4solv_v2( ...
    V+(Δt/2*K1V),a+(Δt/2*K1a),b+(Δt/2*K1b),c+(Δt/2*K1c),...
    w+(Δt/2*K1w),z+(Δt/2*K1z),n+(Δt/2*K1n),p+(Δt/2*K1p),...
    m+(Δt/2*K1m),h+(Δt/2*K1h),r+(Δt/2*K1r),IExt_cur,gE);

[K3V K3a K3b K3c K3w K3z K3n K3p K3m K3h K3r] = VCN_RK4solv_v2( ...
    V+(Δt/2*K2V),a+(Δt/2*K2a),b+(Δt/2*K2b),c+(Δt/2*K2c),...
    w+(Δt/2*K2w),z+(Δt/2*K2z),n+(Δt/2*K2n),p+(Δt/2*K2p),...
    m+(Δt/2*K2m),h+(Δt/2*K2h),r+(Δt/2*K2r),IExt_cur,gE);

[K4V K4a K4b K4c K4w K4z K4n K4p K4m K4h K4r] = VCN_RK4solv_v2( ...
    V+(Δt*K3V),a+(Δt*K3a),b+(Δt*K3b),c+(Δt*K3c),...
    w+(Δt*K3w),z+(Δt*K3z),n+(Δt*K3n),p+(Δt*K3p),...
    m+(Δt*K3m),h+(Δt*K3h),r+(Δt*K3r),IExt_cur,gE);

% Calculate the derivative of each model parameter
dV = RK4_deriv_calc(K1V,K2V,K3V,K4V);
da = RK4_deriv_calc(K1a,K2a,K3a,K4a);

```

```

db = RK4_deriv_calc(K1b,K2b,K3b,K4b);
dc = RK4_deriv_calc(K1c,K2c,K3c,K4c);
dw = RK4_deriv_calc(K1w,K2w,K3w,K4w);
dz = RK4_deriv_calc(K1z,K2z,K3z,K4z);
dn = RK4_deriv_calc(K1n,K2n,K3n,K4n);
dp = RK4_deriv_calc(K1p,K2p,K3p,K4p);
dm = RK4_deriv_calc(K1m,K2m,K3m,K4m);
dh = RK4_deriv_calc(K1h,K2h,K3h,K4h);
dr = RK4_deriv_calc(K1r,K2r,K3r,K4r);

```

A.1.3 VCN_RK4solv_v2.m

```

function [KV Ka Kb Kc Kw Kz Kn Kp Km Kh Kr] = ...
    VCN_RK4solv_v2(V,a,b,c,w,z,n,p,m,h,r,IExt_cur,gE)
% This function calculates the current K values for each of the parameters
% in the VCN model using the 4-th order Runge-Kutta method. The input
% parameters are the current values of all of the model parameters as well
% as the current value of the applied extra-cellular current.

% Find current steady state value of gating particle dynamics and time
% constants of change at current transmembrane potential.
[ass bss css wss zss nss pss mss hss rss] = gateparts(V,0.5);
[ta tb tc tw tz tn tp tm th tr] = gatetaus_v2(V);

% Calculate K values
KV = voltderiv_v2(V,IExt_cur,a,b,c,w,z,n,p,m,h,r,gE);
Ka = gatederiv(a,ass,ta);
Kb = gatederiv(b,bss,tb);
Kc = gatederiv(c,css,tc);
Kw = gatederiv(w,wss,tw);
Kz = gatederiv(z,zss,tz);
Kn = gatederiv(n,nss,tn);
Kp = gatederiv(p,pss,tp);
Km = gatederiv(m,mss,tm);
Kh = gatederiv(h,hss,th);
Kr = gatederiv(r,rss,tr);

```

A.1.4 RK4_deriv_calc.m

```

function deriv = RK4_deriv_calc(K1,K2,K3,K4)
% This function calculates the weighted average of the K values produced by
% the 4th order Runge-Kutta method to return the derivative of the
% parameter.

deriv = ((K1+(2*K2)+(2*K3)+K4)/6);

```

A.1.5 VCN_RK4solv_main_v2.m

```

function [dV da db dc dw dz dn dp dm dh dr] = ...
    VCN_RK4solv_main_v2(V,a,b,c,w,z,n,p,m,h,r,IExt_cur,gE,delta)
% This is the main function of the VCN model RK4 solver. It takes as input
% the current values of all of the model parameters, the current applied
% extracellular current and the simulation time step. The function then
% returns the calculated derivatives for all of the model parameters using
% the 4-th order Runge-Kutta method of numerical differentiation.

% Calculate all K-values for all parameters
[K1V K1a K1b K1c K1w K1z K1n K1p K1m K1h K1r] = VCN_RK4solv_v2(V,...
    a,b,c,w,z,n,p,m,h,r,IExt_cur,gE);

[K2V K2a K2b K2c K2w K2z K2n K2p K2m K2h K2r] = VCN_RK4solv_v2(...
    V+(delta/2*K1V),a+(delta/2*K1a),b+(delta/2*K1b),c+(delta/2*K1c),...
    w+(delta/2*K1w),z+(delta/2*K1z),n+(delta/2*K1n),p+(delta/2*K1p),...
    m+(delta/2*K1m),h+(delta/2*K1h),r+(delta/2*K1r),IExt_cur,gE);

[K3V K3a K3b K3c K3w K3z K3n K3p K3m K3h K3r] = VCN_RK4solv_v2(...
    V+(delta/2*K2V),a+(delta/2*K2a),b+(delta/2*K2b),c+(delta/2*K2c),...
    w+(delta/2*K2w),z+(delta/2*K2z),n+(delta/2*K2n),p+(delta/2*K2p),...
    m+(delta/2*K2m),h+(delta/2*K2h),r+(delta/2*K2r),IExt_cur,gE);

[K4V K4a K4b K4c K4w K4z K4n K4p K4m K4h K4r] = VCN_RK4solv_v2(...
    V+(delta*K3V),a+(delta*K3a),b+(delta*K3b),c+(delta*K3c),...
    w+(delta*K3w),z+(delta*K3z),n+(delta*K3n),p+(delta*K3p),...
    m+(delta*K3m),h+(delta*K3h),r+(delta*K3r),IExt_cur,gE);

% Calculate the derivative of each model parameter
dV = RK4_deriv_calc(K1V,K2V,K3V,K4V);
da = RK4_deriv_calc(K1a,K2a,K3a,K4a);
db = RK4_deriv_calc(K1b,K2b,K3b,K4b);
dc = RK4_deriv_calc(K1c,K2c,K3c,K4c);
dw = RK4_deriv_calc(K1w,K2w,K3w,K4w);
dz = RK4_deriv_calc(K1z,K2z,K3z,K4z);
dn = RK4_deriv_calc(K1n,K2n,K3n,K4n);
dp = RK4_deriv_calc(K1p,K2p,K3p,K4p);
dm = RK4_deriv_calc(K1m,K2m,K3m,K4m);
dh = RK4_deriv_calc(K1h,K2h,K3h,K4h);
dr = RK4_deriv_calc(K1r,K2r,K3r,K4r);

```

A.1.6 gateparts.m

```

function [a b c w z n p m h r] = gateparts(V,zeta)
% This function calculatates the steady state values of all of the VCN

```

```
% model gating particles at a particular transmembrane potential in mV

a = power(1+exp(-(V+31)/6),-1/4);
b = power(1+exp((V+66)/7),-1/2);
c = b;
w = power(1+exp(-(V+48)/6),-1/4);
z = (1-zeta)*power(1+exp((V+71)/10),-1)+zeta;
n = power(1+exp(-(V+15)/5),-1/2);
p = power(1+exp(-(V+23)/6),-1);
m = power(1+exp(-(V+38)/7),-1);
h = power(1+exp((V+65)/6),-1);
r = power(1+exp((V+76)/7),-1);
```

A.1.7 gatetaus_v2.m

```
function [ta tb tc tw tz tn tp tm th tr] = gatetaus_v2(V)
% This function calculatates the time constants for each of the gating
% particles in the VCN model at a particular transmembrane potential (V)
% in mV.

ta = 0.17*(100/(7*exp((V+60)/14)+29*exp(-(V+60)/24)) + 0.1);
tb = 0.17*(1000/(14*exp((V+60)/27)+29*exp(-(V+60)/24)) + 1.0);
tc = 0.17*(90/(1+exp(-(V+66)/17)) + 10.0);
tw = 0.17*(100/(6*exp((V+60)/6)+16*exp(-(V+60)/45)) + 1.5);
tz = 0.17*(1000/(exp((V+60)/20)+exp(-(V+60)/8)) + 50.0);
tn = 0.17*(100/(11*exp((V+60)/24)+21*exp(-(V+60)/23)) + 0.7);
tp = 0.17*(100/(4*exp((V+60)/32)+5*exp(-(V+60)/22)) + 5.0);
tm = 0.17*(10/(5*exp((V+60)/18)+36*exp(-(V+60)/25)) + 0.04);
th = 0.17*(100/(7*exp((V+60)/11)+10*exp(-(V+60)/25)) + 0.6);
tr = 0.17*(1e5/(237*exp((V+60)/12)+17*exp(-(V+60)/14)) + 25.0);
```

A.1.8 voltderiv_v2.m

```
function dVdt = voltderiv_v2(V_cur,IExt_cur,a,b,c,w,z,n,p,m,h,r,gE)
% This function calculates the derivative of the VCN cell transmembrane
% potential. V_cur represents the current transmembrane potential.
% IExt_cur is the external stimulus currently being applied. The rest of
% the parameters represent the gating particle constants as described in
% Rothman and Mannis 2003.

% Model Parameters
global Cm; % Membrane capacitance in pF
global Vth; % Threshold potential in mV

% Sodium Current Parameters
```

```

global gNa_max; % Sodium current peak conductance in nS
global VNa; % Sodium current reversal potential in mV

% Hyperpolarization-activated cation current parameters
global gh_max; % Ih current peak conductance in nS
global Vh; % h current reversal potential in mV

% Model leakage current
global glk_max; % Leakage current max conductance in nS
global Vlk; % Leakage current reversal potential in mV

% Model excitatory post-synaptic current
global tauE; % Excitatory synaptic current time constant in ms
global gE_theta; % Synaptic efficacy of synaptic inputs in nS
global VE; % IE reversal potential in mV

% IA: Fast transient K current
global Vk; % Fast transient K current reversal potential in mV
global gA_max; % Fast transient K current maximum conductance in nS

% ILT: Low-threshold K current
global gLT_max; % Low-threshold K current maximum conductance in nS
global zeta; % gating particle dynamics constant

% High-threshold K current
global gHT_max; % High-threshold K current maximum conductance in nS
global fi; % constant for High-threshold K current activation particles

IA = 3.03*gA_max*(a^4)*b*c*(V_cur-Vk);
ILT = 3.03*gLT_max*(w^4)*z*(V_cur-Vk);
IHT = 3.03*gHT_max*(fi*(n^2)+(1-fi)*p)*(V_cur-Vk);
INa = 3.03*gNa_max*(m^3)*h*(V_cur-VNa);
Ih = 3.03*gh_max*r*(V_cur-Vh);
Ilk = 3.03*glk_max*(V_cur-Vlk);
IE = gE*(V_cur-VE);

dVdt = -((IA+ILT+IHT+INa+Ih+Ilk+IE-IEExt_cur)/Cm);

```

A.1.9 gatederiv.m

```

function dxdt = gatederiv(x,xss,taux)
% This function calculates the rate of change of a gating particle with
% respect to change. The input x is the current value of the gating
% particle. xss represents the steady state value of the gating particle
% at the current transmembrane potential (calculated using the GATEPARTS
% function). taux is teh time constant of the gating particle at the
% current transmembrane potential (calculated using the GATETAUS function).

```

```
dxdt = (xss - x)/taux;
```

A.2 CV Calculation Code

A.2.1 CVplot.m

```
nrep = 100; % number of stimulus repetitions
CVbin = 1; % size of CV calculation bins (ms)
% spikeat = 0.01; % bin size of simulated AN spike trains (ms)
spikeat = 0.001; % bin size of simulated AN spike trains (ms)
stimtime = 50; % stimulus length (ms)
% stimtime = 17*spikeat;

% Cell input configuration
CT = 5; % VCN model cell type
numANfibs = 1; % number of input AN fibers
BW = 0; % Bandwidth of AN inputs in octaves

stimdb = 60; %stimulus intensity in dB SPL
modelCF = 5000; % VCN cell BF in Hz
stimfreq = modelCF; % stimulus frequency in Hz
healthimp = 1; % if 1, unimpaired AN inputs, if 0, impaired AN inputs

if healthimp ≠ 1
    subloc = '\VCNimpaired';
else
    subloc = '\VCNhealthy';
end

savespot = [ subloc '\VCNoutsCF_' num2str(modelCF) 'Hz_' ...
    num2str(numANfibs) 'ANfibs_BW' num2str(BW) 'oct'];
filenam = [pwd savespot '\VCNoutdat_CT' num2str(CT) '_' ...
    num2str(stimdb) 'dB' num2str(stimfreq) 'Hz'];

load(filenam);

[row col val] = find(psth);

numANbinsperCVbin = CVbin/spikeat; % num of spike train bins per CV bin
numCVbinspersim = floor((stimtime-10)/CVbin); % num of CV bins per spiketrain

sigmavec = zeros(1,numCVbinspersim); % init bin standard deviation vector
meanvec = zeros(1,numCVbinspersim); % init bin mean vector

for i = 1:numCVbinspersim
```

```

ISIsinbin = [];
for curcol = (i-1)*numANbinsperCVbin+1:numANbinsperCVbin*i
    startcolindex = find(col==curcol,1,'first');
    endcolindex = find(col==curcol,1,'last');

    for j=startcolindex:endcolindex
        nextspike = find(psth(row(j),curcol+1:end),1,'first');
        if (nextspike+curcol) ≤ (stimtime/spikeΔt)
%           ISIsinbin = [ISIsinbin (nextspike-row(j))];
            ISIsinbin = [ISIsinbin nextspike];
        end
    end
end

sigmavec(i) = std(ISIsinbin)*spikeΔt;
meanvec(i) = mean(ISIsinbin)*spikeΔt;
end

CVvec = sigmavec./meanvec;

figure;
hold on
plot(CVbin*(1:numCVbinspersim),sigmavec,'b--',CVbin*...
(1:numCVbinspersim),meanvec,'r-');
title(['BF tone @ ' num2str(stimdb) ' dB SPL: ' ...
num2str(numANfibs) ' AN fibers with a BW of ' num2str(BW)...
' octaves'], 'FontSize',16);
xlabel('Simulation Time (ms)', 'FontSize',16);
ylabel('Time (ms)', 'FontSize',16);
set(gca, 'FontSize',14);
legend('ISI standard deviation','ISI mean','Location','SouthEast');
text(numCVbinspersim-30,max(meanvec)+0.1,['CV = ' ...
num2str(nanmean(CVvec))], 'FontSize',16);
hold off

```

A.3 Code for generating AN inputs to the Zheng and Voigt (2006) DCN model

A.3.1 fANimpairgenv2.m

```

function fANimpairgenv2(stimdb)
% This function takes as input the stimulus frequency in Hz and the
% stimulus intensity in dB and generates a data file containing the
% spike trains of the 800 AN fibres needed for input to the Zheng and
% Voigt (2006) model of the DCN.

```

```

%
% Load in CFs and spont rates of all input AN fibres
load ANfibredat

% Stimulus parameters
stimdelay = 10e-3; % onset delay in seconds
stimlen = 0.2; % lenth of stimulus in seconds
risefall = 5e-3; % rise/fall time in seconds
T = 1; % trial length in seconds
Fs = 50e3; % sampling rate of output spike train in Hz
Fzbmodel = 100e3; % sampling rate for ZBcatmodel

freqslices = 31; % number of frequency slices in simulation

t = 0:1/Fzbmodel:T-1/Fzbmodel; % time vector

% Create/Open file to save data
mbf = single(5);
freqstep = single(0.1);

% calculates input frequencies
frq = zeros(1,freqslices,'single');
for i=1:freqslices
    if (mod(int32(i),int32(2)) == 0)
        frq(i) = mbf*2^(single((int32(i-1)/int32(2)))*freqstep);
    else
        frq(i) = mbf*2^(-single((int32(i-1)/int32(2)))*freqstep);
    end
end

% Generate fibre parameters for hearing loss
audiogfs = 1000*[1:6 6.5:0.5:10 10.5 21]; % audiogram frequencies
dBloss = [zeros(1,6) 28 40 46 62.5 75 76 76 80 80 80]; % audiogram dBloss

dBlossCfs = interp1(audiogfs,dBloss,ANCFs); % AN threshold shifts

[Cohc Cihc] = fitaudiogram(ANCFs,dBlossCfs); % AN fibre parameters

% create AN fibre data for each stimulus frequency at input SPL
for k=1:freqslices
    F0 = 1000*frq(k); % input stimulus frequency

    % creates and opens data file for saving data
    %filename = 'cfile2.an800'
    x = sprintf('f%04d%03d.an%d',fix(F0),fix(single(stimdb)),fix(800))
    filename = [pwd '/data_imp/' x];
    fdat = fopen(filename,'w');

```

```

% Generate tone stimulus vector
pin = zeros(1,T*Fzbmodel);
pin(round(stimdelay*Fzbmodel)+1:round(((stimdelay+stimlen)*Fzbmodel))...
    = sqrt(2)*20e-6*(10^(stimdb/20))*sin(2*pi*F0*(t(...
    round(stimdelay*Fzbmodel)+1:round(((stimdelay+stimlen)*Fzbmodel))...
    -stimdelay));

% Rise/Fall envelopes
priseenv = 0.5*(1 - cos(2*pi*(t(round(stimdelay*Fzbmodel)...
    +1:round(((stimdelay+risefall)*Fzbmodel))-stimdelay)/2/...
    (risefall-1/Fzbmodel)));

pfallenv = 0.5*(1 - cos(2*pi*(stimdelay+stimlen-t(round(...
    stimdelay-risefall+stimlen)*Fzbmodel)+1:round(...
    stimdelay+stimlen)*Fzbmodel)))/2/(risefall));

% Multiply Input signal by cosine rise/fall envelopes
pin(round(stimdelay*Fzbmodel)+1:round(((stimdelay+risefall)...
    *Fzbmodel))) = priseenv.*pin(round(stimdelay*Fzbmodel)+1:...
    round(((stimdelay+risefall)*Fzbmodel)));

pin(round((stimdelay-risefall+stimlen)*Fzbmodel)+1:round(...
    stimdelay+stimlen)*Fzbmodel))) = pfallenv.*pin(round(...
    stimdelay-risefall+stimlen)*Fzbmodel)+1:round(...
    (stimdelay+stimlen)*Fzbmodel));

% Generate AN spike time vectors
for j = 1:length(ANCFs)

    % model fiber parameters
    cohcn = Cohc(j) % normal ohc function
    cihcn = Cihc(j) % normal ihc function

    % PSTH parameters
    nrep = 1; % number of stimulus repetitions (e.g., 50);
    psthbinwidth = 1/Fs; % binwidth in seconds;

    [timeout,meout,c1filterout,c2filterout,c1vihc,c2vihc,vihc,synout...
    ,psth500k] = zbcatsmodel(pin,ANCFs(j),nrep,1/Fzbmodel,T,cohcn,...
    cihcn,SFR2(j));

    % number of psth500k bins per psth bin
    psthbins = round(psthbinwidth*Fzbmodel);
    psthtime = timeout(1:psthbins:end); % time vector for psth
    % pr of spike in each bin
    pr = sum(reshape(psth500k,psthbins,length(psth500k)/psthbins))...

```

```

/nrep;

sptimes = find(pr > 0); % vector of AP times
numspikes = sum(pr); % number of Action Potentials
isis = sptimes-[0 sptimes(1:length(sptimes)-1)]; % vector of ISIs

% Write AN spike train to data file

fwrite(fdat,numspikes,'int32',0,'ieee-be');
for i=1:numspikes
    if isis(i) < 65536
        fwrite(fdat,isis(i),'uint16',0,'ieee-be');
    else
        fwrite(fdat,hex2dec('ffff'),'uint16',0,'ieee-be');
        fwrite(fdat,isis(i),'int32',0,'ieee-be');
    end
end
end

end
% Close AN spike train file
status = fclose(fdat);
end

```

A.4 DCN model ideal parameters

The ideal set of Zheng and Voigt (2006) model connection parameters capable of producing physiological DCN principal responses to AN inputs simulated by the Zilany and Bruce (2007) model can be found in the following tables. Table A.1, Table A.2 and Table A.3 shows the set of connection parameters that generate type III, type IV and type IV-T cell responses, respectively. Note that parameters not shown are as they appear in Zheng and Voigt (2006).

Table A.1: Type III response DCN model parameters

Connection A→B	$BW_{A→B}$ (octaves)	$N_{A→B}$	$\sigma_{A→B}$
AN→W	2.0	140	0.08
AN→I2	0.4	48	0.800
AN→P	0.3	48	0.2
W→I2	0.1	15	1.40
W→P	0.1	15	1.0
I2→P	0.6	21	0.04

Table A.2: Type IV response DCN model parameters

Connection A→B	$BW_{A→B}$ (octaves)	$N_{A→B}$	$\sigma_{A→B}$
AN→W	2.0	140	0.08
AN→I2	0.4	48	0.800
AN→P	0.4	48	0.434
W→I2	0.1	15	1.40
W→P	0.1	15	1.0
I2→P	0.6	21	1.516

Table A.3: Type IV-T response DCN model parameters

Connection A→B	$BW_{A→B}$ (octaves)	$N_{A→B}$	$\sigma_{A→B}$
AN→W	2.0	140	0.08
AN→I2	0.4	48	0.800
AN→P	0.4	48	0.64
W→I2	0.1	15	1.40
W→P	0.1	15	1.2
I2→P	0.6	21	2.206

Bibliography

- Banks, M. I., Pearce, R. A., and Smith, P. H. (1993). Hyperpolarization-activated cation current (I_h) in neurons of the medial nucleus of the trapezoid body: Voltage-clamp analysis and enhancement by norepinephrine and camp suggest a modulatory mechanism in the auditory brain stem. *J. Neurophysiol.*, **70**, 1420–1432.
- Belluzzi, O., Sacchi, O., and Wanke, E. (1985). A fast transient outward current in the rat sympathetic neurone studied under voltage-clamp conditions. *J. Physiol.*, **358**, 91–108.
- Bruce, I. C., Sachs, M. B., and Young, E. D. (2003). An auditory-periphery model of the effects of acoustic trauma on auditory nerve responses. *J. Acoust. Soc. Am.*, **113**, 369–388.
- Cai, S., Di, W.-L., and Young, E. D. (2008). Encoding intensity in ventral cochlear nucleus following acoustic trauma: Implications for loudness recruitment. *JARO*, **9**, 506–520.
- Cant, N. B. and Benson, C. G. (2003). Parallel auditory pathways: projection patterns of the different neuronal populations in the dorsal and ventral cochlear nuclei. *Brain Research Bulletin*, **60**, 457–474.
- Carney, L. H. (1993). A model for the responses of low-frequency auditory-nerve fibers in cat. *The Journal of the Acoustical Society of America*, **93**, 401–417.
- Chapra, S. C. and Canale, R. P. (2002). *Numerical Methods for Engineers*. McGraw-Hill, fourth edition.
- Costa, P. F. (1996). The kinetic parameters of sodium currents in maturing acutely isolated hippocampal ca1 neurones. *Developmental Brain Research*, **91**, 29–40.
- Davis, K. A. and Voigt, H. F. (1996). Computer simulation of shared input among projection neurons in the dorsal cochlear nucleus. *Biol. Cybern.*, **74**, 413–425.
- Davis, K. A., Gdowski, G. T., and Voigt, H. F. (1995). A statistically based method to generate response maps objectively. *J. Neurosci.*, **57**, 107–118.
- Doucet, J. R. and Ryugo, D. K. (1997). Projections from the ventral cochlear nucleus to the dorsal cochlear nucleus in rats. *The Journal of Comparative Neurology*, **385**, 245–264.
- EnchantedLearning.com (2009). Brain cells. <http://www.enchantedlearning.com/subjects/anatomy/brain/Neuron.shtml>.

- Evans, E. (1972). The frequency response and other properties of single fibers in the guinea-pig cochlear nerve. *J. Physiol.*, **226**, 236–287.
- Ferragamo, M. J., Golding, N. L., and Oertel, D. (1998). Synaptic inputs to stellate cells in the ventral cochlear nucleus. *J. Neurophysiol.*, **98**, 51–63.
- Fu, X. W., Brezden, B. L., and Wu, S. H. (1997). Hyperpolarization-activated inward current in neurons of the rat's dorsal nucleus of the lateral lemniscus in vitro. *J. Neurophysiol.*, **78**, 2235–2245.
- Greenwood, D. S. (1990). A cochlear frequency-position function for several species—29 years later. *J. Acoust. Soc. Am.*, **87**, 2592–2605.
- Guyton, A. C. and Hall, J. E. (2000). *Textbook of Medical Physiology*. W. B. Saunders Company, tenth edition.
- Huguenard, J. R. and McCormick, D. A. (1992). Simulation of the currents involved in rhythmic oscillations in thalamic relay neurons. *J. Neurophysiol.*, **68**, 1373–1383.
- Johnson, D. H. (1980). The relationship between spike rate and synchrony in responses of auditory-nerve fibers to single tones. *J. Acoust. Soc. Am.*, **68**, 1115–1122.
- Johnson, D. H., Tsuchitani, C., Linebarger, D., and Johnson, M. (1986). Application of a point process model to responses of cat lateral superior olive units to ipsilateral tones. *Hear. Res.*, **21**, 135–159.
- Kiang, N. Y.-S. (1990). Curious oddments of auditory-nerve studies. *Hearing Research*, **49**, 1–16.
- Koch, C. (1999). *Biophysics of Computation: information processing in single neurons*. Oxford University Press, Inc.
- Liberman, M. C. (1982). The cochlear frequency map for the cat: Labeling auditory-nerve fibers of known characteristic frequency. *J. Acoust. Soc. Am.*, **72**, 1441–1449.
- Liberman, M. C. (1991). Central projections of auditory-nerve fibers of differing spontaneous rate. I. anteroventral cochlear nucleus. *J. Comparative Neurology*, **313**, 240–258.
- Liberman, M. C. (1993). Central projections of auditory-nerve fibers of differing spontaneous rate, II: Posteroventral and dorsal cochlear nuclei. *J. Comparative Neurology*, **317**, 17–36.

- Lomakin, O. and Davis, K. A. (2008). On the role of the wideband inhibitor in the dorsal cochlear nucleus: a computational modeling study. *JARO*, **9**, 506–520.
- Ma, W.-L. D. and Young, E. D. (2006). Dorsal cochlear nucleus response properties following acoustic trauma: Response maps and spontaneous activity. *Hearing Research*, **216-217**, 176–188.
- MacGregor, R. J. (1987). *Neural and brain modeling*. Academic Press, San Diego.
- Oertel, D. and Young, E. D. (2004). What’s a cerebellar circuit doing in the auditory system? *Trends in Neurosciences*, **27**, 104–110.
- Oertel, D., Bal, R., Gardner, S. M., Smith, P. H., and Joris, P. X. (2000). Detection of synchrony in the activity of auditory nerve fibers by octopus cells of the mammalian cochlear nucleus. *Proceedings of the National Academy of Sciences*, **97**, 11773–11779.
- Oertel, D., Fay, R. R., and Popper, A. N. (2002). *Integrative Functions in the Mammalian Auditory Pathway*. Springer-Verlag, New York, Inc.
- Palmer, A. and Russell, I. (1986). Phase-locking in the cochlear nerve of the guinea-pig and its relation to the receptor potential of inner hair cells. *Hear. Res.*, **24**, 1–15.
- Palmer, A. R., Wallace, M. N., Arnott, R. H., and Shackleton, T. M. (2003). Morphology of physiologically characterised ventral cochlear nucleus stellate cells. *Exp. Brain. Res.*, **153**, 418–426.
- Pickles, J. O. (2008). *An Introduction to the Physiology of Hearing*. Emerald Group Publishing Ltd., third edition.
- Plonsey, R. and Barr, R. C. (2000). *Bioelectricity: a quantitative approach*. Kluwer Academic/Plenum, second edition.
- Reiss, L. A. J. and Young, E. D. (2005). Spectral edge sensitivity in neural circuits of the dorsal cochlear nucleus. *The Journal of Neuroscience*, **25**, 3680–3691.
- Rhode, W. S. (2008). Response patterns to sound associated with labeled globular/bushy cells in cat. *Neuroscience*, **154**, 87–98.
- Rhode, W. S. and Smith, P. H. (1986). Encoding timing and intensity in the ventral cochlear nucleus of the cat. *J. Neurophysiol.*, **56**, 261–286.

- Rothman, J. S. and Manis, P. B. (2006a). Differential expressions of three distinct potassium currents in the ventral cochlear nucleus. *J. Neurophysiol.*, **89**, 3070–3082.
- Rothman, J. S. and Manis, P. B. (2006b). Kinetic analyses of three distinct potassium conductances in ventral cochlear nucleus neurons. *J. Neurophysiol.*, **89**, 3083–3096.
- Rothman, J. S. and Manis, P. B. (2006c). The roles potassium currents play in regulating the electrical activity of ventral cochlear nucleus neurons. *J. Neurophysiol.*, **89**, 3097–3113.
- Rothman, J. S., Young, E. D., and Manis, P. B. (1993). Convergence of auditory nerve fibers onto bushy cells in the ventral cochlear nucleus: Implications of a computational model. *J. Neurophysiol.*, **70**, 2562–2583.
- Ruggero, M. A., Rich, N. C., Recio, A., Narayan, S. S., and Robles, L. (1997). Basilar-membrane responses to tones at the base of the chinchilla cochlea. *J. Acoust. Soc. Am.*, **101**, 2151–2163.
- Ryugo, D. K. and May, S. K. (1993). The projections of intracellularly labeled auditory nerve fibers to the dorsal cochlear nucleus of cats. *The Journal of Comparative Neurology*, **329**, 20–35.
- Ryugo, D. K. and Parks, T. N. (2003). Primary innervation of the avian and mammalian cochlear nucleus. *Brain Research Bulletin*, **60**, 435–456.
- Syka, J. (2002). Plastic changes in the central auditory system after hearing loss, restoration of function, and during hearing. *Physiol. Review.*, **82**, 601–636.
- Tan, Q. and Carney, L. H. (2003). A phenomenological model for the responses of auditory-nerve fiber. II. nonlinear tuning with a frequency glide. *J. Acoust. Soc. Am.*, **114**, 2007–2020.
- Tortora, G. J. and Grabowski, S. R. (2003). *Principles of Anatomy and Physiology*. John Wiley & Sons Inc., tenth edition.
- Travagli, R. A. and Gillis, R. A. (1994). Hyperpolarization-activated currents, I_H and I_{KIR} , in rat dorsal motor nucleus of the vagus neurons in vitro. *J. Neurophysiol.*, **71**, 1308–1317.
- universe-review.ca (2009). Nervous system. <http://universe-review.ca/R10-16-ANS.htm>.

- van Netten, S. M., Meulenberg, C. J. W., Lennan, G. W. T., and Kros, C. J. (2008). Pairwise coupling of hair cell transducer channels links auditory sensitivity and dynamic range. *Eur. J. Physiol.*, **10**, 1–9.
- Young, E. D. and Oertel, D. (2004). The cochlear nucleus. In G. M. Shepherd, editor, *The Synaptic Organization of the Brain*. Oxford University Press, fifth edition.
- Young, E. D., Robert, J.-M., and Shofner, W. P. (1988). Regularity and latency of units in ventral cochlear nucleus: implications for unit classification and generation of response properties. *J. Neurophysiol.*, **60**, 1–29.
- Zhang, X., Heinz, M. G., Bruce, I. C., and Carney, L. H. (2001). A phenomenological model for the responses of auditory-nerve fiber. II. nonlinear tuning with compression and suppression. *J. Acoust. Soc. Am.*, **109**, 648–670.
- Zheng, X. and Voigt, H. F. (2006). Computational model of response maps in the dorsal cochlear nucleus. *Biol. Cybern.*, **95**, 233–242.
- Zheng, X., Giang, A., Vetsis, S., Bruce, I. C., and Voigt, H. F. (2008). A computational modeling study of the effects of acoustic trauma on the dorsal cochlear nucleus. In *Proceedings of 4th European Conference of the International Federation for Medical and Biological Engineering (ECIFMBE 2008)*, volume 22, pages 2695–2698. Antwerp, Belgium.
- Zilany, M. S. A. and Bruce, I. C. (2006). Modeling auditory-nerve responses for high sound pressure levels in the normal and impaired auditory periphery. *J. Acoust. Soc. Am.*, **120**, 1446–1466.
- Zilany, M. S. A. and Bruce, I. C. (2007). Representation of the vowel /ε/ in normal and impaired auditory nerve fibers: Model predictions of responses in cats. *J. Acoust. Soc. Am.*, **122**, 402–417.